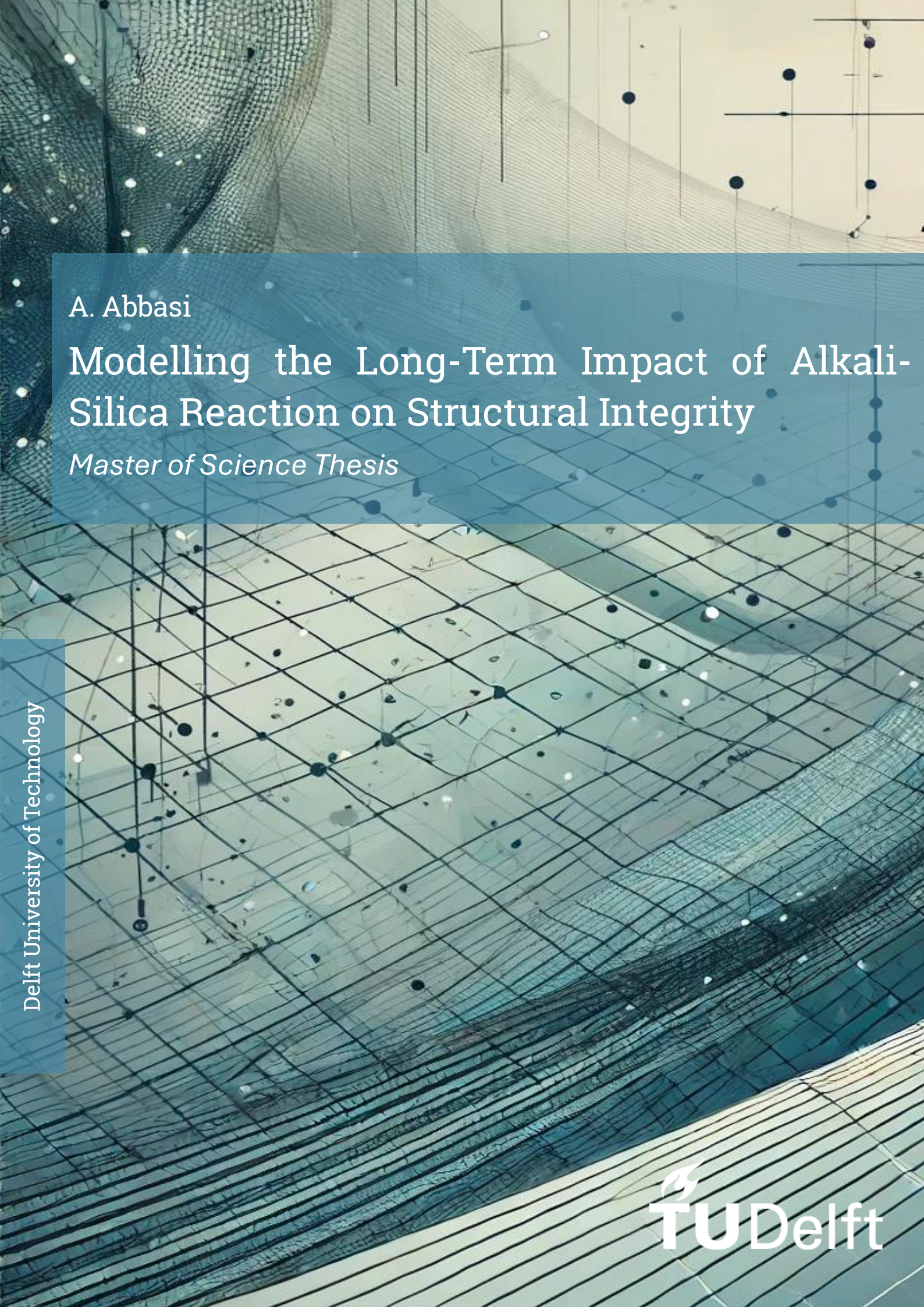

A. Abbasi

Modelling the Long-Term Impact of Alkali-Silica Reaction on Structural Integrity

Master of Science Thesis

Delft University of Technology

TU Delft

[Cover image generated by DALL·E 3, November 5, 2024, Open AI]

Modelling the Long-Term Impact of Alkali-Silica Reaction on Structural Integrity

Main author: A. (Anas) Abbasi

MSc Civil Engineering (Track: Structural Engineering)
Faculty of Civil Engineering and Geosciences
Delft University of Technology

Assessment committee:

Dr. Oğuzhan Çopuroğlu (Chair)	TU Delft
ir. Patrick Holthuizen (Daily supervisor)	TU Delft
Dr.ir. Branko Šavija	TU Delft
Prof.dr.ir. Max Hendriks	TU Delft

Date: January 2025

Acknowledgement

This thesis marks the completion of my Master's journey in Civil Engineering at Delft University of Technology. The path to this milestone has been both challenging and fulfilling, shaped by growth, learning, and the support of many people along the way. First and foremost, all praise is due to Allah for His countless blessings and guidance, making this achievement possible and surrounding me with incredible individuals who contributed directly and indirectly to this work.

I am deeply grateful to my assessment committee for their support throughout this process. I extend my heartfelt thanks to Dr. Oğuzhan Çopuroğlu (Chair) for his guidance and encouragement, which has been central to my academic and professional development. From my earliest courses in Building Materials to this thesis, his insights and motivation were invaluable in keeping me on track during challenging moments. Special thanks go to ir. Patrick Holthuizen, my daily supervisor, for his enthusiasm, availability, and dedication, which greatly enriched this research. The discussions we had were extremely valuable, and his generosity in sharing knowledge and resources enhanced the quality of my work. I also wish to thank Dr.ir. Branko Šavija for his critical feedback and thoughtful suggestions, which helped me stay focused and clarify my approach. Additionally, I deeply appreciate the contributions of Prof.dr.ir. Max Hendriks, whose expertise in numerical modelling and insightful input added immense value to this research. Their collective guidance and expertise were instrumental in the successful completion of this thesis.

I am also deeply thankful to my friends and family, who offered unwavering support throughout this journey. I am especially grateful to ir. Anas Kariouh for dedicating his time to proofreading and helping refine this report, as well as to ir. Khalil Akchikchi and ir. Brahim Bougarchouh for their encouragement and support. To my brother Diaa, thank you for your logistical help, and to my sister Yousra, for her academic insight and encouragement.

Finally, I owe my greatest gratitude to my parents, who have sacrificed so much to ensure my success. Their love, support, and belief in me have been a constant source of strength and motivation. Words cannot fully express my gratitude to you. This accomplishment is as much yours as it is mine.

Anas Abbasi

The Hague, January 2025

Abstract

Alkali-Silica Reaction (ASR) poses a significant challenge to the durability and structural integrity of reinforced concrete structures worldwide. This thesis presents a comprehensive modelling framework that integrates numerical simulations and phenomenological models to predict the long-term behaviour of ASR-affected structures. The framework addresses the progressive degradation of material properties and the structural implications of ASR-induced expansion, using expansion characteristics derived from experimental data.

Several numerical methods exist to simulate ASR effects at the structural scale. Among these, the Dual Mesh Method (DMM) stands out as novel pre-damage method to simulate ASR induced damage in reinforced concrete. Building upon this approach, this research develops the Modified Dual Mesh Method (MDMM), introducing key advancements such as an adapted tensile curve (ATC) to enhance its predictive capabilities.

The MDMM was validated numerically against reinforced concrete beam behaviour, demonstrating its effectiveness in simulating ASR-induced stress generation, crack propagation, and material degradation under incremental expansion conditions. A comparative analysis with the Reduced Material Properties Method (RMPM) highlighted the MDMM's effective ability to account for internal expansion forces and anisotropic behaviour influenced by structural configurations. The results confirmed the framework's accuracy in replicating critical structural responses such as crack propagation patterns and load-deflection behaviour.

Phenomenological models by Larive and Esposito were integrated into the framework, linking ASR-induced expansion with time and material property degradation. These models enabled long-term damage simulations and were applied to a hypothetical bridge pier cap. The simulation successfully captured key aspects of ASR-induced damage, including crack alignment with reinforcement, stress redistribution, and reinforcement yielding, providing insights into the service life thresholds of ASR-affected structures.

While the framework demonstrates promising capabilities, it remains in an early development stage. Limitations were observed, particularly in accurately representing the gradual reduction of elastic modulus associated with ASR progression. Further validation with complete case studies and exploration of diverse structural configurations are recommended to enhance its applicability and reliability.

This research offers a valuable tool for structural assessment, maintenance planning of ASR-affected infrastructure, bridging the gap between experimental observations and predictive modelling of long-term structural performance.

Keywords:

Alkali-Silica Reaction (ASR), Numerical Modelling, Dual Mesh Method (DMM), Modified Dual Mesh Method (MDMM), Structural Integrity, Reinforced Concrete, Finite Element Method (FEM), Material Degradation, Time-Dependent Expansion, Concrete Durability, Larive's model, Esposito's model, Infrastructure Maintenance and Anisotropic Expansion

Table of Contents

Abbreviations

2D	Two-Dimensional
3D	Three-Dimensional
ASR	Alkali-Silica Reaction
ATC	Adapted Tensile Curve
DMM	Dual Mesh Method
FEM	Finite Element Method
FEA	Finite Element Analysis
MDMM	Modified Dual Mesh Method
MP	Material Properties
RC	Reinforced Concrete
RMPM	Reduced Material Properties Method
SMM	Single Mesh Method

1. Introduction

1.1 Background

Alkali-Silica Reaction (ASR) is a harmful chemical process that affects the long-term durability and structural integrity of concrete structures worldwide. First identified in structures in the 1940s [1], ASR occurs when reactive silica in aggregates reacts with alkali hydroxides in the concrete pore solution, leading to the formation of an expansive alkali-silica gel. This gel absorbs moisture and expands, inducing internal stresses that cause microcracking, loss of mechanical properties, and, ultimately, structural degradation [2].

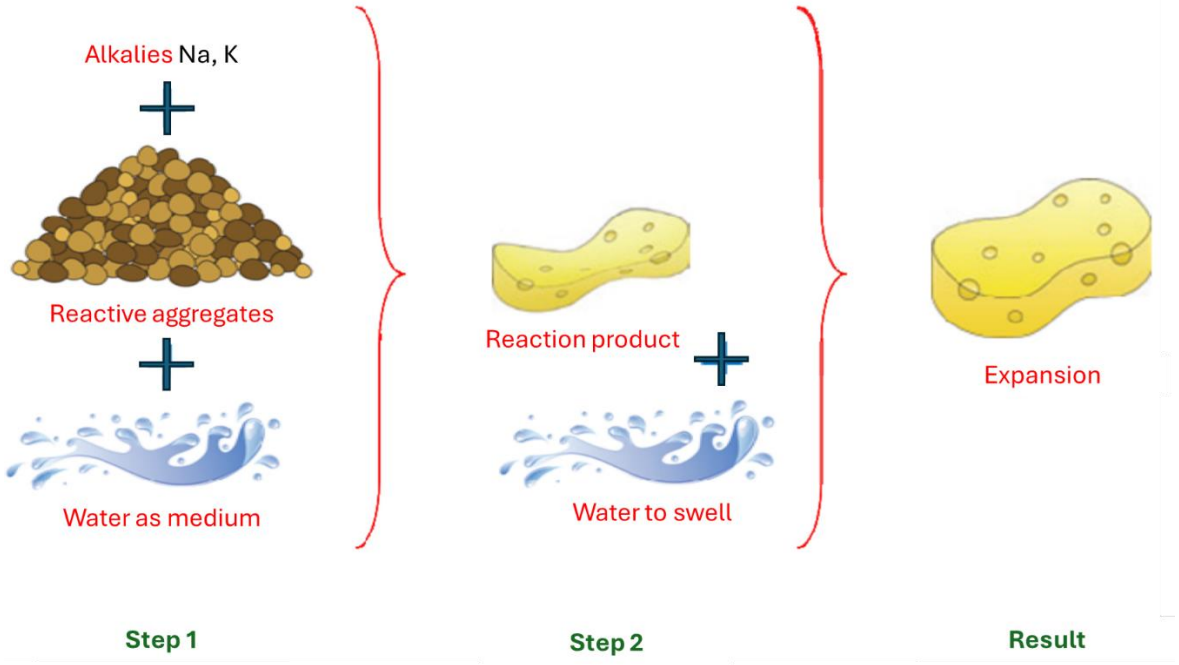

Figure 1 Schematic steps involved in AAR [3]

The complexity of ASR arises from its multi-scale nature, involving chemical reactions at the micro-scale that manifest as macroscopic structural damage. Over the decades, extensive research has focused on understanding ASR mechanisms, developing rapid test methods, predicting long-term performance, and proposing mitigation strategies [4], [5]. Despite these efforts, predicting the structural behaviour of ASR-affected concrete remains a significant challenge due to the intricate interplay between chemical kinetics, material deterioration, and mechanical responses [2], [5], [6].

Various modelling approaches have been developed to simulate ASR effects, categorized broadly into micro-scale, meso-scale, and macro-scale models [7]. Micro-scale models dive into the chemical reactions and ion diffusion processes but are often too detailed for practical structural analysis. Meso-scale models consider the internal pressures and gel production at the material level, requiring extensive microstructural data. Macro-scale models, on the other hand, simulate ASR-induced expansion at the structural level by applying equivalent strains to concrete elements. These models are more practical for engineering applications but may oversimplify the underlying physicochemical processes and material degradation [7].

One of the key challenges in macro-scale modelling is accurately capturing the time-dependent expansion due to ASR and its impact on the mechanical properties of concrete and consequently assessing the resulting structural implications [5], [7], [8], [9]. A well-developed approach is needed to describe the chemical aspects of ASR, including reaction kinetics and expansion

prediction over time. By modelling the ASR expansion as a function of time and environmental conditions, this approach provides a means to incorporate the effects of ASR into structural analyses.

Furthermore, ASR-induced expansion leads to the deterioration of mechanical properties such as the modulus of elasticity and tensile strength [10], [11], [12]. Several studies have indicated that these properties degrade as a function of the level of ASR expansion [10], [11]. Incorporating this deterioration into structural models is crucial for predicting the residual capacity and serviceability of affected structures.

Given the need for practical engineering tools, there is a pressing demand for a modelling approach that is both simple and reliable, enabling engineers to predict the structural behaviour of ASR-affected concrete over time without the complexities associated with detailed microstructural models. Developing a finite element model at the macro scale, coupled with an expansion-time dependent relation and accounting for mechanical property degradation, can address this need by providing a balance between computational efficiency and predictive accuracy.

1.2 Problem Statement

Despite the availability of various models to simulate ASR effects in concrete structures, there remains a gap between detailed scientific understanding and practical engineering application [5], [8], [13], [14], [15]. The problem addressed in this thesis is the lack of a straightforward yet reliable macro-scale modelling approach that incorporates the time-dependent expansion due to ASR, the consequent degradation of mechanical properties, and the resulting structural implications. Specifically, there is a need for a finite element model that:

1. **Simulates ASR-Induced Damage Accurately**: The model should capture the anisotropy of ASR-induced expansion, accurately reflect the development of crack patterns, and account for the effects on the total stiffness of the structure.
2. **Simulates ASR-Induced Expansion Over Time**: The model should be capable of representing gradual expansion levels and correlating them with time, accurately reflecting the progression of ASR.
3. **Accounts for Mechanical Property Deterioration**: The model should incorporate the reduction in modulus of elasticity and tensile strength as functions of the ASR expansion level, reflecting the material degradation observed in ASR-affected concrete.
4. **Provides Practical Utility for Engineers**: The modelling approach should be simple to implement using commonly available finite element software, requiring input parameters that are accessible through standard testing and avoiding unnecessary computational complexity.

By addressing these needs, the thesis aims to develop a macro-scale finite element model that enhances the predictive capability for ASR-affected concrete structures, bridging the gap between detailed scientific models and practical engineering tools. This model will enable engineers to assess the long-term structural performance, plan maintenance and rehabilitation efforts, and ensure the safety and serviceability of concrete infrastructure subjected to ASR.

1.3 Research relevance

The relevance of this research lies in its contribution to improving the modelling and prediction of Alkali-Silica Reaction (ASR) effects on reinforced concrete structures. The Dual Mesh Method (DMM) was initially developed as pre-damage method to simulate ASR induced damage in reinforced concrete. Building upon the DMM, this study introduces the Modified Dual Mesh Method (MDMM), enhancing its capabilities to capture anisotropic expansion and progressive material degradation. Combined with time-dependent material degradation models, the MDMM

provides a simple yet reliable framework for accurate structural assessments. This research equips engineers with valuable tools for more effective infrastructure management, while also informing strategies for the maintenance and rehabilitation of ASR-affected structures.

1.4 Research Aim and objectives

The aim of this research is to model and evaluate the structural behaviour of reinforced concrete structures affected by Alkali-Silica Reaction (ASR) over time, using expansion characteristics derived from experimental results.

To achieve this, the study will first survey relevant literature and software tools to identify effective methods for incorporating ASR-induced degradation and damage into numerical models. It will then focus on developing and enhancing modelling approaches by identifying necessary inputs from micro- and meso-scale levels, including ASR expansion mechanisms and time-dependent material properties, and refining techniques to realistically simulate ASR-induced damage and deterioration. The research will also integrate experimental data and phenomenological models to link numerical models with time-dependent behaviour, enabling accurate long-term predictions while minimizing reliance on extensive physical testing. Finally, a comprehensive framework for structural assessment will be developed by combining the refined modelling techniques with experimental data, providing a robust tool for predicting the safety and performance of reinforced concrete structures affected by ASR.

1.5 Research Scope and Constraints

This research develops a framework for modelling ASR-affected reinforced concrete structures, integrating finite element modelling (FEM) through the Modified Dual Mesh Method (MDMM) and semi-empirical models to simulate ASR expansion and material degradation. The framework focuses on reinforced concrete elements, such as beams and columns, providing a tool for long-term ASR damage assessment. Constraints include reliance on existing literature for parameter validation, limited real-time experimental data, and the assumption of uniform ASR expansion. The framework also does not account for other deterioration mechanisms, such as corrosion, and is limited to FEM software that supports dual mesh configurations.

1.6 Thesis outline

This thesis systematically explores the development of a comprehensive framework for modelling the impact of Alkali-Silica Reaction (ASR) on reinforced concrete structures. **Chapter 1: Introduction** outlines the research problem, objectives, and the importance of studying ASR's effects on structural integrity. **Chapter 2: Literature Review** examines existing research on ASR mechanisms, material degradation, and structural modelling approaches, identifying gaps in current methodologies and providing the foundation for the proposed framework. **Chapter 3: Methodology** describes the step-by-step approach for developing and validating the Modified Dual Mesh Method (MDMM) and integrating it with material degradation models to capture time-dependent ASR effects. **Chapter 4: Structural Model Development** focuses on refining and validating the MDMM, highlighting its capability to simulate ASR-induced anisotropic expansion and material degradation. **Chapter 5: Structural Model Assessment** benchmarks the MDMM against experimental and theoretical models to evaluate its accuracy and practicality. **Chapter 6: Material Models** introduces time-dependent and expansion-dependent degradation models, such as Larive's and Esposito's models, and integrates these into the MDMM framework. **Chapter 7: Comprehensive Framework** consolidates the structural and material models into a unified tool for assessing ASR-affected structures and demonstrates its application through case studies. Finally, **Chapter 8: Conclusion and Recommendations** summarizes the key findings, discusses the contributions to ASR modelling, and proposes directions for future research and practical applications.

2. Literature Review

This literature review is divided into two key sections. The first part examines the mechanisms and impacts of Alkali-Silica Reaction (ASR) on reinforced concrete structures, including ASR-induced expansion and material degradation. The second part reviews existing modelling approaches for simulating ASR effects, providing the foundation for the comprehensive framework developed in this research.

2.1 Alkali Silica Reaction (ASR)

2.1.1 Mechanisms and influencing factors

Alkali-Silica Reaction (ASR) is a complex chemical phenomenon that significantly compromises the durability and structural integrity of concrete structures. At the microstructural level, ASR-induced degradation originates from the formation of a hydrophilic alkali-silica gel. This gel forms through the interaction of reactive silica present in aggregates, alkali hydroxides (primarily sodium and potassium compounds) sourced from the cement clinker, and water within the concrete pore solution [2], [4], [5]. The reactive silica is predominantly derived from the aggregates, while the alkalis originate from both the cementitious matrix and external sources within the concrete [2], [4], [5].

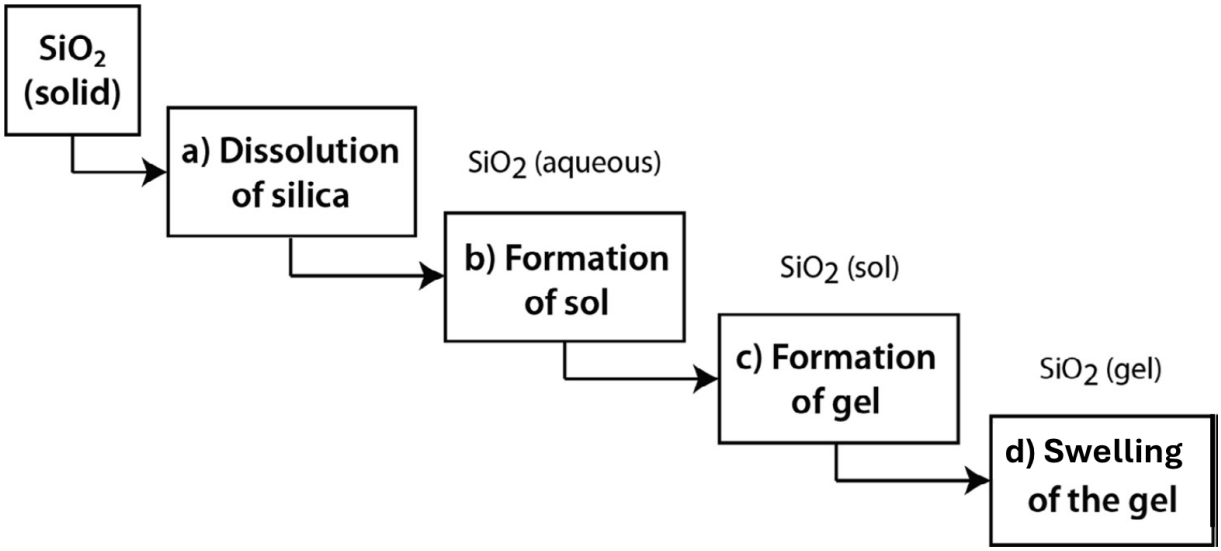

Figure 2 Series of ASR sequential reactions [5]

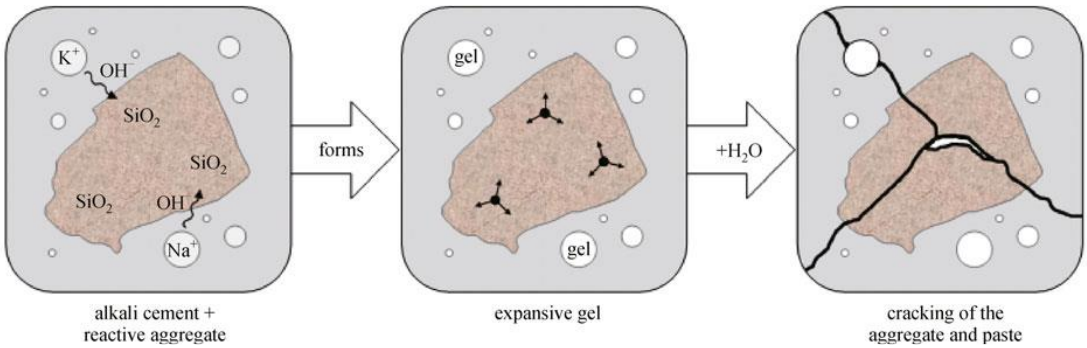

Figure 3 Illustration of ASR mechanism [5].

There are several theories proposed to understand the mechanism of the alkali silica reaction. The ASR process is complex and consists of several stages. A simplified description of ASR, as proposed by various researchers, can be summarized in a series of sequential reactions [4], as illustrated in Figure 2 and Figure 3:

a) **Dissolution of Silica**: Reactive silica in aggregates dissolves in the highly alkaline pore solution, producing silicate ions.

b) **Formation of Sol**: The silicate ions react with available calcium and alkalis, forming a colloidal solution (sol).

c) **Formation of Gel**: The sol undergoes polymerization, forming an expansive alkali-silica gel.

d) **Swelling of the Gel**: The gel absorbs water, swells, and exerts internal pressures, leading to cracking and expansion of the concrete.

Essential Conditions for ASR

For ASR to occur in hardened concrete, three critical conditions must be met [4], [16], Figure 4:

1. **Presence of Reactive Aggregates:**
    - **Reactive Silica Forms:** Aggregates must contain forms of silica that are susceptible to attack by alkali hydroxides. The reactivity is influenced by the mineral composition and the degree of crystallinity of the silica. Poorly crystalline or amorphous silica phases, such as opal, chalcedony, and volcanic glass, exhibit high reactivity.
    - **Particle Size Effect:** The particle size of the aggregates plays a significant role, with smaller particles providing a larger surface area for the reaction, thereby enhancing the susceptibility to ASR.
2. **High Level of Alkalinity:**
    - **Source of Alkalis:** The alkaline environment necessary for ASR is primarily maintained by alkali hydroxides (sodium and potassium) present in the cement paste. Additionally, external sources of alkalinity, such as de-icing salts and seawater, can contribute to the overall alkali content, further promoting ASR.
    - **Alkalinity Measurement:** The sodium equivalent (Na_2Oeq) is commonly used to quantify the alkalinity level in concrete, ensuring that the pH remains sufficiently high to sustain the dissolution of reactive silica.
3. **Sufficient Moisture:**
    - **Moisture Availability:** Moisture is essential for the formation and swelling of the alkali-silica gel. A relative humidity of at least 85% is generally required for ASR to proceed effectively.
    - **Impact on Expansion:** The presence of adequate moisture allows the gel to absorb water, swell, and generate internal stresses that lead to cracking and expansion of the concrete. Environmental conditions, such as climate and exposure to water, significantly influence moisture availability and, consequently, the progression of ASR.

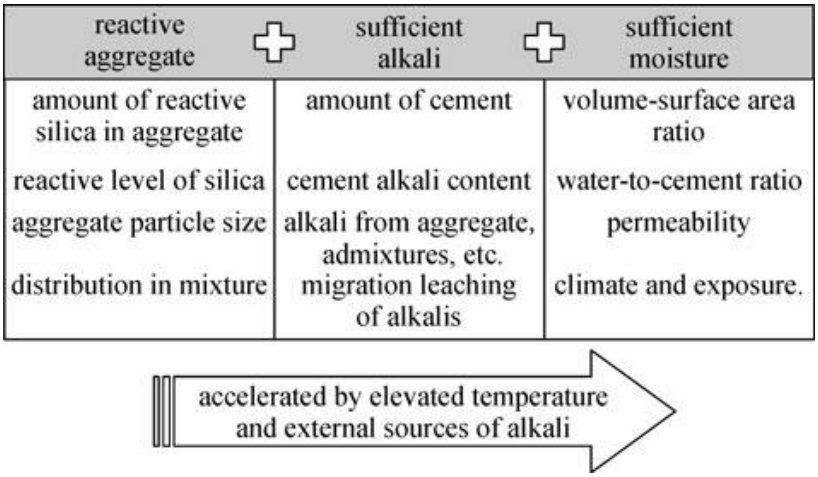

Figure 4 three critical conditions of ASR [4]

Influence of Environmental Conditions

Environmental factors play a pivotal role in the progression and severity of ASR [4], [16]:

- **Temperature:**
  - **Acceleration of Reactions:** Elevated temperatures can accelerate the chemical processes involved in ASR by increasing the reaction rates and enhancing ion mobility within the pore solution.
  - **Climate Impact:** Structures located in warmer climates or subjected to significant thermal variations are more prone to rapid ASR progression.
- **Moisture Dynamics:**
  - **Leaching Effects:** In environments with flowing water or high humidity, alkalis can leach out of the concrete, reducing the overall alkali content and lowering the pH of the pore solution. This leaching effect can decelerate ASR by diminishing the availability of alkalis necessary for the reaction.
  - **Seasonal Variations:** Fluctuations in moisture levels due to seasonal changes can cause intermittent swelling and drying cycles, exacerbating the cracking and expansion phenomena associated with ASR.

2.1.2 Induced expansion

The interplay between the mechanisms and influencing factors of Alkali-Silica Reaction (ASR) results in a dynamic and progressive degradation of concrete structures. A pivotal aspect of this degradation is ASR-induced expansion, which critically impacts the structural integrity of concrete. This expansion can be categorized into two primary types: free expansion and restrained expansion, each exhibiting distinct characteristics and implications for concrete structures.

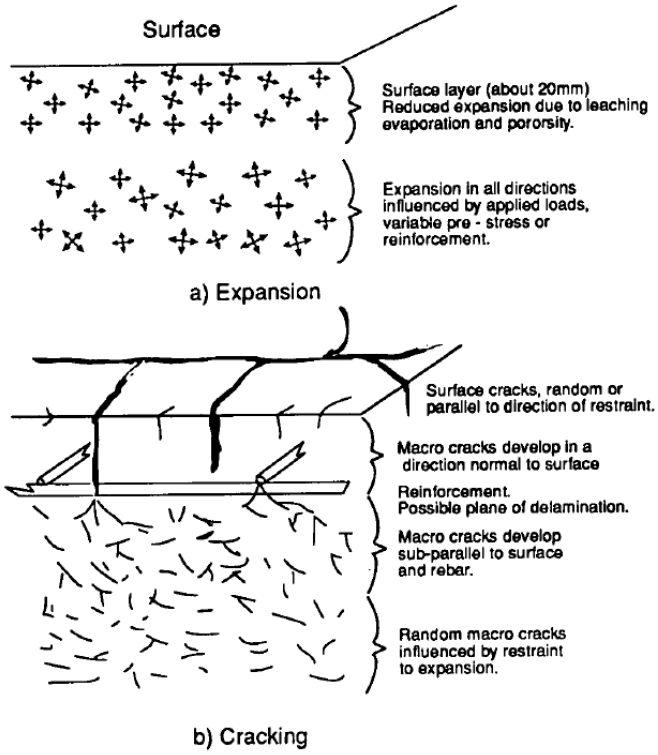

Figure 5 (a) Development of expansion and (b) cracking linked to ASR [17]

ASR causes concrete to expand through the formation of an expansive alkali-silica gel. This gel absorbs moisture and exerts swelling pressure within the concrete matrix, leading to local tensile stresses and potential micro-cracking. When ASR occurs at numerous points within the concrete, it culminates in overall expansion, which varies in both distribution and development over time [16]. The variability in expansion is influenced by several factors, including differences in cement and aggregate sources, variations in cement content and alkali levels, and environmental conditions such as moisture and temperature.

Free Expansion

Free expansion, also referred to as unrestrained expansion, occurs when concrete expands without any physical constraints. This type of expansion is significant for assessing the potential maximum deformation of ASR-affected concrete. The degree of free expansion is influenced mainly by the availability of water, the permeability of the concrete, and prevailing environmental conditions.

Study by Smaoui et al. [18] has demonstrated that ASR-induced free expansion is often anisotropic, exhibiting higher expansion perpendicular to the casting plane. This anisotropy is attributed to the presence of water films under aggregate particles and the orientation of flat or elongated aggregate particles parallel to the casting plane. Larive et al. and Smaoui et al. [18], [19] further explained that these particles trap more water, enhancing expansion in specific directions. However, conflicting findings by Wald et al. , Fan and Hanson , and Mohammed et al. [20], [21], [22] indicated that significant anisotropy in ASR expansion is not always observed. In some cases, such as one instance reported by Wald et al. [20], higher expansion perpendicular to the casting plane was noted, but the authors suggested that the casting direction does not play a major role in the differences observed. This contradiction may stem from the inherent variability and heterogeneity of concrete, which can influence the manifestation of anisotropic expansion.

Restrained Expansion

Restrained expansion occurs when the concrete's expansion is constrained by external factors, such as structural boundaries, reinforcement, or adjacent structural elements. This constraint leads to the development of internal stresses as the concrete attempts to expand against the imposed restrictions. The resultant stresses can exacerbate cracking, deformation, and overall structural misalignment.

Stress Development and Mechanical Property Deterioration

ASR expansion imposes tensile stresses on the reinforcement, which reduces deformation in the rebars. ISE [17] indicated that steel is likely to yield when the reinforcement percentage is less than about 1.6% for mild steel and 0.9% for high-yield steel, Figure 6(a). Studies by Smaoui et al. and Mohammed et al. [21], [23] confirmed the yielding of steel in ASR-affected concrete. However, significant expansion can lead to debonding between the concrete and reinforcement, as observed in experiments [20, 21, 26-29]. This debonding typically occurs when expansion is measured at the concrete surface rather than near the reinforcement.

In reinforced concrete, ASR induces tensile stresses in the reinforcement and compressive stresses in the surrounding concrete, known as chemical prestress. This prestress can be beneficial, limiting expansion and potentially enhancing structural performance. ISE [17] suggested that this compressive stress is generally limited to about 4 MPa. Studies indicate that chemical prestress can positively affect structural behaviour, a topic discussed in more detail in subsequent sections.

Influence of External Restraints

External restraints, such as applied stress, similarly influence ASR expansion. Data collected by Smaoui et al. [23] show that uniaxial compressive stress significantly reduces ASR expansion in the direction of the applied stress, Figure 6 (a). Compressive stress not only restrains expansion but also aligns ASR cracking parallel to the direction of the stress. In contrast, tensile stress increases expansion, although limited data are available on this effect.

Figure 7 from ISE [17] illustrates the crack patterns in ASR-affected beams with different reinforcement configurations. Beams with only bottom reinforcement exhibited map cracking in the unreinforced, unrestrained top region. Conversely, beams with equal top and bottom reinforcement showed cracks parallel to the reinforcement, indicating effective restraint. This difference underscores the importance of reinforcement in controlling ASR-induced expansion and crack propagation.

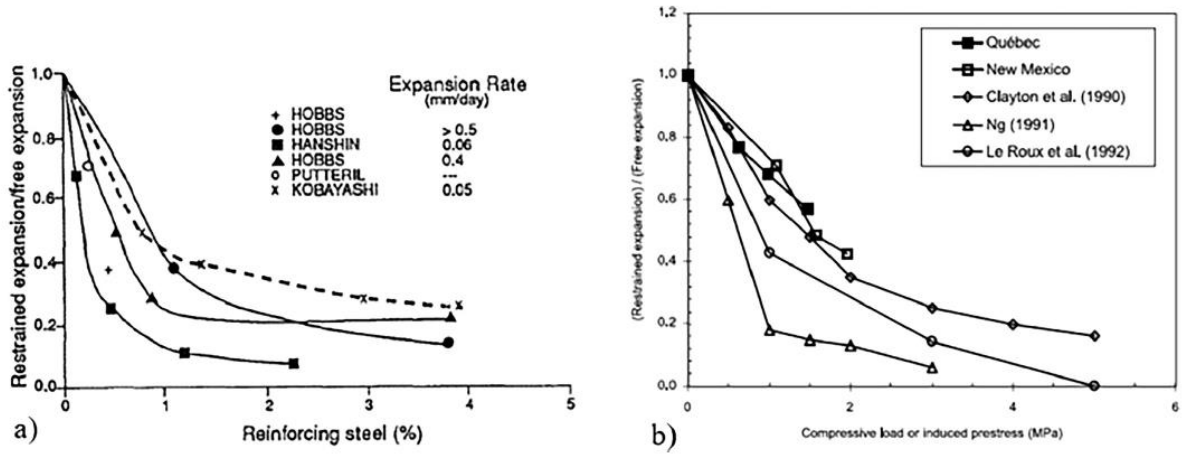

Figure 6 (a) Effects of reinforcing steel on concrete's expansion [17] and (b) effects of confinement on the concrete's expansion [23]

2.1.3 Induced cracking

Alkali-Silica Reaction (ASR) induces cracking in concrete structures, manifesting as both micro-cracks within the concrete mass and macro-cracks on the surface. The development and pattern of these cracks are influenced by factors such as the distribution of reactive particles, internal expansion differentials, and the presence of restraints.

Micro-Cracking and Macro-Cracking

Micro-cracking occurs at the microstructural level due to differential expansion within the concrete. ASR expansion is not uniform throughout the concrete matrix; it tends to be greater near reactive aggregate particles or clusters. This localized expansion generates tensile stresses that exceed the tensile strength of the surrounding cement paste, leading to the formation of micro-cracks. These micro-cracks are randomly oriented in unrestrained concrete but can be influenced by internal restraints and edge conditions.

Macro-cracks develop when micro-cracks coalesce or when tensile strains exceed the concrete's capacity at a larger scale. Surface cracks often manifest as irregular patterns of intersecting and branching cracks, commonly referred to as "map cracking" or "Isle of Man" cracking. This pattern indicates widespread internal distress due to ASR.

Influence of Restraints on Crack Patterns

While the "Restrained Expansion" section discussed how restraints like reinforcement affect ASR-induced expansion and stress development, it's important to note their influence on crack patterns, as illustrated in Figure 7:

- Unrestrained Concrete: Exhibits random micro-cracking and irregular macro-crack patterns due to uniform expansion without constraints.
- Restrained Concrete: Crack patterns are influenced by the direction and degree of restraint. Restraints can alter stress distribution, causing cracks to align parallel to the restraint or to develop in specific patterns reflecting the constraints imposed.

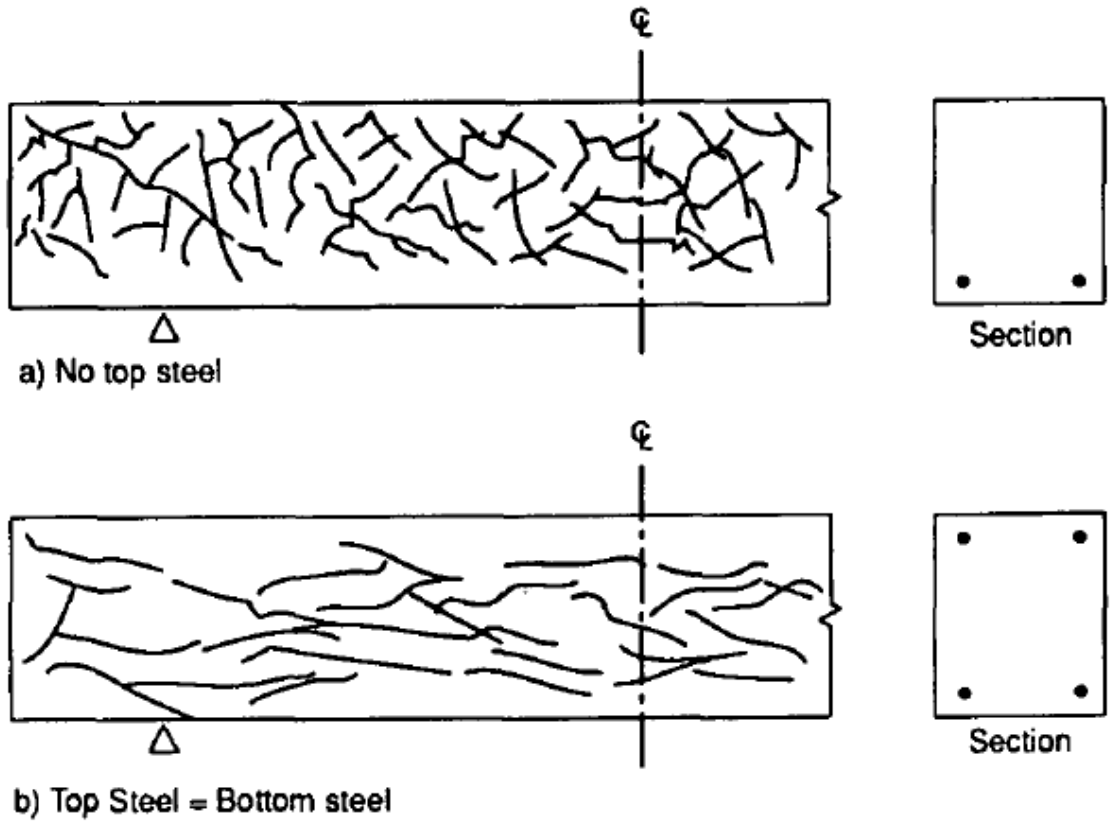

Figure 7 Influence of reinforcement on ASR cracking [17]

2.1.4 Impact on Mechanical Properties

Alkali-silica reaction (ASR) significantly impacts the mechanical properties of concrete by causing internal microcracking and expansion. Young's modulus and tensile strength are particularly sensitive to ASR-induced expansion, showing significant reductions as expansion progresses. Data from ISE [17] summarizes the lower bounds of residual mechanical properties at various ASR expansion levels, Figure 8, demonstrating that Young's modulus and tensile strength degrade rapidly, while compressive strength declines at a slower rate.

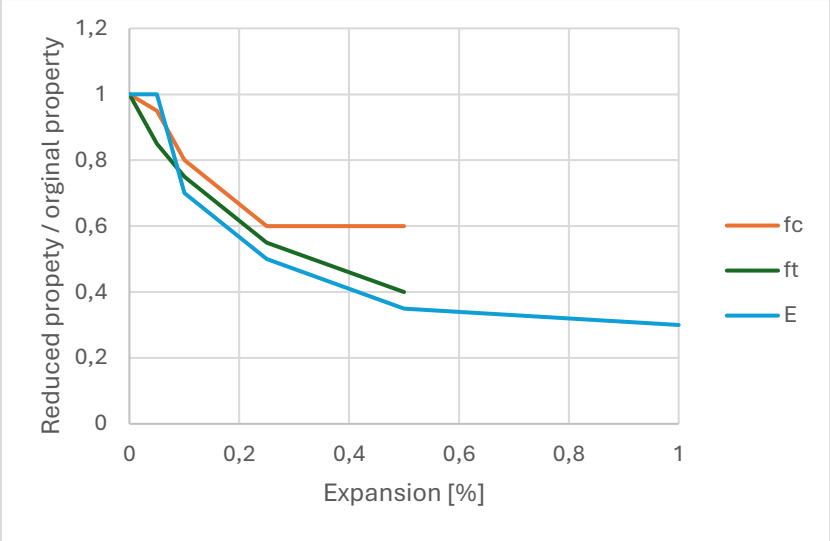

Figure 8 the lower bounds of residual mechanical properties at various ASR expansion levels adapted from [17]; where: f_c is compressive strength, f_t is tensile strength, E is Modulus of Elasticity

Esposito et al. [27] conducted an experimental study and an extensive literature review, finding that Young's modulus is one of the most reliable indicators of ASR-induced damage, potentially dropping to as low as 90% of its original value. Tensile strength, on the other hand, can decrease by about 64% when expansion exceeds 1%. However, some studies, such as Sanchez et al. [28], reported even higher tensile strength reductions. These variations can often be attributed to differences in the aggregate types and cracking patterns. Table 1 shows The classification of ASR damage degrees and the corresponding material property losses are

Table 1 Classification of the damage degree in concrete due to ASR (adapted and reproduced from [28] and cited in [29])

Classification of ASR damage degree (%)	Reference expansion level (%)	Assessment of ASR		
		Stiffness: loss in elastic modulus %	Compressive strength loss %	Tensile strength loss %
Negligible	0.00 - 0.03	-	-	-
Marginal	0.04 ± 0.01	5 – 37	0 – 15	15 – 60
Moderate	0.11 ± 0.01	20 – 50	0 – 20	40 – 65
High	0.20 ± 0.01	35 – 60	13 – 25	45 – 80
Very high	0.30 ± 0.01	40 – 67	20 – 35	50 – 80

2.1.5 Impact on Structural Behaviour of reinforced concrete member

Alkali-silica reaction (ASR) significantly affects the structural behaviour of reinforced concrete beams by altering loading capacity, failure mode, and crack patterns. While ASR leads to noticeable reductions in material properties such as compressive and tensile strengths, these reductions do not always correspond to significant decreases in ultimate load capacity. In some cases, ASR can even increase shear capacity and change failure modes from shear to bending.

Loading Capacity

Significant Reduction in Load Capacity: Research by den Uijl [30] found that beams cut from severely ASR-affected areas of a slab viaduct exhibited a shear capacity of only 75% of the estimated value without ASR damage. This reduction was primarily attributed to the decreased tensile strength caused by ASR, which led to shear tension failures instead of the expected flexural shear failures. Similarly, Aryan et al. [31] documented notable reductions in shear strength and stiffness in ASR-affected beams. They noted that beams with minimal shear

reinforcement were particularly susceptible to increased cracking and deformation under shear loads.

Increase in Load Capacity: Conversely, Ahmed et al. [32] observed that ASR increased the shear capacity of reinforced concrete beams, regardless of the presence of shear links. They explained that the beneficial effects of cement hydration outweighed the detrimental effects of ASR-induced cracking. Good anchorage further reduced expansion and enhanced shear strength, suggesting that proper reinforcement can mitigate some adverse effects of ASR. This finding indicates that, under certain conditions, ASR can lead to improved load capacity. Anca et al. [33] similarly found that in lightly reinforced concrete elements, the internal prestressing effects from ASR expansion sometimes mitigated the reduction in shear capacity.

Minor Reduction or No Change in Load Capacity: Other studies have found that ASR has little to no impact on load capacity. Fan et al. [34] conducted four-point bending tests on beams with various reinforcement ratios and reported that ASR-induced expansion and cracking did not reduce the flexural loading capacity of the beams. This suggests that while ASR severely impacts the mechanical properties of concrete cylinders, its effect on the structural behaviour of reinforced concrete beams is less pronounced. These discrepancies in findings can be attributed to differences in test conditions, reinforcement, and the extent of ASR damage. Similarly, Cao et al. [35] noted that the flexural capacity of reinforced concrete beams, despite ASR-induced microcracking and deterioration, remained largely unaffected due to the structural integrity provided by longitudinal reinforcement.

Influence of ASR on Deflection

ASR impacts the deflection behaviour of concrete beams. Abe et al. [36] investigated the influence of ASR on the flexural yield strength and ultimate shear strength of reinforced concrete beams. They observed a slight reduction in yield strength and a significant reduction in deflection at yield strength in ASR-affected beams. Additionally, there was a shift in failure modes from diagonal shear tension failure in unaffected beams to horizontal slip failure in ASR-affected beams, Figure 9. This change was linked to ASR-induced horizontal cracks altering the stress distribution within the beams.

Ohno et al. [37] noted that while the ultimate flexural strength of ASR-damaged beams was similar to that of unaffected beams, the deflection at yield strength was reduced. These internal defects decreased the beam's ability to deform under load. Similarly, Fan et al. [34] observed that ASR-affected beams had slightly lower deflection and curvature after yielding compared to nonreactive beams, despite similar flexural strengths.

Inoue et al. [38], however, documented that ASR-affected beams exhibited higher flexural cracking strengths due to the internal chemical prestressing effects caused by ASR-induced expansion. This prestressing effect improved the deformability of some ASR-affected beams, particularly in cases with higher reinforcement ratios. Murazumi et al. [39] found that although ASR-affected beams initially exhibited lower stiffness compared to normal beams, as the load increased, the stiffness of the ASR-affected beams surpassed that of the unaffected beams.

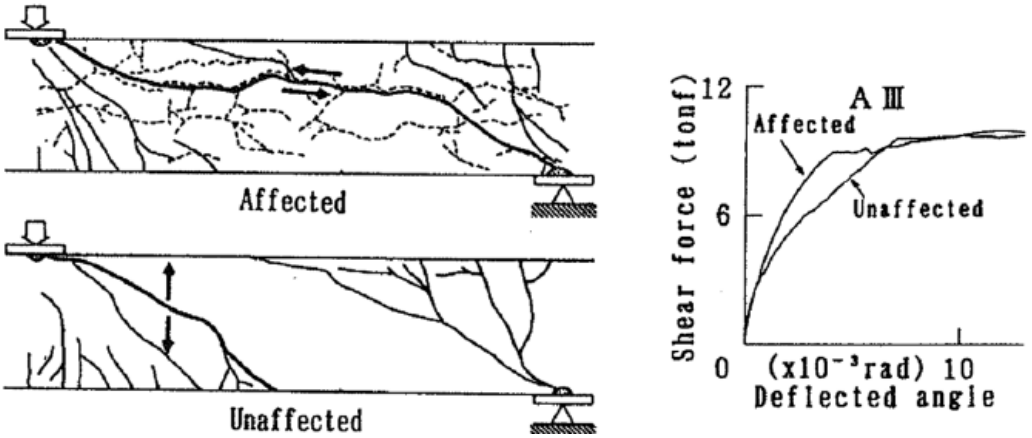

Figure 9 The failure mode shifted from diagonal shear tension in beams not affected by ASR to horizontal slip failure in beams affected by ASR, as reported by Abe et al. [36].

Failure Mode

The failure mode of ASR-affected beams often can change from shear to bending Ahmed et al. [40] found that the provision of shear links in ASR-affected beams increased shear resistance sufficiently to change the failure mode from shear to bending. This shift is due to the compressive stresses induced by ASR expansion, which compensate for the loss in tensile strength and enhance shear resistance. Similarly, Kobayashi et al. [41] observed that beams with high shear reinforcement ratios failed in bending due to concrete crushing, while beams with less shear reinforcement failed in shear.

Inoue et al. [38] presented a special case where the failure mode of ASR-affected beams with a high reinforcement ratio changed from shear in unaffected beams to bending in affected beams. They found that the ASR-affected beams failed in flexure with sufficient ductility, while the unaffected beams failed in shear in a brittle manner, Figure 10. This study emphasizes the critical role of reinforcement in determining failure modes in ASR-affected structures.

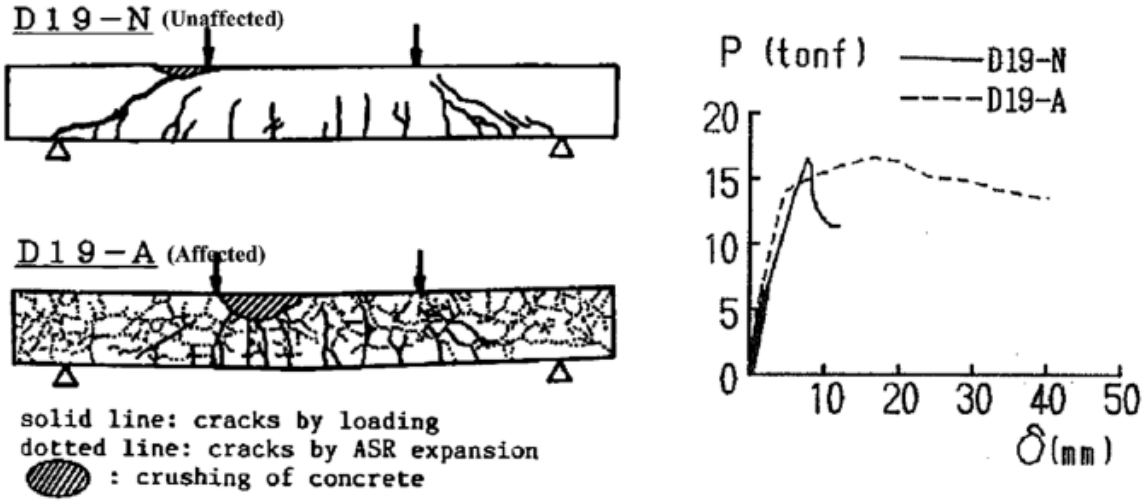

Figure 10 The unaffected beams exhibited shear failure, whereas the affected beams failed in bending, as reported by Inoue et al. [38].

Role of Reinforcement

The mitigating effect of reinforcement on ASR-induced damage is consistently highlighted across studies. Adequate reinforcement not only enhances structural capacity but also influences how ASR affects the beam's behaviour.

Li et al. [24] found that larger reinforcement bars are more effective at reducing ASR expansion, providing greater restraint against internal gel pressures. The presence of stirrups and longitudinal reinforcement reduces concrete expansion stresses and delays the formation of ASR-induced cracks, leading to fewer overall cracks. This interaction significantly influences deflection characteristics and helps maintain load capacity despite material degradation.

Li et al. [26] reported that higher longitudinal and stirrup reinforcement ratios reduce overall volumetric expansion due to ASR. Stirrups provide confinement that delays crack formation and expansion-induced stresses, contributing to shifts in failure modes from shear to bending. The study emphasizes that beams with sufficient reinforcement often maintain higher load capacities and exhibit improved structural performance.

Aryan et al. [31] highlighted that adequate shear reinforcement is crucial in mitigating ASR-induced damage, especially in beams subjected to shear loads. Beams with minimal shear reinforcement were more vulnerable to significant reductions in load capacity, increased cracking, and deformation under shear loading.

Anca et al. [33] emphasized that reinforcement ratios significantly influence the structural performance of ASR-affected elements. Lightly reinforced beams may benefit from internal prestressing effects due to ASR expansion, while heavily reinforced beams maintain reasonable shear performance despite ASR-induced damage.

Overall, reinforcement—both in terms of quantity and detailing—plays a critical role in mitigating the adverse effects of ASR. Adequate reinforcement restrains ASR expansion, delays crack formation, enhances shear resistance, and can alter failure modes, contributing to the maintenance of structural integrity and load-bearing capacity.

Influence of Chemical Prestressing

The influence of chemical prestressing due to ASR expansion on the structural behaviour of concrete beams has been documented in various studies. Inoue et al. [38] reported that ASR-induced expansion introduced significant internal compressive stresses, which improved the shear resistance of ASR-affected beams. This internal prestress also contributed to higher flexural cracking strengths, allowing ASR-affected beams to exhibit higher flexural strength compared to unaffected beams. Kobayashi et al. [41] similarly noted that the chemical prestressing effect prevented the formation of new cracks, thereby enhancing the overall shear resistance of the beams.

2.1.6 Summary

The examination of Alkali-Silica Reaction (ASR) reveals that it is a multifaceted phenomenon with significant implications for concrete structures. The key takeaways from this exploration are:

1. **ASR-Induced Expansion:**
    - **Free vs. Restrained Expansion:** ASR can cause both free expansions, where concrete expands without constraints, and restrained expansion, where internal or external restraints limit expansion and generate additional stresses.
    - **Anisotropy of Expansion:** Expansion due to ASR is often anisotropic. At the material level, this anisotropy arises from factors like aggregate orientation and moisture gradients. At the structural level, anisotropy results from confinement provided by reinforcement, prestressing, external compressive forces, and boundary conditions.
2. **Reduction of Mechanical Properties:**
    - **Elastic Modulus and Tensile Strength:** ASR significantly reduces mechanical properties, with elastic modulus and tensile strength being the most affected. These reductions impact the stiffness and cracking resistance of concrete structures.
    - **Variability in Degradation:** The extent of mechanical property reduction varies depending on factors such as the type of reactive aggregates, degree of ASR progression, and presence of microcracks and its orientations.
3. **Impact on Structural Behaviour:**
    - **Load Capacity:** ASR can lead to no reduction or only slight reductions in load capacity (in some cases increases). In some cases, internal chemical prestressing due to ASR-induced expansion can offset losses in material strength.
    - **Deflection Behaviour:** Deflection can be reduced in ASR-affected structures due to stiffness degradation and internal cracking, affecting serviceability.
    - **Failure Modes:** ASR may alter failure modes, such as shifting from shear to bending failures, influenced by changes in internal stress distributions and material properties.
4. **Influence of Confinement and Reinforcement:**
    - **Confinement Effects:** Confinement, whether provided by reinforcement, prestressing, external loads, or boundary conditions, plays a crucial role in the structural response of ASR-affected concrete. It not only restrains expansion but also influences anisotropy and internal stress development.
    - **Contradictory Findings:** The literature presents differing and sometimes contradictory results regarding ASR's impact. These discrepancies are often attributed to variations in confinement conditions, reinforcement details, and the extent of ASR-induced damage.
5. **Implications for Modelling Approaches:**
    - **Accounting for Confinement and Anisotropy:** Models aiming to predict the structural behaviour of ASR-affected concrete must incorporate the effects of confinement and the resulting anisotropy of expansion. This inclusion is essential for accurately simulating stress distributions and deformation patterns.

- **Influence of Environmental Factors:** Moisture and temperature significantly affect ASR progression and expansion behaviour. Models should be capable of accounting for these environmental influences.
- **Material Heterogeneity:** The inherent heterogeneity of concrete, including variations in aggregate properties and microstructural characteristics, must be considered to capture the localized effects of ASR.

Understanding the complex interplay between ASR-induced expansion, mechanical property degradation, and structural behaviour is critical for developing robust predictive models. Such models should accurately represent the influence of confinement, anisotropy of expansion, environmental conditions, and material heterogeneity. By doing so, engineers can better assess the structural integrity of ASR-affected concrete structures and design effective mitigation and rehabilitation strategies. This comprehensive understanding serves as a foundation for the modelling approaches discussed in subsequent chapters, where these key factors are integrated into analytical and numerical models to simulate the behaviour of ASR-damaged structures accurately.

2.2 Modelling of Alkali-Silica Reaction (ASR)

Building on the understanding of ASR's physical and structural effects from the previous section, this part of the literature review focuses on modelling approaches for simulating ASR in concrete structures. ASR's complexity, from microscopic reactions to structural impacts, demands varied modelling strategies. Despite numerous models, a gap remains between detailed scientific understanding and practical application, particularly in accounting for time-dependent expansion and mechanical property deterioration.

This section categorizes and reviews existing ASR models, highlights their limitations, and lays the groundwork for developing a simplified, reliable macro-scale model. The review is structured into four sections:

- Classification of ASR Models: An overview of models based on scale and principles.
- Structural Models: A review of FEM approaches, focusing on ASR's structural effects.
- Material Models: Analysis of models predicting ASR expansion and its impact on mechanical properties.

This review identifies key factors necessary for developing a practical, effective ASR modelling framework.

2.2.1 Classification of ASR Models

Over the past decades, various models have been developed to simulate ASR, each targeting different aspects of the phenomenon due to its multi-scale nature. Esposito et al. [7], as mentioned earlier, provides a comprehensive classification of existing ASR models into four main categories, which will form the framework for this discussion:

(a) **Macro-Models (based on concrete expansion)**
(b) **Meso-Models (based on internal pressure)**
(c) **Micro-Meso-Models (based on gel production)**
(d) **Micro-Models (based on ion diffusion/reaction products)**

While other researchers might adopt different classification schemes, Esposito's approach is both intuitive and comprehensive, making it a suitable basis for this review.

1. Macro-Scale Models

Macro-scale models simulate ASR-induced expansion at the structural level. They apply strains to concrete elements to mimic the effects of expansive gel production over time. Initially, ASR expansion was modelled as an equivalent isotropic thermal strain, assuming uniform expansion in all directions [7]. However, recent studies have demonstrated that ASR expansion behaves anisotropically, influenced by factors such as aggregate orientation, confinement, and reinforcement.

These models primarily focus on the macroscopic consequences of ASR on structural elements, such as load-bearing capacity, cracking, deformation, reinforcement yielding, and serviceability effects. They are practical for structural engineers analysing large-scale structures, as they abstract the complex chemical processes into mechanical strains applied within finite element frameworks.

2. Meso-Scale Models

Meso-scale models address ASR by simulating internal pressures at the material level. They treat concrete as a heterogeneous material composed of aggregates embedded within a cementitious matrix, possibly including an interfacial transition zone (ITZ). These models directly simulate expansion by representing the swelling pressure of the ASR gel within the microstructure [7]. They require detailed definitions of parameters such as aggregate shape, size, volume fraction, and distribution within a representative elementary volume (REV).

Due to the necessity of detailed microstructural data and consideration of physicochemical processes, meso-scale models are more complex and exhibit greater variability than macro-

scale models. They provide insights into how ASR affects material properties at an intermediate scale, which can influence larger-scale behaviour.

3. **Micro-Meso Scale Models**

Micro-meso scale models operate at the aggregate level, linking gel production processes to the mechanical behaviour of concrete. They capture the strain or pressure imposed on concrete due to gel expansion, integrating physicochemical aspects of ASR [7]. By associating the gel's mass or volume changes with mechanical effects at the aggregate level, these models offer a detailed understanding of how gel production translates into expansion and damage.

4. **Micro-Scale Models**

Micro-scale models provide the most detailed representation, focusing on the diffusion-reaction mechanisms governing ASR gel formation. They meticulously simulate chemical reactions, ion diffusion, alkali leaching, and silica consumption at the microscopic level [7]. While they offer valuable insights into the chemistry of ASR, their complexity makes them less suitable for direct application in structural analysis without integration into larger-scale frameworks.

From a practical engineering perspective, these models can be summarized into two primary categories, [14]:

- **Structural Models (Macro-Scale Models):** These models are directly applicable for structural analysis, addressing the impact of ASR on large-scale structures. They are suitable for predicting load-bearing capacity, deformation, and serviceability issues.
- **Material Models (Meso, Micro-Meso, and Micro-Scale Models):** These models offer a deeper understanding of the chemical and physical aspects of ASR at the material level. They are most effective when integrated into larger-scale models to inform how ASR-induced changes affect material behaviour.

Despite the valuable insights offered by each category, a significant gap exists in developing models that can effectively capture the complex physicochemical nature of ASR while remaining applicable to large-scale structures. Many existing models do not fully account for critical factors such as anisotropic expansion, temperature and humidity variations, and the deterioration of mechanical properties over time. Multi-scale models have been proposed to integrate material-level behaviour with structural performance. However, they tend to be overly complex, computationally intensive, and require extensive data collection, rendering them impractical for routine engineering applications.

2.2.2 Review of Structural Models

Several finite element (FE) models have been developed in recent years to assess the condition of ASR-affected structures and forecast their future behaviour. These models vary in their input and output parameters, depending on their specific focus. Broadly, two types of models can be distinguished: those simulating environmental effects on ASR expansion, and those focused on structural behaviour.

The first type of model uses environmental parameters, such as temperature and moisture, as input to predict strain and stress distributions resulting from ASR. In contrast, the second type of model treats ASR expansion as the input—often estimated or known—and generates output related to structural behaviour, such as load-deflection responses and crack patterns. In alignment with the objectives of this study, the focus will be on the second type of model, which simulates the impact of ASR on structural behaviour.

Farage et al. [42], developed a macroscopic model simulating the behaviour of concrete affected by alkali-aggregate reaction (AAR). Using a smeared crack model within a finite element framework, the model treats concrete as a heterogeneous material. It assumes uncoupling between stress and gel formation, simplifying the interaction between mechanical stresses and chemical reactions. While reducing complexity, this assumption limits the model's ability to capture the full scope of ASR processes. The model was validated against lab-scale tests on reactive concrete samples but did not extend to real-world structural behaviour or account for coupling between stresses and ASR.

Juliani et al. [43], applied a macro-scale model to assess the effects of AAR on concrete pile caps using a finite element model in ANSYS. The model included logarithmic expansion regression to describe concrete swelling over time and modelled ASR expansion as thermal expansion, assuming anisotropy and confinement influences beforehand. While practical for engineering applications, this approach limits the model's predictive capacity over long-term degradation, highlighting the need for continuous monitoring to fully understand ASR effects on structural integrity.

Ferche et al. [44], proposed a macro-modelling approach to analyse the nonlinear behaviour of ASR-affected reinforced concrete structures using a smeared rotating crack model. The model assumes concrete behaves as an orthotropic material under ASR conditions. While it provided reasonable load-deformation response simulations, it failed to accurately capture ASR-induced anisotropic properties and bond degradation. The model's limitations suggest the need for refinements to address non-uniform reductions in mechanical properties, particularly under real-world environmental stresses.

Chen [45], introduced a dual mesh method (DMM) to simulate ASR-affected reinforced concrete beams, focusing on realistic pre-damage conditions such as ASR-induced cracks. The model represents a significant advancement by simulating anisotropic expansion and incorporating chemical prestress caused by ASR. It successfully predicts transitions between failure modes, such as from shear to bending, and integrates pre-existing cracks, providing a more realistic simulation of ASR's impact. However, the study primarily focused on adjusting the dual mesh parameters to fit experimental results, with less attention given to the material properties of ASR-affected concrete. Further investigation and refinement of the dual mesh method are needed to predict long-term structural behaviour accurately. A deeper understanding of the relationship between imposed expansion and material property degradation is essential, along with developing the approach for applications beyond experimental settings.

Gorga et al. [46], developed a finite element approach using ABAQUS to assess a concrete overpass damaged by ASR after 50 years in service. The model combined the mechanical behaviour of concrete with ASR-induced expansion effects, utilizing both the Concrete Damaged

Plasticity (CDP) model and an analytical ASR expansion model. A user subroutine (USDFLD) was implemented to capture the anisotropic expansion of ASR. While the model successfully replicated observed damage patterns and evaluated the residual strength, this was based on specific reduced material properties and expansion levels observed from field data after 50 years of service. Although this demonstrates the model's ability to simulate structural behaviour at a given point in time, it highlights the limitation in forecasting long-term behaviour. The study recommended further research into the combined effects of distress mechanisms such as freeze-thaw cycles and corrosion, as well as refining environmental exposure factors like temperature and relative humidity for more accurate long-term ASR damage predictions.

Vo et al. [47],developed a homogenized finite element model to assess the residual strength of ASR-affected reinforced concrete beams. This meso-scale model simplifies the complex interaction between ASR-induced expansion and reinforcement by homogenizing the concrete matrix and steel reinforcement. Although the model was validated with experimental data, the homogenization approach may oversimplify the interactions between concrete and reinforcement, particularly in more complex structures where detailed modelling of local effects is crucial. This simplification could limit the model's accuracy in capturing the nuanced behaviour of ASR-affected structures under varying conditions.

Alrousan et al. [48], studied ASR-damaged full-scale bridge deck slabs reinforced with Carbon Fiber Reinforced Polymer (CFRP) bars using nonlinear finite element analysis. The study demonstrated the advantages of CFRP reinforcement in improving load-carrying capacity, with the FE models effectively capturing the impact of ASR damage through staged reductions in concrete’s compressive and tensile strengths over time. However, the model treated ASR damage as a global reduction of material properties at different stages, rather than explicitly simulating ASR-induced expansion and anisotropic damage. While this approach provided useful insights into the progression of ASR and its influence on structural failure, it did not account for the localized effects of ASR expansion and cracking, which could be critical for long-term predictions of ASR behaviour.

Kongshaug et al. [49], focused on finite element (FE) modelling of reinforced concrete (RC) beam bridges affected by ASR, aiming to illustrate the load effects caused by ASR expansion on statically indeterminate beam structures. The study emphasized the importance of accurately modelling material constitutive behaviour, including non-linearities such as cracking, creep, and crushing, to assess the structural load effects of ASR. Building on this work, Kongshaug et al. [50], extended the research by developing an inverse problem methodology to estimate ASR-induced stresses based on displacement measurements and crack observations. By integrating both material modelling and back-calculated stress estimations, these studies offer a comprehensive approach to understanding ASR-induced damage in RC structures. However, Kongshaug et al. [50] simplified the ASR expansion as thermal-like linear strain fields and assumed constant environmental conditions, limiting its predictive accuracy in more complex, real-world environments. This simplification calls for further investigation to enhance the approach for more accurate predictions in varied environmental conditions.

The review of previous models reveals that most simulate ASR either as imposed strain or as a global reduction in material properties. Recent models [50, 52-54], have improved accuracy in capturing ASR effects but often require complex implementations using commercial FEM software with specialized subroutines and multiple input parameters. This complexity makes them less practical for routine engineering applications.

In contrast, the Dual Mesh Method (DMM) introduced by Chen [45] offers a more practical solution. It simplifies the implementation process by requiring only a single input for ASR and avoids the need for subroutines. The method effectively simulates ASR-induced damage and physical restraints, irrespective of boundary conditions, besides accurately capturing the anisotropic nature of ASR expansion. Chen's model has shown success in replicating experimental results related to failure mode, load-bearing capacity, and deflection. However, further investigation is required to enhance its predictive capability for long-term structural behaviour.

Additionally, all studies highlight the importance of refining environmental factors, such as temperature and relative humidity, to improve the accuracy of long-term ASR damage predictions.

In summary, while advanced models provide detailed simulations, their complexity limits practical use. Chen's dual mesh approach stands out as a promising alternative, balancing ease of implementation with accurate ASR simulation. Further refinement could lead to a reliable tool for engineers to assess and predict long-term ASR-affected concrete structures.

2.2.3 Review of Material Models

2.2.3.1 Time-Dependent ASR-induced Free Expansion Model

Several empirical and analytical models have been developed to estimate ASR kinetics and the resulting expansion in laboratory settings, which, when combined with numerical analyses, aim to predict the structural implications, such as deformation and stability, of structures and their components [11, 55-60]. Among these models, Larive's semi-empirical model is one of the most widely accepted and utilized by the ASR research community [2, 14, 61-65]. This model, which describes the stress-free expansion evolution, is based on an extensive experimental database of over 600 concrete specimens incorporating various reactive aggregates and exposed to different laboratory conditions [55].

Larive's induced expansion plot typically exhibits an S-shaped curve, which can be divided into four distinct phases, illustrated in Figure 11 (a). The **first phase** represents the formation of AAR-secondary products (e.g., ASR-gel) and their accommodation within reactive aggregates and adjacent cement paste, resulting in minimal to no expansion. The **second phase**, characterized by an ascending curve, signifies the AAR-induced expansion due to moisture uptake by the reaction product. During this phase, expansion occurs with limited cracking, creating an initial convex shape. This phase concludes at the inflection point of the S-curve, beyond which significant deterioration, including cracking within aggregate particles and surrounding cement paste, begins. In **the third phase**, the curve transitions from convex to concave, as the reaction products find additional space (such as cracks and flaws) to occupy, thereby reducing the rate of AAR expansion. The **fourth and final phase** shows a levelling off of the reaction as the system exhausts the total available reactants (alkalis and/or silica) [60]. It's important to note that similar levelling-off trends in laboratory tests might occur not because of the complete consumption of reactants, but rather as a result of alkali leaching [62].

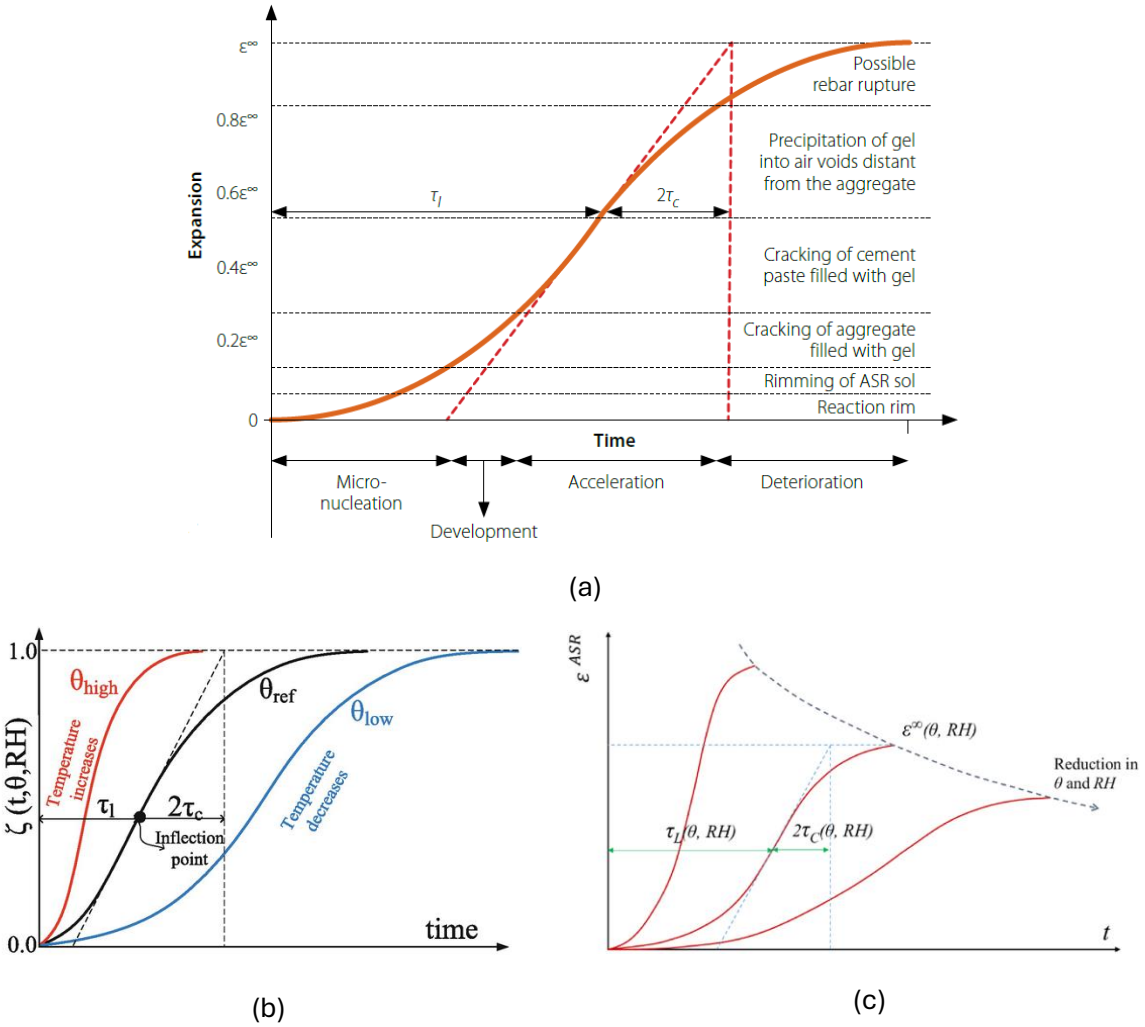

Figure 11 (a) Physical deterioration associated with ASR at stages of the Larive model [29] adopted from [15] (b) ASR-Induced Expansion Curves Considering Temperature (θ) [15], (c)) ASR-Induced Expansion Curves Considering Temperature and relative humidity (RH) [61]

Numerous efforts have been made to enhance the Larive model for predicting Alkali-Silica Reaction (ASR) expansion in concrete by incorporating additional factors such as environmental conditions and material properties. Capra et al. [63] extended the model to account for temperature variations, while Saouma et al. [11] introduced the effects of relative humidity and stress states. Figure 11 (b) and (c) illustrate the influence of temperature variations and relative humidity on the expansion curve. Comi et al. [54] further refined the model by coupling it with concrete saturation levels. Grazia et al. [64] tailored the model to specific aggregate types and reactivity levels. Despite these advancements, the models often require case-by-case calibration and detailed environmental data, which can be difficult to obtain in practical applications. Therefore, for simplicity and due to the unavailability of the necessary data profiles in this research, the original Larive model will be employed without incorporating these additional factors. The explanation of Larive's equation and its parameters, along with its application to develop a time-dependent expansion relationship, will be presented in Chapter 6.

2.2.3.2 Expansion-Dependent Material Deterioration Model

The relationship between ASR-induced expansion and the subsequent degradation of concrete's mechanical properties is a critical area of study for understanding and forecasting the structural impacts of ASR. The research conducted by Esposito et al. [65] provides significant insights into this relationship. Their study, not only clarify the relationship between ASR-induced expansion

and the subsequent decline (or, in some cases, enhancement) of material properties, but also proposes a revised degradation model based on statistical analysis of laboratory test results and available literature. This model refines the degradation law previously proposed by Saouma et al [11], making it more accurate in predicting the behaviour of concrete affected by ASR.

In Esposito et al.'s model [65], tensile strength and elastic modulus are described using an inverse S-shaped curve as functions of ASR expansion, Figure 12. While for compressive strength, a piecewise linear curve was proposed. This model is essential for developing predictive tools for ASR-affected concrete structures, as it effectively captures the material property deterioration across expansion levels, providing critical input for finite element models. A detailed explanation of the model, its parameters and its application will be provided in Chapter 4.

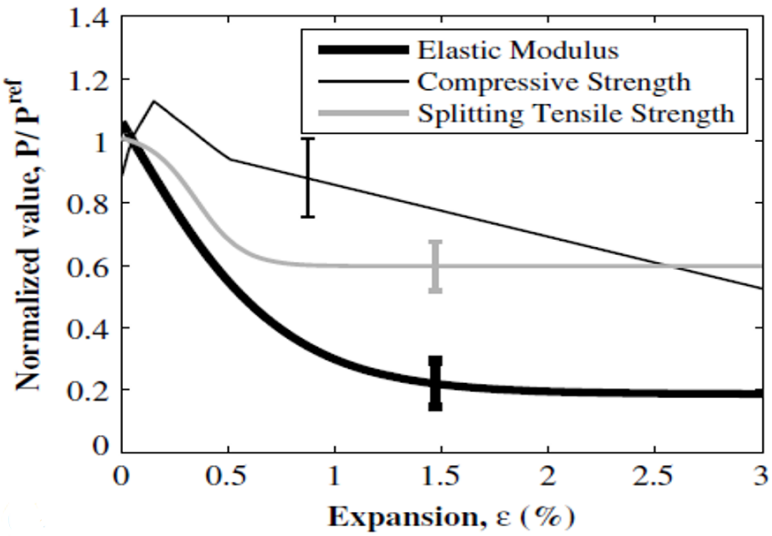

Figure 12 Best curve-fitting results of the relation between normalized properties and concrete expansion of statical analysis of laboratory test results and data available in the literature [27]

2.2.4 Summary

The complexity of Alkali-Silica Reaction (ASR), which spans microscopic chemical reactions to macroscopic structural damage, has led to a variety of models across different scales. ASR models are generally classified into four categories: macro-models, meso-models, micro-meso models, and micro-models. Each category focuses on different aspects of the ASR process, from the diffusion and chemical reactions at the micro-scale to the structural effects at the macro-scale.

From a practical engineering perspective, these models can be split into two main groups:

1. **Material Models (Meso, Micro-Meso, and Micro-Scale Models):**
    - **Focus:** These models simulate the expansion process and ASR kinetics, addressing the chemical and physical changes within the concrete material.
    - **Advantages:** Provide detailed insights into ASR-induced expansion, internal pressures, and gel production, enhancing the understanding of material-level degradation.
    - **Disadvantages:** Highly complex and data-intensive, making them challenging to implement in routine engineering applications due to the extensive microstructural information required.

2. **Structural Models (Macro-Scale Models):**
    - **Focus:** These models simulate the mechanical fracturing and deterioration resulting from ASR-induced expansion at the structural level.
    - **Advantages:** Practical and computationally efficient for large-scale structural analysis, allowing engineers to predict load-bearing capacity, deformation, and serviceability issues.
    - **Disadvantages:** Often oversimplify the underlying physicochemical processes and fail to account for the time-dependent nature of ASR expansion and mechanical property deterioration, potentially leading to inaccurate predictions.

Gap in Existing Models: Despite the advancements in both material and structural models, there remains a significant gap in developing models that effectively capture the complex, time-dependent behaviour of ASR while remaining practical for engineering applications. Existing macro-scale models typically neglect the progressive deterioration of mechanical properties and the anisotropic nature of ASR expansion, limiting their predictive accuracy for long-term structural performance.

Structural Models:

- **Finite Element Models (FEM):** Various FEM approaches have been developed to assess ASR-affected structures, focusing on simulating load-deflection responses, crack patterns, and residual strength. Notable models, such as the Dual Mesh Method (DMM), offer improved simulation of anisotropic expansion and pre-damage conditions but require further refinement for long-term predictions.
- **Implementation Challenges:** Advanced structural models often involve complex implementations with specialized software and numerous input parameters, reducing their practicality for routine use.

Material Models:

- **Expansion-Time Relationships:** Empirical models like Larive's model effectively describe ASR-induced expansion over time but may require calibration for specific cases.
- **Material Property Degradation:** Models by Esposito et al. establish a relationship between ASR expansion and the degradation of concrete's mechanical properties, essential for integrating into structural models.
- **Simplification Needs:** While detailed material models provide deep insights, their complexity necessitates simpler approaches for practical engineering applications, leveraging available experimental data and phenomenological models.

2.3 Software selection

A survey was conducted to select the most suitable software and modelling approaches from a practical and efficiency standpoint. **DIANA FEA** was selected for this research due to its intuitive interface and specialized functionalities that closely align with the research's requirements. The software's extensive library of pre-defined material models and robust capabilities in nonlinear analysis provide an efficient and reliable platform for conducting the finite element analyses essential to this study. In **Appendix B**, a detailed comparison between the three most well-known software platforms—**DIANA FEA**, **ABAQUS**, and **ANSYS**—is provided, illustrating the strengths and limitations of each and further supporting the selection of DIANA FEA for this research.

2.4 Conclusion

The literature review underscores the complex, multi-scale nature of Alkali-Silica Reaction (ASR) and the existing limitations in current modelling approaches. Material models offer detailed insights but are impractical for routine engineering use, while structural models provide practical applications yet often overlook time-dependent expansion and property degradation. Additionally, the software selection highlights the need for an intuitive and efficient finite element tool to implement the desired macro-scale modelling effectively.

Aligning with the thesis aim, this study adopts a novel dual mesh approach within a macro-scale finite element framework. The dual mesh method enhances traditional macro-scale models by accurately simulating anisotropic ASR expansion. Furthermore, this study will integrate expansion-dependent mechanical property degradation and couple the expansion with a time-based free ASR expansion correlation, achieving this without the excessive complexity of detailed material models. This innovative methodology bridges the gap between detailed scientific understanding and practical engineering application, providing a solid foundation for accurately predicting the long-term behaviour of ASR-affected concrete structures. Consequently, it enables engineers to effectively assess, maintain, and rehabilitate impacted infrastructure with greater accuracy and confidence.

3. Methodology

This chapter outlines the methodological framework adopted to develop a practical and reliable macro-scale finite element model for simulating the structural behaviour of reinforced concrete structures affected by Alkali-Silica Reaction (ASR) over time. The methodology comprises four interconnected phases: **the literature and tool survey**, **structural model development**, **material models integration**, and **the final framework for coupling structural and material models**. These phases work in parallel and interactively to bridge the gap between detailed scientific models and practical engineering tools, enabling engineers to effectively assess long-term structural performance.

The **first phase** involves an extensive review of existing literature and finite element software to understand the mechanisms of ASR and its impact on concrete and reinforced concrete structures. This phase also examines various modelling techniques across different scales—micro, meso, and macro—to identify the most suitable approach for simulating ASR effects in reinforced concrete structures. The review helps in selecting finite element software that meets the research's requirements for accurately simulating ASR effects, considering factors such as user interface, material models, and computational efficiency.

The **second phase** focuses on the systematic development of the structural model. A numerical modelling approach was adopted, starting with the investigation and enhancement of **the Dual Mesh Method (DMM)**. This method was further advanced into the Modified Dual Mesh Method (MDMM), which incorporates several key features. The DMM utilizes two meshes: a primary mesh to represent the concrete material and captures structural behaviour, and a secondary mesh to simulate ASR-induced expansion effects. Initial strains equivalent to ASR-induced free expansion are incrementally applied to the secondary mesh and transferred to the primary mesh, simulating anisotropic expansion and internal stresses. **The constitutive model** integrates the relationship between expansion and material degradation to account for reduced mechanical properties due to ASR, while **phased analysis** minimizes unnecessary stiffness from the secondary mesh, ensuring the model reflects realistic loading conditions and ASR progression over time.

The structural model was validated through simulations on concrete cube elements under various scenarios, testing its ability to capture ASR-induced anisotropic expansion, material degradation, and resulting stresses and strains. The progression of ASR over time is simulated by externally applying the expansion-time relationship, correlating incremental ASR-induced strains in the secondary mesh with specific time steps based on phenomenological models and experimental data.

The model’s performance was further assessed using a benchmark structure commonly used for validating FEM models, providing a standardized reference in a realistic setting. Comparative analyses with alternative methods confirmed the MDMM’s consistency with theoretical expectations and its accuracy in simulating ASR effects on key structural responses, including load capacity, deflection behaviour, and failure modes, confirming the model's validity in real-world applications.

Parallel to the structural model development, the **third phase** involved the integration of material models to establish relationships between ASR-induced expansion, time, and material property degradation. Realistic data from case studies were essential to illustrate how these relationships can be established, as they provide practical examples of ASR progression and its effects on material properties. The Larive model was employed to describe the expansion-time relationship

of ASR in concrete. For simplicity and due to the unavailability of detailed environmental data, additional factors like temperature and relative humidity were not incorporated. While Esposito et al.'s model linked ASR-induced expansion to the degradation of material properties within the concrete constitutive model. Case study data and literature findings were utilized to refine these models, ensuring a realistic representation of the time-dependent behaviour of ASR-affected materials.

In the **final phase**, the previously developed structural and material models were assembled to create a comprehensive modelling framework. This step consolidates all components, allowing for a unified approach to simulating the effects of ASR on reinforced concrete structures. This framework visually represents the interactive phases and key components of the research approach, providing a comprehensive overview of the process.

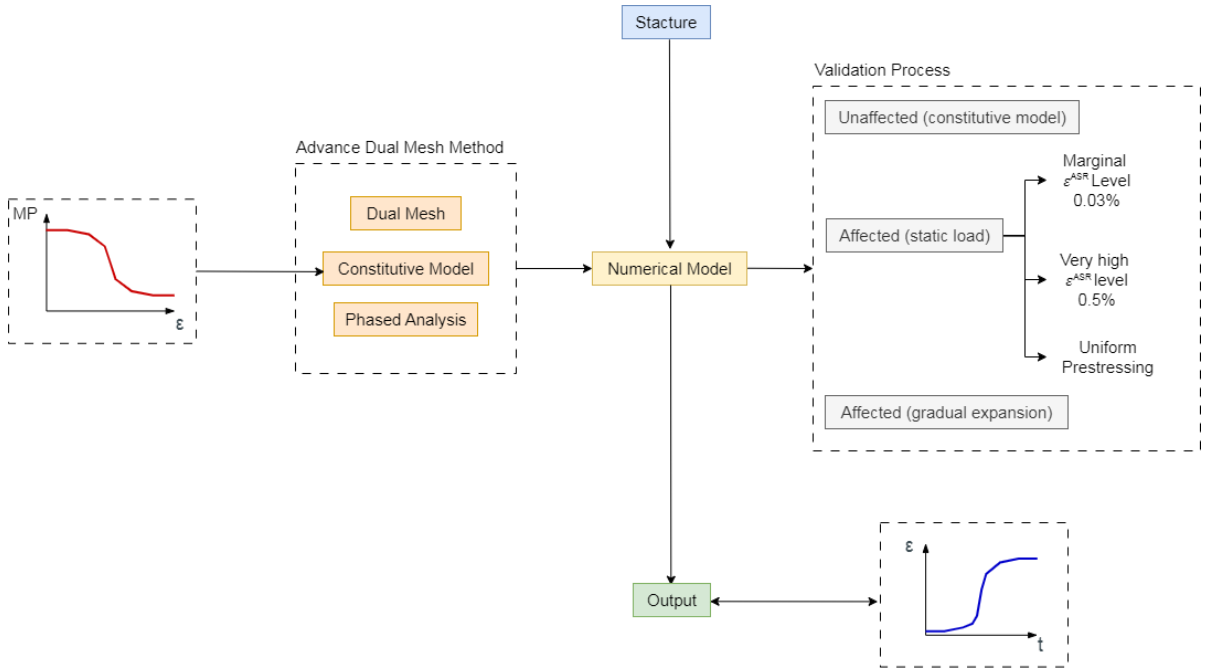

Figure 13 Overview of the Methodology.

4. Structural Model Development

This chapter focuses on developing a numerical modelling approach to simulate the long-term structural behaviour of reinforced concrete structures affected by Alkali-Silica Reaction (ASR). Building on the Dual Mesh Method (DMM) introduced by Chen [45] ,the method is adapted and refined to address specific challenges related to ASR-induced damage.

The chapter begins with an explanation of the DMM concept and highlights the adaptations made in this research to align the method with the requirements for long-term structural analysis (Section 4.1). Numerical investigations are conducted to examine the mechanism of the DMM, including the effects of expansion anisotropy and material property degradation (Section 4.2). An Adapted Tensile Curve (ATC) is introduced to represent the degradation of tensile strength due to ASR expansion (Section 4.3). Additionally, phased analysis is utilised to allow accurate representation of structural conditions (Section 4.4).

Together, these advancements form the foundation for a Modified Dual Mesh Method (MDMM), which integrates the DMM, ATC, and phased analysis to simulate ASR-affected structural behaviour with improved accuracy and predictive capability.

4.1 Dual Mesh Method Concept

The Dual Mesh Method (DMM), also known as the Double Mesh Method, offers a noval approach to finite element modelling by incorporating two overlapping meshes—a Primary Mesh (structural mesh) and a Secondary Mesh (shadow mesh)—within the same physical space and therefore undergo the same kinematics [49, 70-73]. These meshes share nodes but consist of distinct elements, allowing different material properties to be assigned to each. Figure 14 illustrates a 2D representation of this concept.

The structural mesh represents the primary system and is assigned non-linear material properties to simulate the complex mechanical behaviour of concrete under stress. The shadow mesh, configured with linear-elastic properties, introduces strain loading to model ASR-induced expansion. Despite the increased number of elements, the shared nodes ensure that both meshes experience identical deformations, governed by the combined stiffness of the structural and shadow meshes. Chen [45] demonstrated the interaction and mechanics of the two meshes through analytical 1D and 2D solutions, providing foundational insights into the DMM's functionality. A summary of this work is reviewed in Appendix B, and for comprehensive details, the reader is referred to Chen's original publication [45].

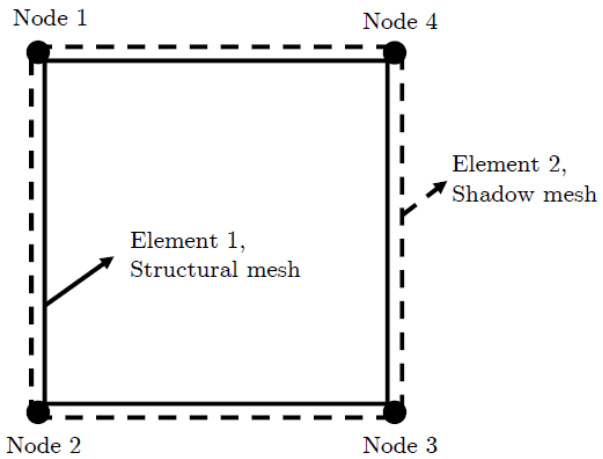

Figure 14 Simple 2D illustration DMM representing 4 shared nodes of dual elements [45]

ASR-induced damage is modelled by applying strain to the shadow mesh. These strains are transferred to the structural mesh through shared nodes, simulating the effects of expansion forces. The shadow mesh introduces directional pre-strains, influenced by the constraints of the structural mesh, thereby mimicking the anisotropic nature of ASR-induced expansion.

A key difference between this study and Chen's earlier work lies in the application and adaptation of the DMM. Chen [45] used the DMM as a pre-cracking technique, where shadow mesh parameters were calibrated to match experimental crack patterns. This approach suited experimental scenarios where ASR damage was introduced before structural loading. However, for real-world structures subjected to ASR while in service, the progression of damage occurs post-loading. To address this, the current study modifies and applies the DMM as a post-damage method, simulating ASR-induced damage incrementally.

In addition to adapting the DMM, this research aims to address areas not fully illustrated in Chen's work. While Chen provided explanation of the fundamental mechanics of the DMM, the numerical aspects and illustrative implementation of the method were not extensively demonstrated. This study builds upon Chen's foundational work by offering detailed numerical investigations to illustrate how the DMM functions within finite element analyses. Furthermore, original work did not explicitly link ASR expansion levels to material property degradation—an aspect critical for predicting long-term structural behaviour. This study addresses this gap by integrating expansion-based degradation into the DMM framework, enabling its application for time-dependent structural assessments.

Another distinction is the treatment of shadow mesh properties. In DMM approach, the shadow mesh's modulus of elasticity and Poisson’s ratio were adjusted for each case to match experiments. In this study, the shadow mesh modulus of elasticity is kept constant, and the Poisson’s ratio is set to zero to ensure uniform directional expansion on the structural mesh. This approach eliminates numerical artefacts in simulating anisotropy by basing anisotropy effects only on the structural configuration, ensuring more reliable and consistent results.

The methodology introduced here applies strain loading incrementally, correlating each increment to a specific ASR expansion level. The structural mesh is calibrated to reflect the progressive degradation of concrete material properties over these increments. By transitioning the DMM from a pre-damage to a post-damage modelling tool, this study expands its applicability to real-world structures and provides a pathway for long-term predictions of ASR-affected reinforced concrete behaviour.

4.2 Numerical Exploratory Study: Implementation and Evaluation of the DMM

This section focuses on the numerical implementation of the DMM, with the following objectives:

1. To numerically illustrate the DMM concept.
2. To understand the mechanism of stress generation under both linear and nonlinear analyses.
3. To evaluate the model's capability to capture anisotropy of expansion at structural scale due to ASR.
4. To investigate the model's capacity to simulate material degradation resulting from induced expansion.

To achieve these objectives, a comparative numerical study is conducted using a 2D plain concrete cube model to ensure clarity and simplicity in analysis. The investigation begins by illustrating the DMM concept and exploring stress generation mechanisms. Two approaches are compared: (1) the Single Mesh Method (SMM), where expansion is applied directly to the concrete mesh, and (2) the DMM approach, where expansion is introduced via the shadow mesh. These approaches are analysed under both linear and nonlinear conditions to understand their differences.

Next, the model's ability to capture anisotropic expansion due to ASR is evaluated. This is achieved by comparing the 2D plain concrete cube model with a modified version that includes a single steel rebar to introduce directional restraint. This analysis will highlight how structural configuration influences anisotropy in expansion.

Finally, the degradation of tensile strength and modulus of elasticity (E-modulus) due to incremental ASR-induced expansion is investigated. The stress-strain state of the plain concrete model is examined to observe property reductions.

In all simulations, an initial strain of 1% is applied incrementally to the shadow mesh, enabling a detailed evaluation of the DMM's capacity to simulate ASR effects accurately.

4.2.1 Model Description

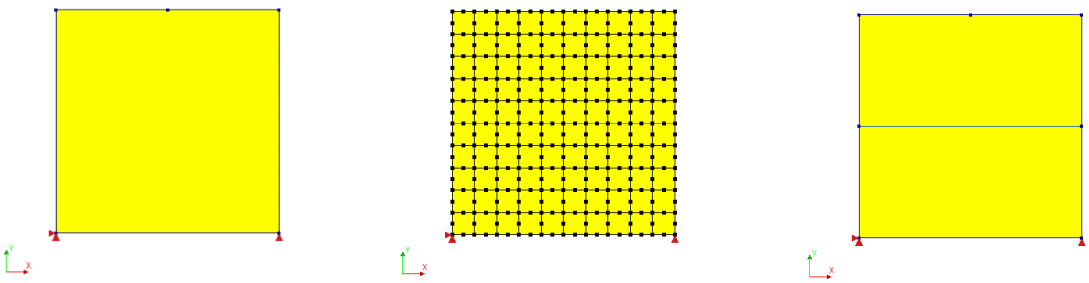

(a) (b) (c)

Figure 15 The used finite element model 100x100 mm; (a) plain concrete model, (b) quadratic mesh of the model, and (c) restraint model with single steel rebar.

The model represents a concrete cube with dimensions of 100 mm by 100 mm and a thickness of 100 mm, as shown in Figure 15. This simple geometry allows the focus to remain on the conceptual differences between SMM and DMM, avoiding the complexity of more intricate models (full structural scale). The cube is simply supported to allow for free deformation. Two

different loading scenarios are investigated in both linear and nonlinear analyses: strain directly applied to the concrete mesh (SMM) and strain applied to the shadow mesh (DMM). To simulate the cracking behaviour of concrete, a rotating smeared cracking model is employed, with the shadow mesh assumed to be elastic, possessing an elastic modulus equal to 2% of that of concrete, as it was proposed by Chen [45].

Table 2 summarises the material properties, and Figure 16 provides a simplified model description. The model input for tensile behaviour (Tensile Curve) is shown in Figure 17. Detailed information about the model setup and parameters can be found in Appendix C.

Table 2 Material properties of concrete, Shadow mesh, and the steel rebar

Material	Parameter	Input
Concrete	Young's modulus (E_c)	33950 MPa
	Poisson's ratio (v)	0.2[1]
	Compressive strength (f_{cm})	45 MPa
	Tensile strength (f_{tm})	4.11 MPa
Shadow mesh	Young's modulus (E_{DM})	2% E_C MPa
	Poisson's ratio (v)	0
Steel rebar	Young's modulus (E)	200000 MPa
	Yielding strength (f_{ym})	450 MPa
	Ultimate strength (f_{um})	540 MPa
	Ultimate strain (ε_{su})	0.05

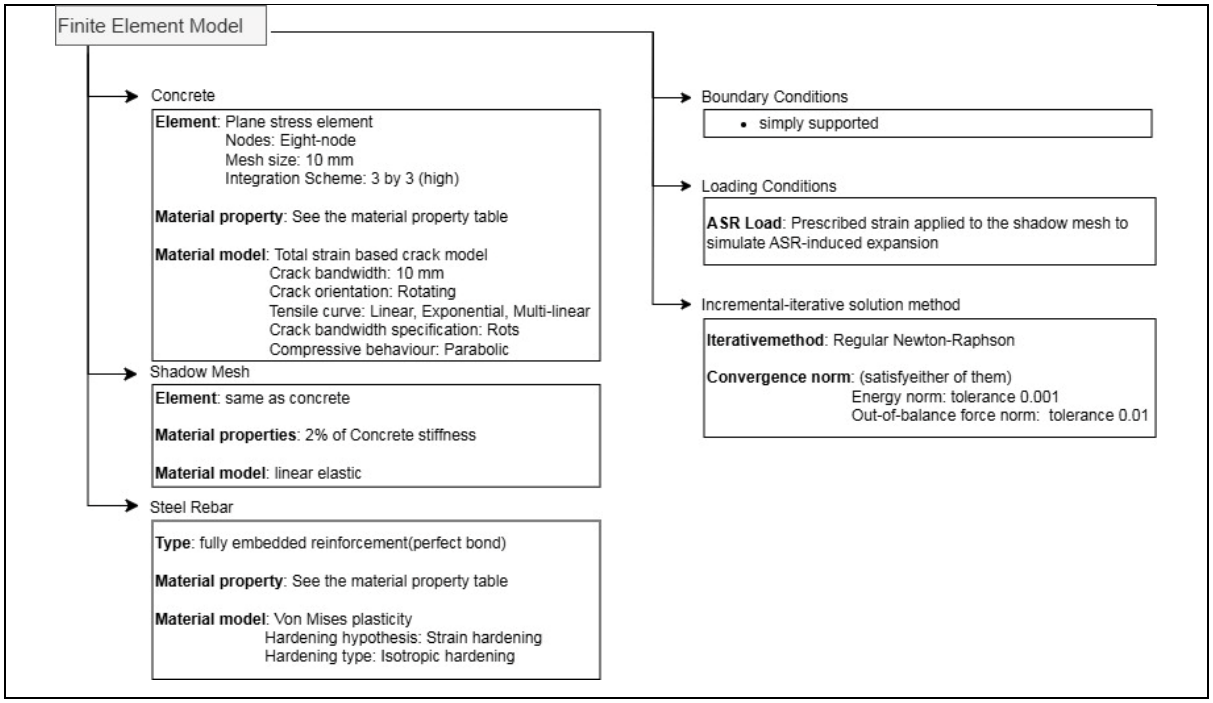

Figure 16 Finite Element Model Description of the 2D cube

[1] It should be noted that, for the first two objectives, the concrete Poisson's ratio is set to 0. This adjustment allows verification of the model against the analytical solution proposed by Chen [45].

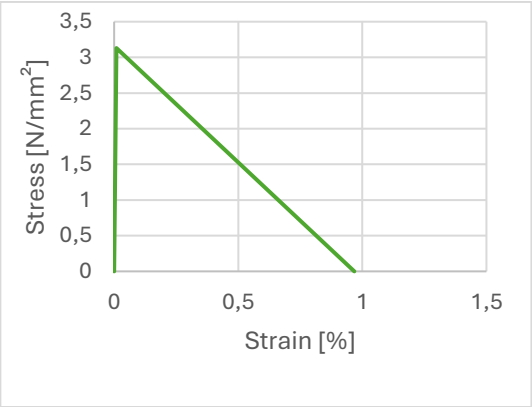

Figure 17 Model input for Tensile Curve

4.2.2 Results & Discussion

4.2.2.1 Linear Analysis of Expansion Behaviour

Figure 18 presents the linear analysis results comparing the Single Mesh Method (SMM) and the Dual Mesh Method (DMM), including contour plots of displacement in the x-direction (Dtx) and y-direction (Dty), and vector plots of principal total strains (E) and principal total stresses (S).

When a 1% initial strain is applied in both cases, both methods exhibit displacement (elongation) in both directions. In the SMM, the total displacement, shown in Figure 18 (a) and Figure 18(c), is equivalent to the 1% initial strain applied, as depicted in Figure 18(e). In contrast, the DMM results in displacement due to the interaction between the stiffness of the structural mesh (K_{st}) and the shadow mesh (K_{sh}), as described by the analytical solution proposed by Chen [45] in Equation (1):

$$\Delta_{st} = \frac{K_{sh}}{K_{sh} + K_{st}} \Delta_0 \quad (1)$$

where Δ_{st} represents the final displacement of the structural mesh, Δ_0 is the initial applied displacement, K_{sh} is the stiffness of the shadow mesh, and K_{st} is the stiffness of the structural mesh [45]. The final displacement is determined by the relative magnitudes of K_{st} and K_{sh} [45].

The results from the DMM simulation align with Equation (1), particularly when the Poisson's ratio is set to zero, as shown in the comparison. This consistency validates the model's implementation in linear analysis. Specifically, the displacement distribution in the DMM, shown in Figure 18(b) and Figure 18(d), results from the interplay between the stiffness of the two meshes, while the SMM directly applies the initial strain to the concrete mesh.

Notably, while both methods simulate displacement, only the DMM generates internal stresses, as shown in Figure 18(h). This occurs because the shadow mesh restrains the expansion of the structural mesh, effectively simulating the stress development caused by ASR-induced expansion.

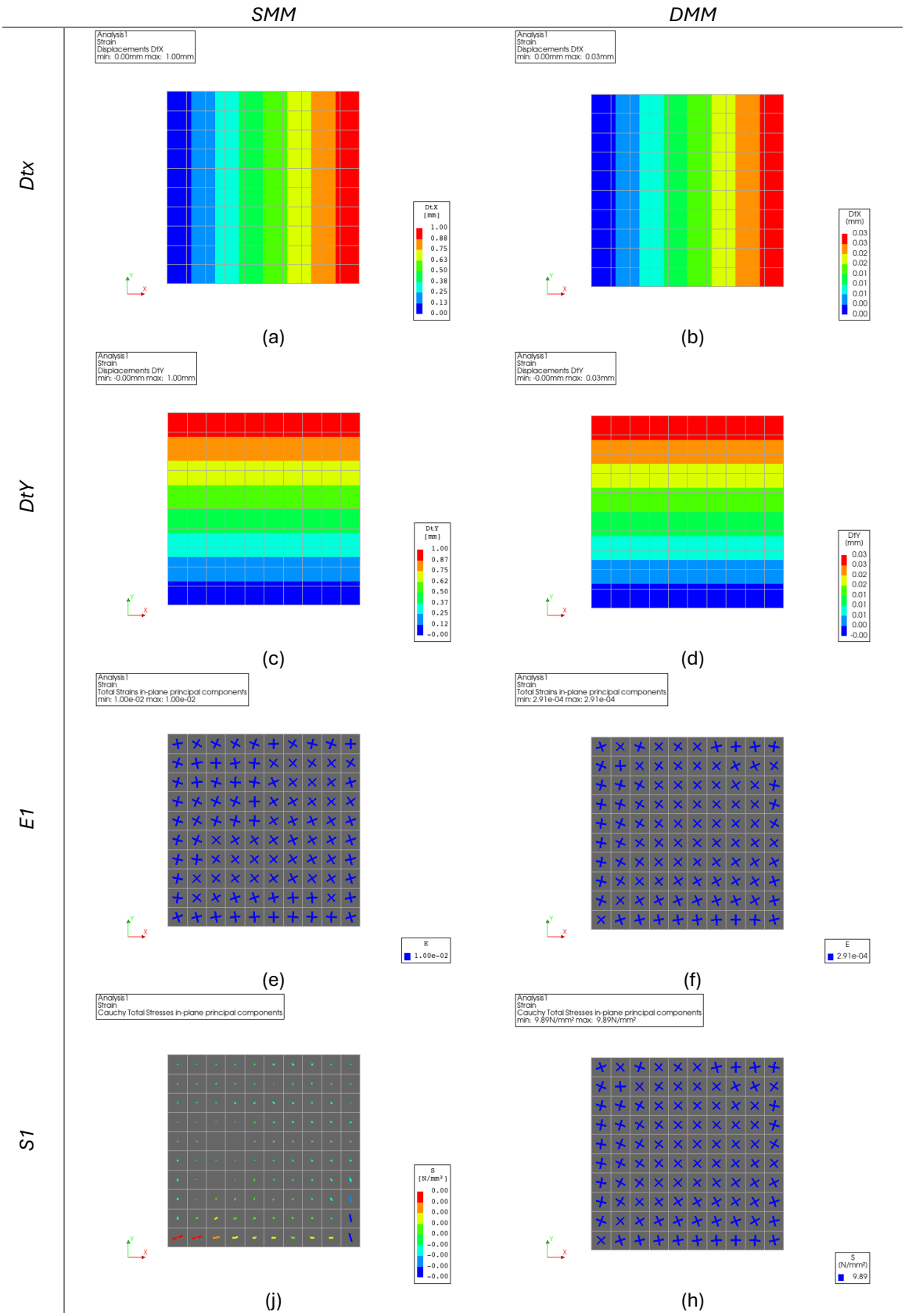

Figure 18 Linear analysis results comparing Single Mesh Method (SMM) and Dual Mesh Method (DMM); where Dtx is displacement in the x-direction, Dty is displacement in the y-direction, E1 is principal total strains, and S1 is principal total stresses.

4.2.2.2 Nonlinear Analysis of Expansion Behaviour

In nonlinear analysis, unlike the linear case where deformation results from the interaction between the structural mesh and the shadow mesh with both stiffnesses influencing deformation, induced cracks in the structural mesh reduce its stiffness, making the interaction between the meshes a dynamic process. Figure 19 presents the nonlinear analysis results comparing the Single Mesh Method (SMM) and the Dual Mesh Method (DMM), showing displacement in the x-direction (Dtx) and y-direction (Dty). Figure 20 compares the stress-strain input and output, displaying total principal strains and stresses on the structural mesh versus load factor of applied 1% initial strain, as well as cracking strain versus load factor. Figure 21 illustrates the development of free expansion in the structural mesh with respect to the initial strain. The striped line represents a reference line where the increase in expansion equals the increase in initial strain, occurring when the structural mesh stiffness (Kst) is zero.

The observed free expansion behaviour can be divided into three stages based on two distinct kinks (A: maximum tensile strength, and B: ultimate strain) in the curve shown in Figure 21:

- **Stage 1 (0 to Point A):** A linear stage from the beginning until the onset of cracking, with almost no expansion occurring.
- **Stage 2 (Point A to Point B):** From the onset of cracking to when the concrete reaches its ultimate strain capacity. Cracking reduces the structural mesh stiffness (Est), leading to observable expansion. As cracking progresses, Est continues to decrease.
- **Stage 3 (Point B to 1% strain):** The structural mesh is completely cracked with no remaining stiffness, and only the shadow mesh stiffness contributes to the behaviour.

These results demonstrate that the DMM has the capability to simulate the imposed damage due to ASR-induced expansion. It should be noted that no reaction forces at the supports are observed in both the SMM and DMM analyses.

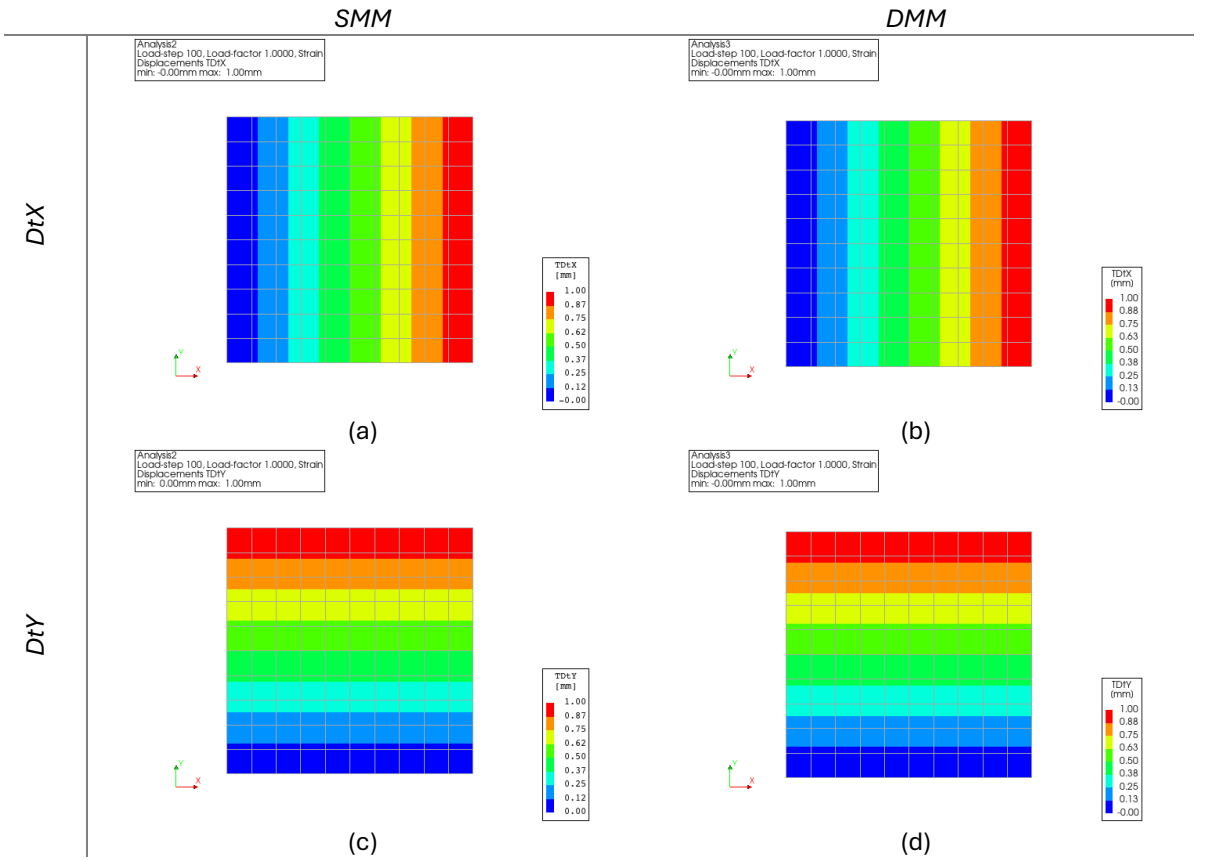

Figure 19 Nonlinear Analysis Results Comparing Displacements in the x-direction (Dtx) and y-direction (Dty) for Single Mesh Method (SMM) and Dual Mesh Method (DMM).

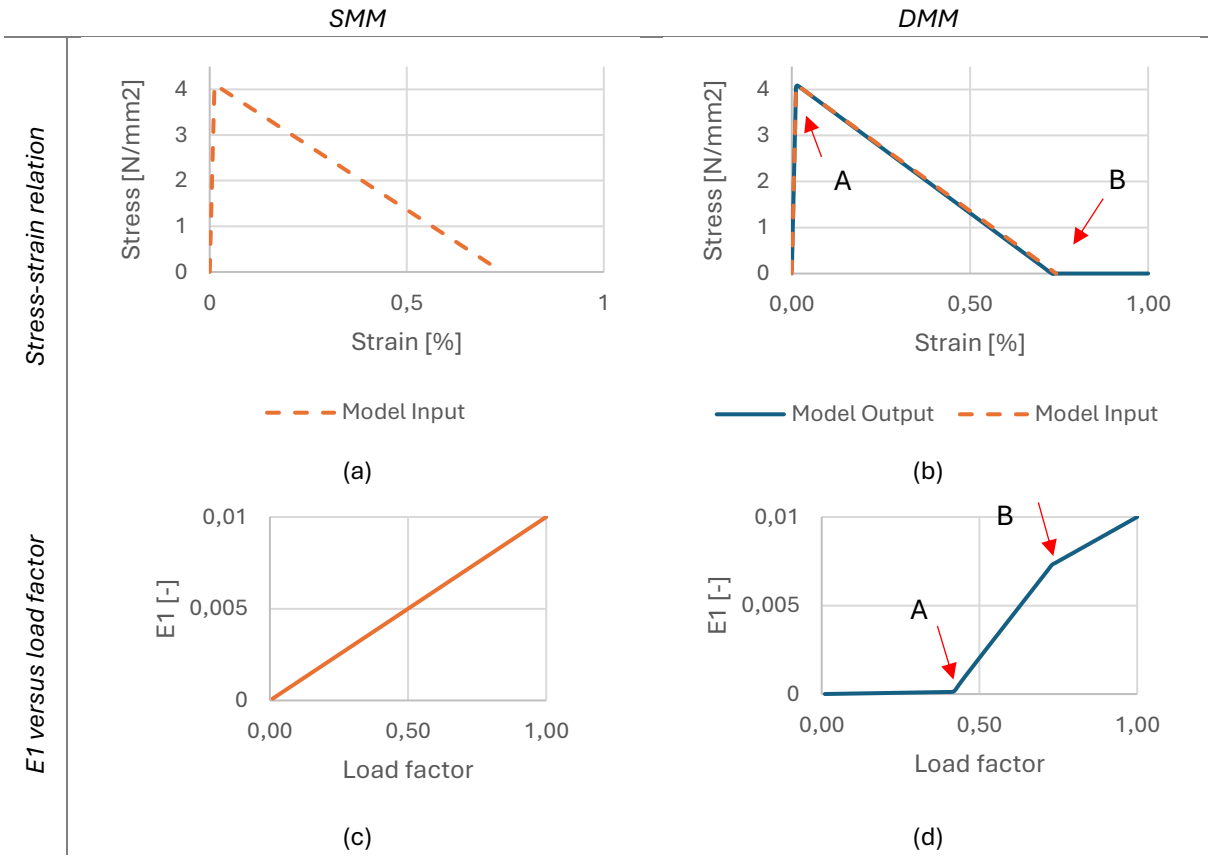

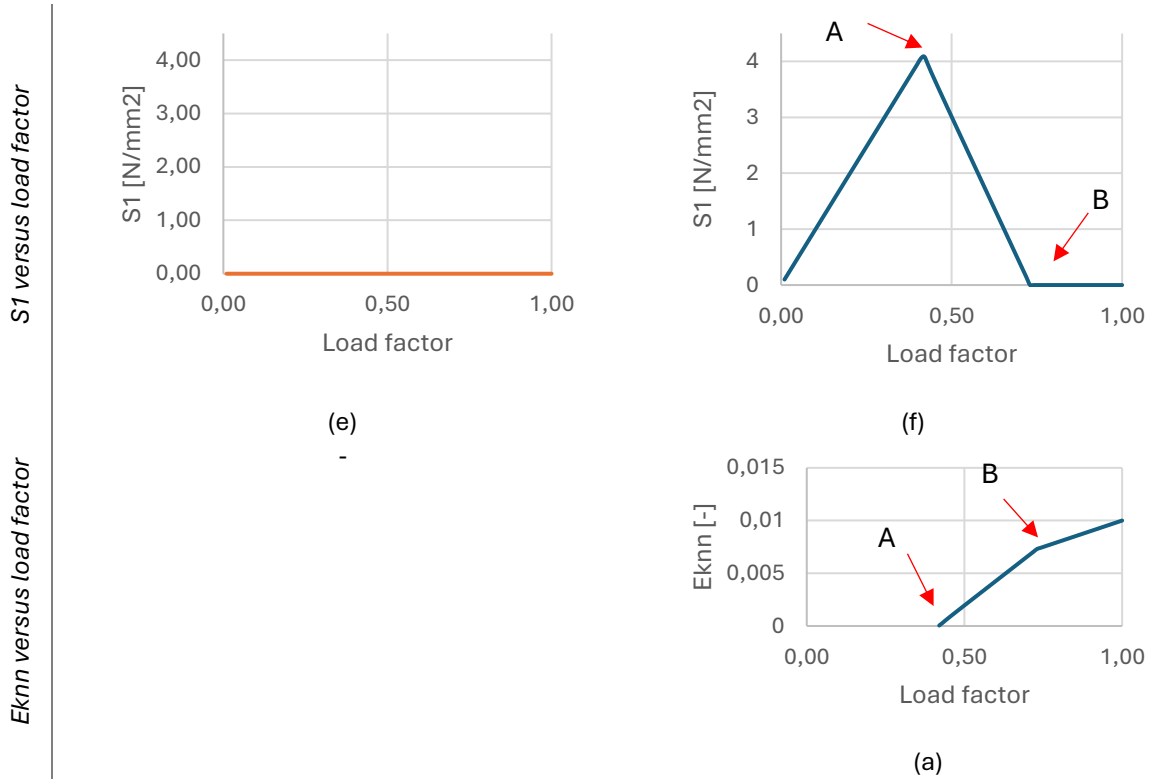

Figure 20 Comparison of Stress-Strain Input and Output, Principal Strains, Principal Stresses, and Cracking Strain Versus Load Factor for Single Mesh Method (SMM) and Dual Mesh Method (DMM); (A: maximum tensile strength, and B: ultimate strain).

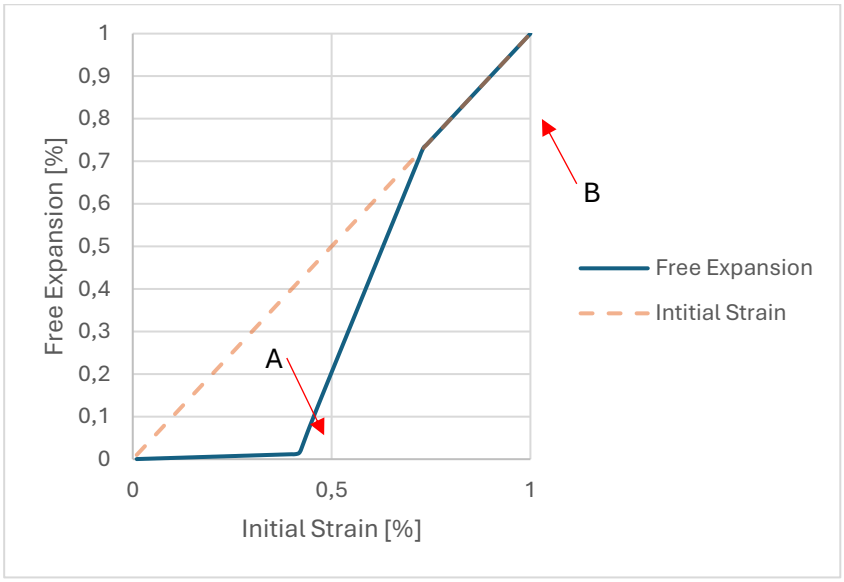

Figure 21 development of Free Expansion on the Structural Mesh with Respect to Initial Strain in Nonlinear Analysis for Dual Mesh Method (DMM), Showing Three Distinct Expansion Stages; (A: maximum tensile strength, and B: ultimate strain).

Finally, when initial strain is applied to the shadow mesh, it induces expansion on the structural mesh, which is considered as the free expansion. The initial strain applied to the shadow mesh and the resulting free expansion on the structural mesh differ from each other, as shown Figure 21. This difference highlights the need for calibration steps to determine the corresponding free expansion for each applied initial strain step, before applying it to confinement conditions.

4.2.2.3 Investigation of Expansion Anisotropy

In this section, a comparison was made between a 2D concrete cube model with expansion applied to the shadow mesh under three conditions: unrestrained, restrained with a single steel rebar in the x-direction. Figure 22 shows contour plots of displacement in the x-direction for all three cases at 1% initial strain. Figure 23 presents contour plots of displacement in the y-direction for the same cases and stages. Figure 24 illustrates crack strain vectors with crack directions at the onset of cracking and at 1% initial strain for both.

In the **unrestrained case**, cracks occur simultaneously throughout the structural mesh with a random pattern, and displacements are uniform in both x and y directions, indicating isotropic expansion due to ASR.

In the **restrained case,** the displacement in the x-direction is reduced near the rebar area due to the restraint imposed by the steel reinforcement. Slight increases in displacement are observed at the corners of the cube in the x-direction, suggesting a redistribution of expansion stresses, while displacement in the y-direction is minimally affected. Crack patterns become less random in the restrained direction, with cracks around the rebar aligning parallel to the restrained direction, consistent with observations from the literature. This behaviour reflects how restraint affects crack development and orientation in ASR-induced expansion scenarios.

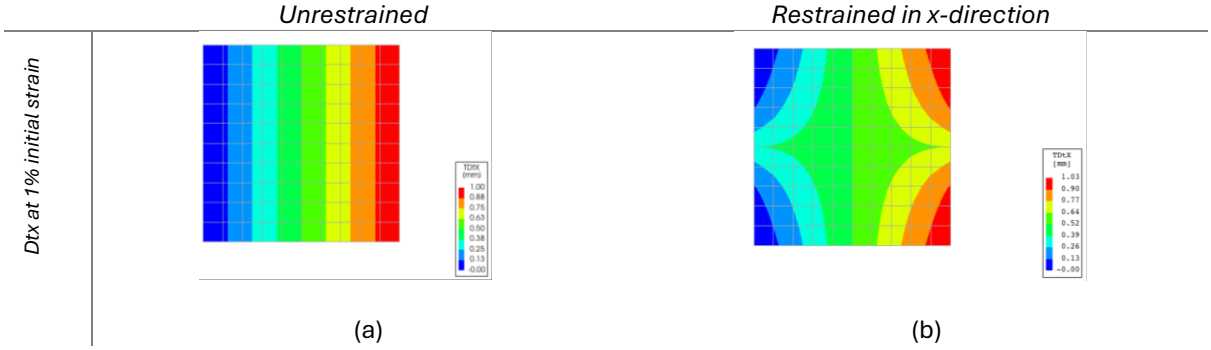

Figure 22 Contour plots of displacement in the x-direction for unrestrained, restrained, and restrained with Poisson's ratio = 0 cases at the onset of cracking and at 1% initial strain.

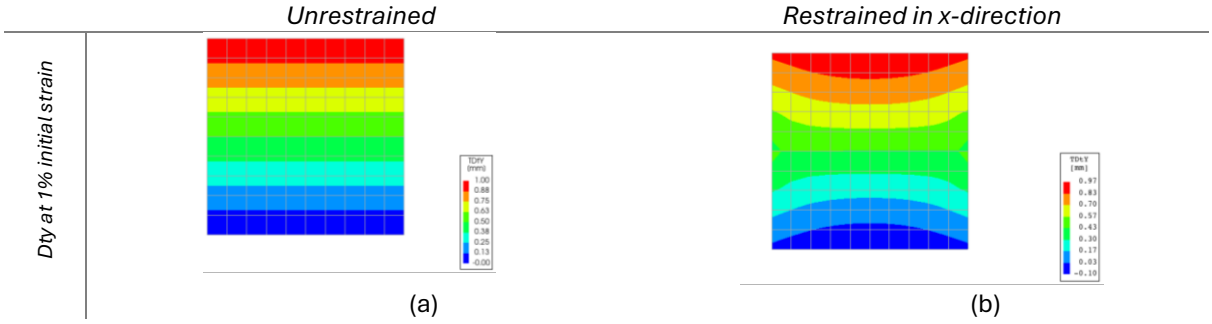

Figure 23 Contour plots of displacement in the y-direction for unrestrained, restrained, and restrained with Poisson's ratio = 0 cases at the onset of cracking and at 1% initial strain.

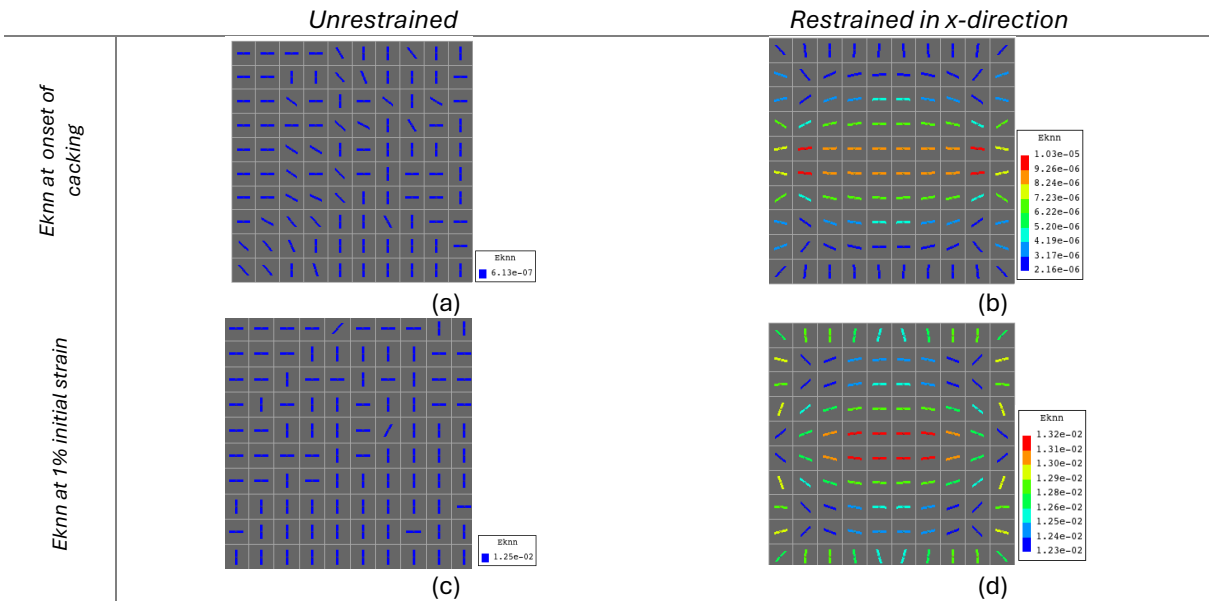

Figure 24 Crack strain orientation at the onset of cracking and at 1% initial strain for unrestrained, restrained, and restrained with Poisson's ratio = 0 cases.

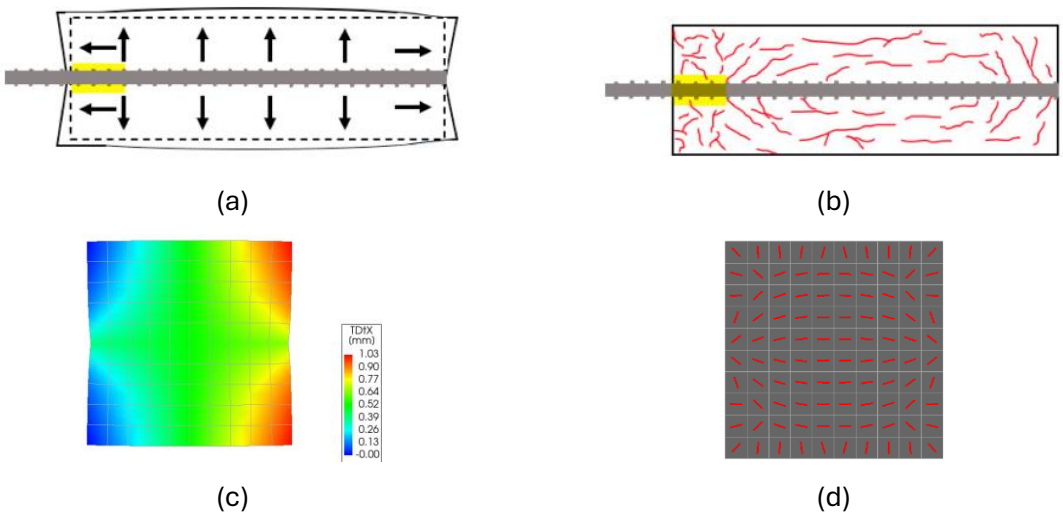

Figure 25 Comparison of Conceptual Crack Propagation Diagrams of ASR-affected prisms with one rebar from from Farooq et al. [70] with Numerical Simulation Results for ASR-Affected Cube with Single Rebar; (a) deformed prism [70]; (b) crack pattern of the prism [70]; (c) model output of deformation in x-direction: (d) model output of crack orientation.

Figure 25 compares the conceptual diagrams of crack propagation in prisms with one rebar from Farooq et al. [70] to the deformation and crack orientation observed in the numerical simulation of the ASR-affected cube with a single rebar. The numerical results exhibit similar deformation behaviour to the diagrams in Figure 25(a), with free expansion-like effects at the edges (top and bottom) due to reduced restraint from the rebar. The crack patterns in the cube also show alignment with Figure 25(b), where diagonal cracks are observed at the top and bottom regions and vertical cracks dominate the middle region. While the numerical model does not replicate physical reality, the resemblance suggests that the developed model captures key features of expansion anisotropy influenced by reinforcement, providing valuable insights into potential crack propagation trends under ASR effects.

4.2.2.4 Investigation of Material Property Degradation

Figure 26 compares the model output for tensile strength (ft) and elastic modulus (E) reduction as functions of ASR-induced expansion using the linear tensile curve model, alongside the ISE lower bound [17] for reference. It should be noted that the model's output for E-modulus represents the secant elastic modulus, defined as the tangent of the line connecting the targeted point to the origin.

For tensile strength, Figure 26(a) shows that the linear model predicts a proportional decrease in ft with increasing expansion, aligning closely with the ISE lower bound but ultimately reducing to zero.

While this provides a useful baseline for understanding material degradation, it is important to view this from a different perspective. In the present approach, ASR expansion is applied incrementally to represent progressive changes over time. Observations from the literature [12, 17, 27] indicate that tensile strength decreases with increasing expansion but eventually stabilises at a residual plateau. This finding implies that ASR-affected concrete retains some residual tensile strength over time, a behaviour that should be incorporated into the model to enhance its accuracy.

For elastic modulus, Figure 26(b) shows a rapid decline in stiffness in the linear model, with a sharp drop below 0.2 even at minimal expansion levels, stabilising after 0.1% expansion. By contrast, the ISE lower bound suggests a more gradual and conservative reduction in stiffness. This difference highlights that the current tensile curve predicts rapid deterioration, particularly during the early stages of ASR-induced expansion. To address this, the tensile strength–expansion relationship within the model requires adaptation to align with realistic behaviour observed in ASR-affected structures.

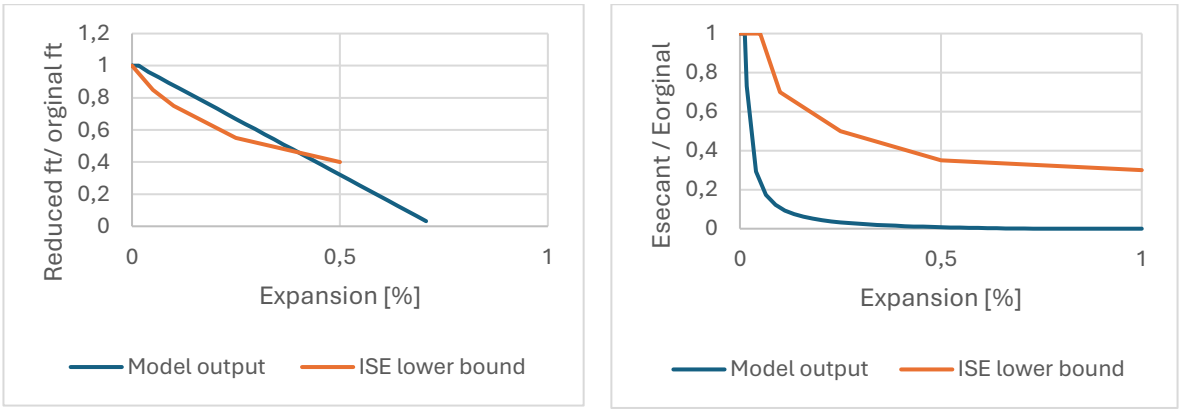

(a) (b)

Figure 26 Comparison of Model Output and ISE Lower Bound for Tensile Strength and Elastic Modulus Reduction Due to Expansion Using Linear Tensile curve

While these results demonstrate the model's capability to capture material degradation, the critical question remains whether these reductions faithfully represent observations from case studies or specific material degradation-expansion relationships. The next section will address this issue by refining the model to enhance its applicability to real-world ASR-affected structures.

4.3 Adapted Tensile Curve (ATC)

In finite element analysis (FEA), constitutive models are used to simulate the stress-strain behaviour of materials, including concrete, under various loading conditions. For ASR-affected concrete, the choice of a constitutive model must reflect the specific objectives of the analysis. In this study, the goal is to predict the structural behaviour of concrete subjected to ASR over time by incorporating strain increments as inputs to represent varying expansion levels. A realistic representation of the progressive degradation of material properties, including tensile strength and elastic modulus, is critical for achieving this goal.

To illustrate the concept, Figure 27 presents a schematic view of the tensile curve evolution under ASR-induced expansion. At t_0, with no ASR effects, the tensile curve corresponds to an unaffected concrete with initial tensile strength (f_t) and elastic modulus (E). Over time, as ASR-induced expansion progresses to t_1, represented by ε_1, both f_t and E begin to degrade. At t_2, with a further expansion ε_2, the reduction of these properties intensifies. If the focus is placed solely on the degradation of f_t and E with respect to ASR expansion, a clear relationship emerges: tensile strength and elastic modulus decline progressively with increasing strain, stabilising at a residual value. Capturing this behaviour in the model requires a tensile curve adapted to represent this progressive degradation.

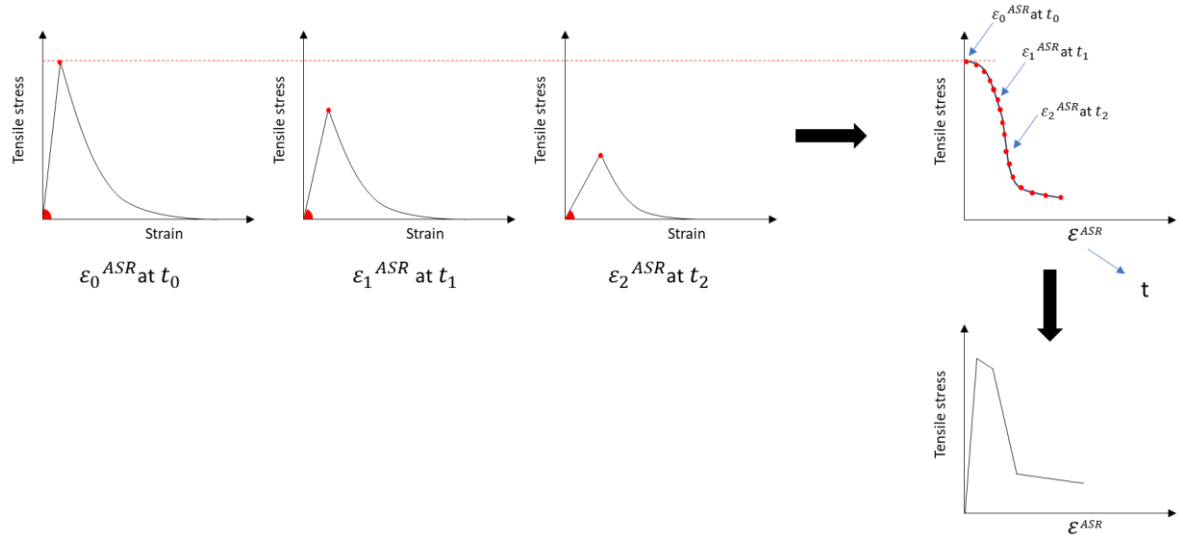

Figure 27 Conceptual Illustration of Tensile Curve Evolution under ASR-Induced Expansion.

This section focuses on adapting the constitutive model for ASR-affected concrete to capture the relationship between material degradation and expansion progression. Esposito et.al [27] provides a valuable framework for this adaptation, identifying that tensile strength and elastic modulus degradation due to ASR follows an inverse sigmoid function. In this behaviour, both properties decrease with increasing ASR-induced expansion but stabilise at a residual value, as shown in Figure 28. This finding is significant because it suggests that ASR-affected concrete retains some residual tensile strength, which must be accounted for to achieve accurate structural predictions. Esposito et. al [27] also emphasises the importance of elastic modulus as a key indicator of ASR damage, which can be used to recalibrate tensile strength models for improved alignment with observed material behaviour.

4.3.1 Methodological Approach for ATC

To adapt the tensile softening behaviour of ASR-affected concrete, this study employs Esposito's normalised degradation model, using tensile strength and elastic modulus as key indicators.

Standard parameters from the literature and experimental data, as summarised in Table 3, are used to develop and validate the model concept. While these parameters are illustrative at this stage, and they don't represent real value, they will be refined and calibrated based on specific case study results in Chapter 6.

- **Recalibrating Based on Tensile Strength**: Up to elastic strain limit, tensile strength increases until reaching its maximum. Thereafter, the tensile strength decreases until it reaches a residual strength. This is modelled by multiplying the normalized βP value for tensile strength by the maximum tensile strength, shown in Figure 29.
- **Recalibrating Based on Elastic Modulus**: Similarly, the elastic modulus initially governs tensile behaviour until peak strain. Afterward, the modulus decreases along with the tensile strength. This recalculation is done by multiplying the normalized βP value of the elastic modulus by the expansion, as shown in Figure 29.

Table 3 Original tensile strength and E-modulus values of model next to standard parameters of Esposito's model based on Literature Data [27].

	Original value	β0	β∞	ϵc	ϵl
Tensile strength ft	3.13 MPa	1.01	0.6	0.11	0.35
Elastic modulus E	34300 MPa	1.06	0.19	0.37	1.13E-09

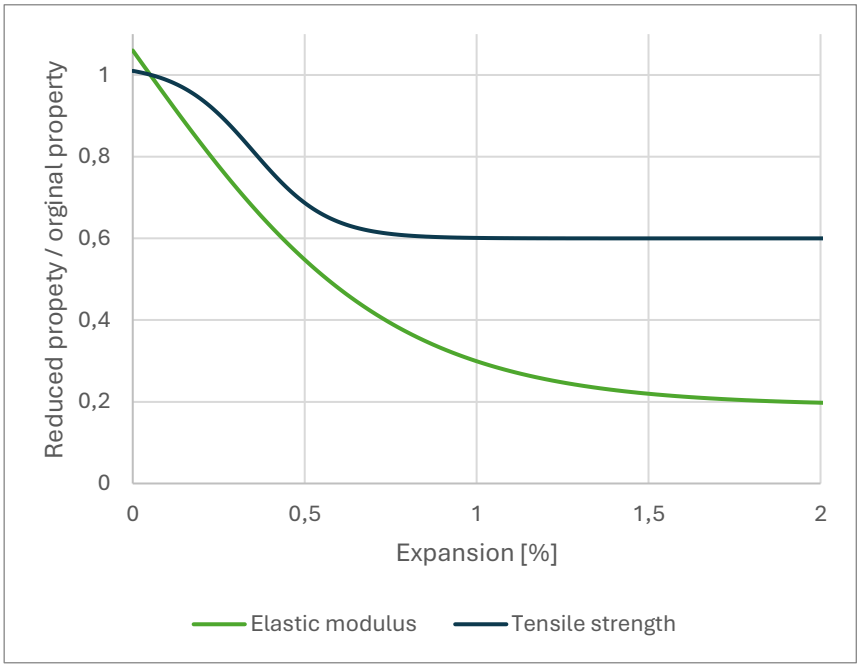

Figure 28 Reduction of mechanical properties adapted from (Esposito et al., [27])

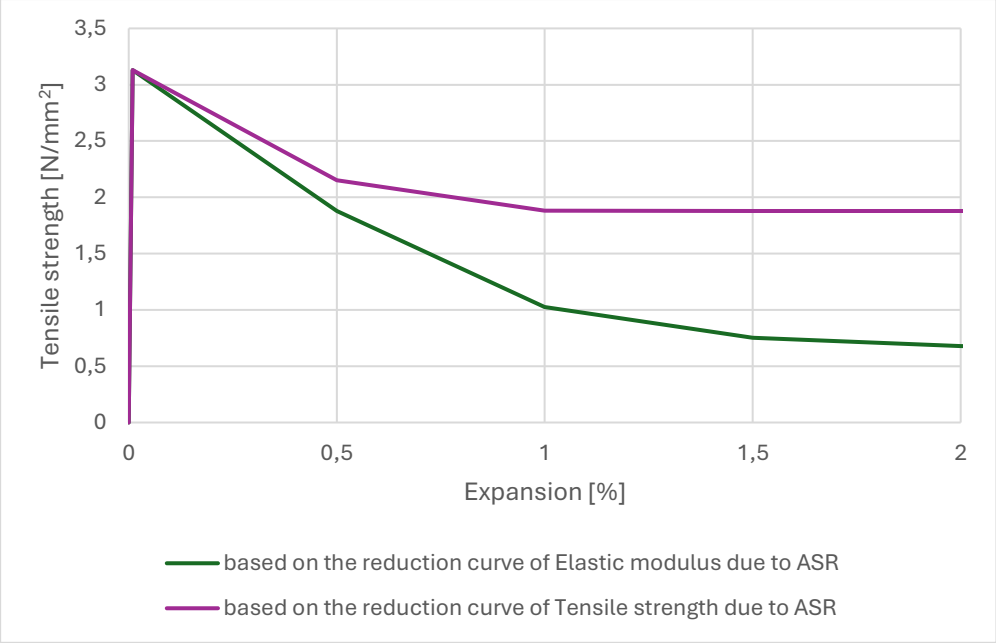

Figure 29 tensile strength-expansion relation recalculated from Esposito's model in compassion with the linear relation of normal concrete

4.3.2 Results & Discussion

The relationship between tensile behaviour and ASR-induced expansion is integrated into the numerical model using a multi-linear stress-strain relationship. The 2D concrete cube model described in the previous sections is employed to evaluate the model's ability to replicate the targeted reduction in material properties. Figure 30 illustrates the input for the tensile behaviour using a multi-linear approach.

A strain of 1% is incrementally applied to simulate ASR-induced expansion, and the resulting degradation of tensile strength and elastic modulus is assessed based on the observed stress-strain behaviour of the model. Additionally, a verification test is performed to cross-check the model's predictions: at a specific expansion level, a strain increment is applied, followed by a compressive load, to evaluate the material's response under realistic conditions. This test ensures the model's validity in capturing material degradation due to ASR.

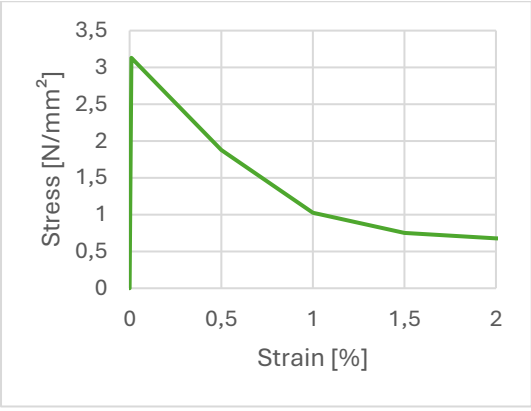

Figure 30 Model input for tensile curve using Multi-linear model

4.3.2.1 Investigation of the Multi-linear model

Figure 31 compares the model output with Esposito's literature-based model for tensile strength (a) and elastic modulus (b) reductions due to expansion. In Figure 31(a), the model predicts a residual tensile strength at higher expansion levels, but the reduction values are lower than those

of the reference. This difference arises because the model output is recalibrated based on elastic modulus reduction rather than directly on tensile strength. Figure 31(b) shows a rapid decrease in elastic modulus, similar to the behaviour observed in the linear model, indicating that the proposed adapted model does not fully capture the gradual reduction of the elastic modulus.

Figure 32 further investigates the reduction behaviour of elastic modulus (E modulus) using different tensile softening curves. The calculated secant E modulus for all three curves demonstrates a similar trend: a rapid decline in stiffness at small expansion levels, stabilising at a significantly reduced value beyond a certain point. This pattern suggests that the majority of stiffness degradation occurs in the early stages of ASR expansion, with minimal changes thereafter.

This behaviour highlights a limitation of the current model, as it does not simulate the gradual and progressive reduction of elastic modulus observed in real ASR-affected concrete. This limitation should be considered when applying the model to predict the structural behaviour of ASR-affected structures. Furthermore, it is concluded that basing material property degradation on tensile strength, rather than elastic modulus, may provide a more accurate representation of the observed behaviour.

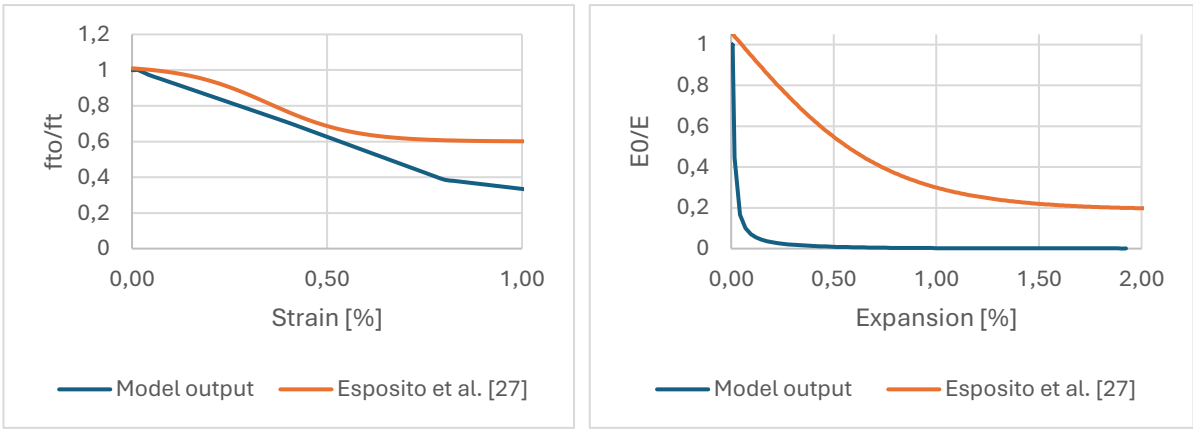

(a) (b)

Figure 31 Comparison of Model Output and Literature Esposito's model for Tensile Strength and Elastic Modulus Reduction Due to Expansion Multi-Linear Model

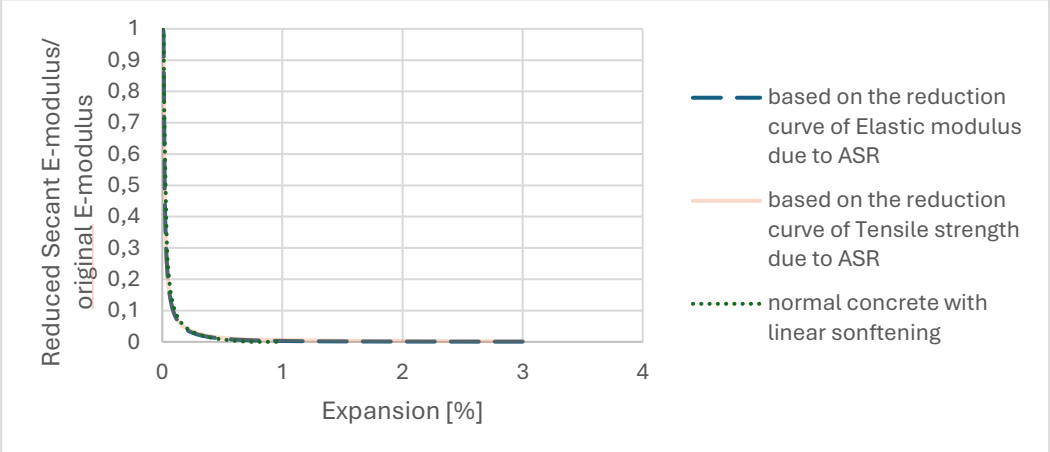

Figure 32 Comparison of Model Output for Elastic Modulus Reduction Using Different Softening Curves under expansion.

4.3.2.2 Validation of Degraded Material Properties at Specific Expansion Levels

In this subsection, a load test was conducted to validate the material degradation results derived from the model's stress-strain state. This test aims to verify whether the model accurately predicts the degradation of material properties as a result of ASR-induced expansion. The process involved applying an expansion to a 2D cube model up to a certain level, followed by the application of compressive loading. A load-displacement curve was then plotted. This procedure was repeated for several different expansion levels.

The resulting load-displacement curves display two distinct phases. In the initial phase, where cracks are still open due to the expansion-induced damage, the curve exhibits lower stiffness (sloop of the red line). As the compressive load increases, the cracks progressively close, marking the beginning of the second phase. In this second phase, the stiffness of the concrete corresponds to its compressive strength (sloop of the green line). Figure 33 presents the load-displacement curve after an induced expansion of 0.03%.

This process was repeated for several expansion levels. At each step, the actual elastic modulus (E) values were plotted against the reduced modulus values obtained from the stress-strain state. Figure 34 demonstrates a good match between both values, validating the model's ability to simulate material degradation due to imposed expansion.

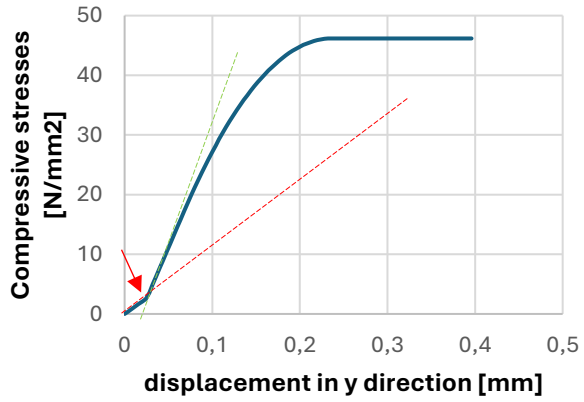

Figure 33 Load-displacement curve as result of applying compressive load test to 2D concrete cube model after 0.03% imposed expansion.

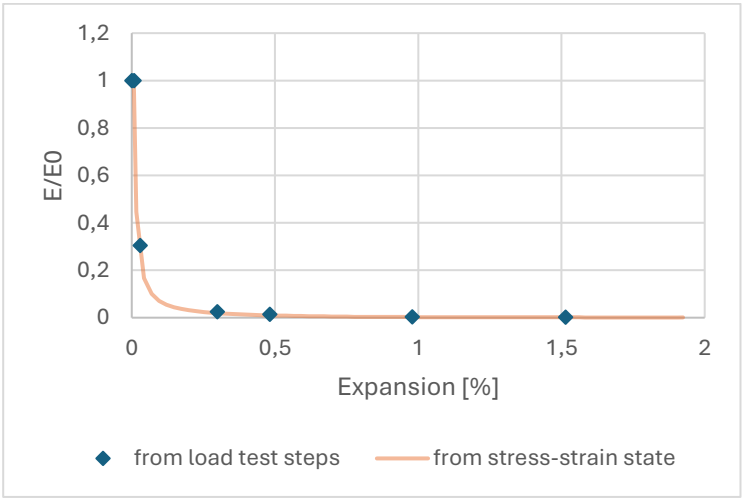

Figure 34 Comparison between actual elastic modulus values from load tests and calculated reduced elastic modulus values from the stress-strain state across multiple expansion levels.

4.4 Phased Analysis

In the DMM, the structural mesh and shadow mesh share the same nodes, resulting in the shadow mesh's stiffness also contributing to the total structural stiffness. In DIANA software, phased analysis enables the activation and deactivation of groups (sets) of elements between phases [75]. Within the dual mesh concept, phased analysis is employed to manage the transition from the original structural design to the ASR-affected state.

In the first phase, the model represents the original design under initial loading conditions, with the shadow mesh deactivated to prevent its stiffness from contributing to the total structural stiffness. In the second phase, the shadow mesh is activated to simulate ASR-induced expansion, applied incrementally to represent the progressive deterioration of the structure.

4.4.1 Simple Beam Model

To demonstrate the effects of phased analysis, a simple 2D concrete beam model was created. The beam, 1000 mm in length and 100 mm in width, includes a single Ø10 mm rebar embedded with perfect bonding (see Figure 35). The finite element details and material properties for the concrete and shadow meshes are similar to those used in the 2D cube models discussed in Section 4.2.1.

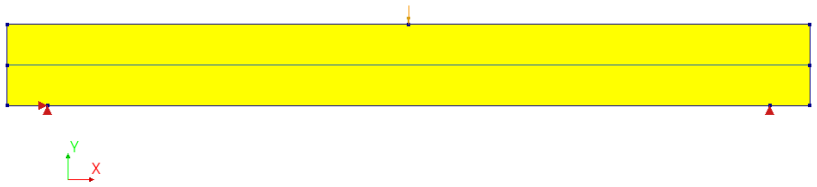

Figure 35 FEM model of simple beam with single rebar

4.4.2 Results and Discussion

Figure 36 compares the principal stress contour plots for three cases. SMM, where no shadow mesh is used, DMM with the shadow mesh active in all phases, and DMM using phased analysis, where the shadow mesh is deactivated during self-weight and point load applications activated during ASR expansion.

The results show identical stress distributions for the SMM and DMM with the shadow mesh deactivated during loading, confirming that the shadow mesh does not contribute to structural stiffness in these cases. When the shadow mesh is always active, a slight reduction in concrete stresses is observed, demonstrating its contribution to the total stiffness. These findings validate the phased analysis approach, ensuring precise control over the activation and deactivation of the shadow mesh and its influence on the structural response.

It should be noted that after expansion is applied, the first crack forms at the middle of the beam's bottom, as shown in Figure 37. This crack is driven by stress concentrations from the applied loads. In contrast to the cube model, where cracks develop uniformly under pure expansion, the beam model demonstrates crack initiation influenced by loading conditions, highlighting the role of stress concentration in directing damage progression in this model.

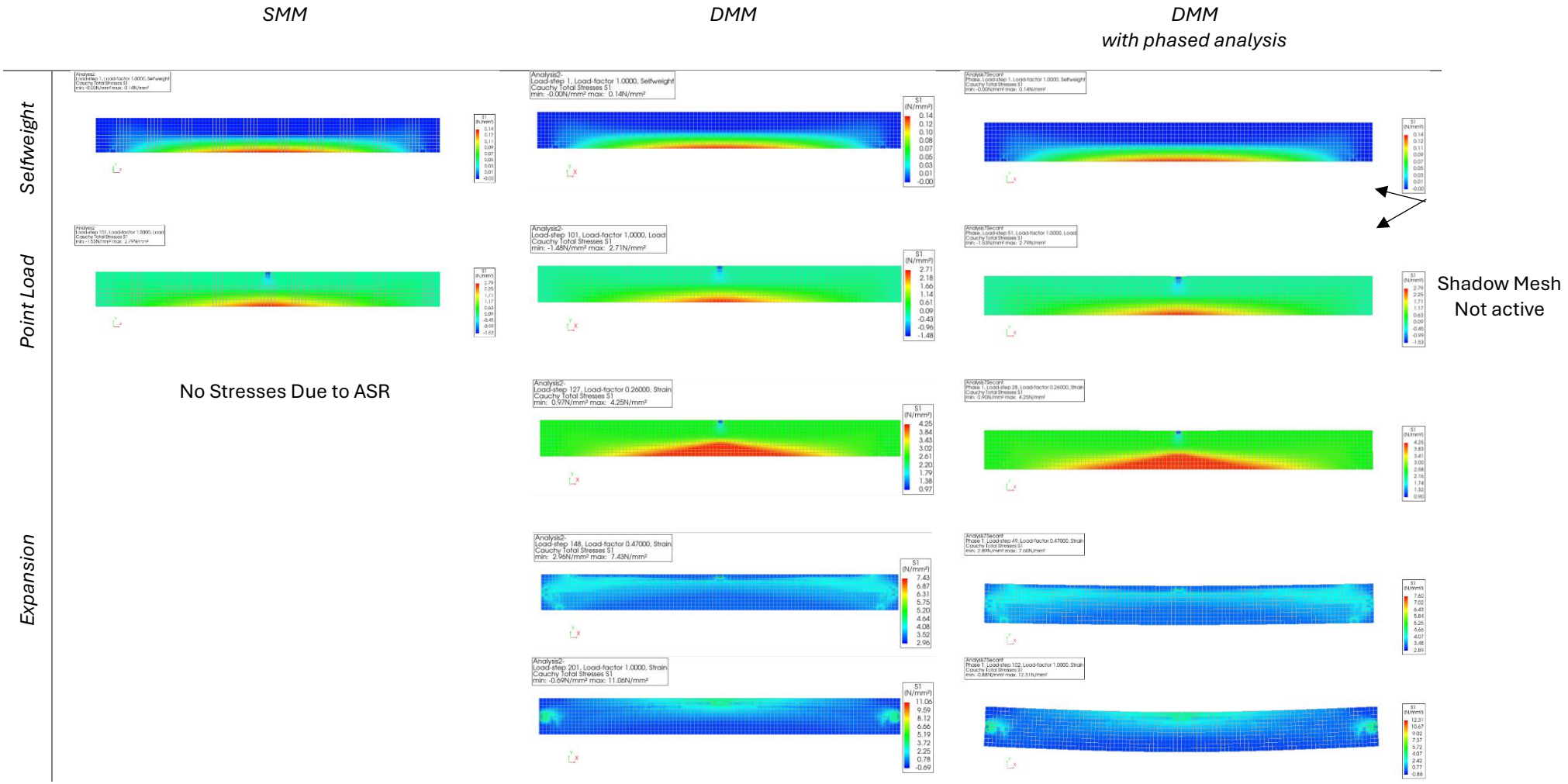

Figure 36 Comparison of Principal Stress Contour for SMM, DMM Active, and DMM Phased Analysis.

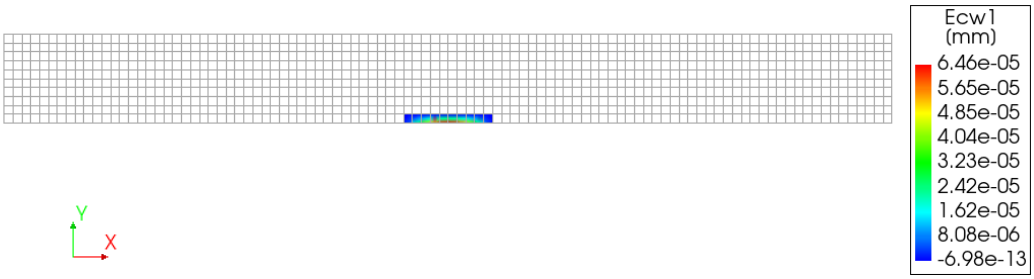

Figure 37 First Crack Initiation Due to Combined Loading and Expansion

4.5 Conclusion

This chapter developed a numerical modelling approach to simulate the long-term structural behaviour of reinforced concrete structures affected by Alkali-Silica Reaction (ASR). Building upon the Dual Mesh Method (DMM), the method was adapted and refined to address specific challenges associated with ASR-induced damage.

The key findings are as follows:

The DMM was effectively implemented to simulate ASR-induced expansion by applying strain through a shadow mesh. Linear analysis confirmed that the model's displacement results align with the analytical solution proposed by Chen, validating the method's implementation. Nonlinear analysis demonstrated the model's capability to simulate stress development and crack propagation due to ASR-induced expansion. The nonlinear analysis revealed that induced cracks reduce the stiffness of the structural mesh, making the interaction between the structural and shadow meshes dynamic. This interaction accurately represents the progressive damage in ASR-affected concrete. Further, the model successfully simulated anisotropic expansion when directional restraint was introduced through reinforcement. The crack patterns and deformation behaviours observed in the simulations corresponded with conceptual diagrams from the literature, indicating that the model can capture the influence of structural configuration on expansion anisotropy.

The model was able to represent the reduction in tensile strength due to ASR-induced expansion. However, it showed a rapid decline in elastic modulus at early stages of expansion, which does not fully align with more gradual degradation observed in real ASR-affected concrete. This indicates a limitation in the model's ability to simulate elastic modulus reduction accurately over the entire expansion range. By integrating an adapted tensile curve based on literature models, the tensile strength degradation was more realistically represented in the model. The ATC accounted for the residual tensile strength observed in ASR-affected concrete. Nonetheless, the model still exhibited limitations in capturing the gradual reduction of elastic modulus, suggesting that basing material degradation on tensile strength may provide more accurate results.

Phased analysis was utilised to apply realistic loading conditions and manage the activation of the shadow mesh. This approach ensured that the shadow mesh's stiffness did not contribute to the overall structural stiffness during initial loading phases, allowing for accurate simulation of ASR effects introduced in subsequent phases. The simulations showed that, under combined loading and ASR-induced expansion, cracks initiated at locations of stress concentration due to applied loads. This contrasts with models under pure expansion, where cracks developed uniformly. This finding highlights the model's ability to represent the interaction between mechanical loading and ASR-induced damage.

The modifications and enhancements to the Dual Mesh Method, including the implementation of an adapted tensile curve and the use of phased analysis, have improved the model's capability to simulate ASR-induced damage in reinforced concrete structures. The adapted model can capture key aspects of ASR effects, such as stress generation mechanisms, anisotropic expansion, and material property degradation. However, the limitations identified—particularly in accurately representing the gradual reduction of elastic modulus—suggest the limitation of the developed model. Overall, the developed modelling approach provides a valuable tool for simulating the long-term structural behaviour of ASR-affected concrete structures. It lays the groundwork for more comprehensive analyses in subsequent chapters, where the model can be calibrated and validated against specific case studies.

5. Model Assessment

This chapter evaluates the Modified Dual Mesh Method (MDMM) and the underlying assumptions by applying it to a benchmark structure commonly used for validating finite element models (FEM). As illustrated in Figure 38, the assessment begins with a comparison between an unaffected beam using two constitutive models: the linear softening behaviour and the multi-linear model proposed in the previous chapter (Section 5.3). Subsequently, the MDMM's capability to simulate Alkali-Silica Reaction (ASR) damage on ASR-affected beams is examined through three distinct static load cases: a beam with marginal expansion, a beam with very high expansion, and a beam with marginal expansion combined with additional uniform prestressing (Section 5.4). Additionally, the chapter explores the MDMM's performance in simulating ASR effects under gradual expansion conditions, demonstrating the potential to link these gradual expansion levels with time using Larive's model (Section 5.5). A comparative approach is employed throughout the analysis to ensure consistency and validate the model's accuracy in predicting ASR-induced structural behaviour.

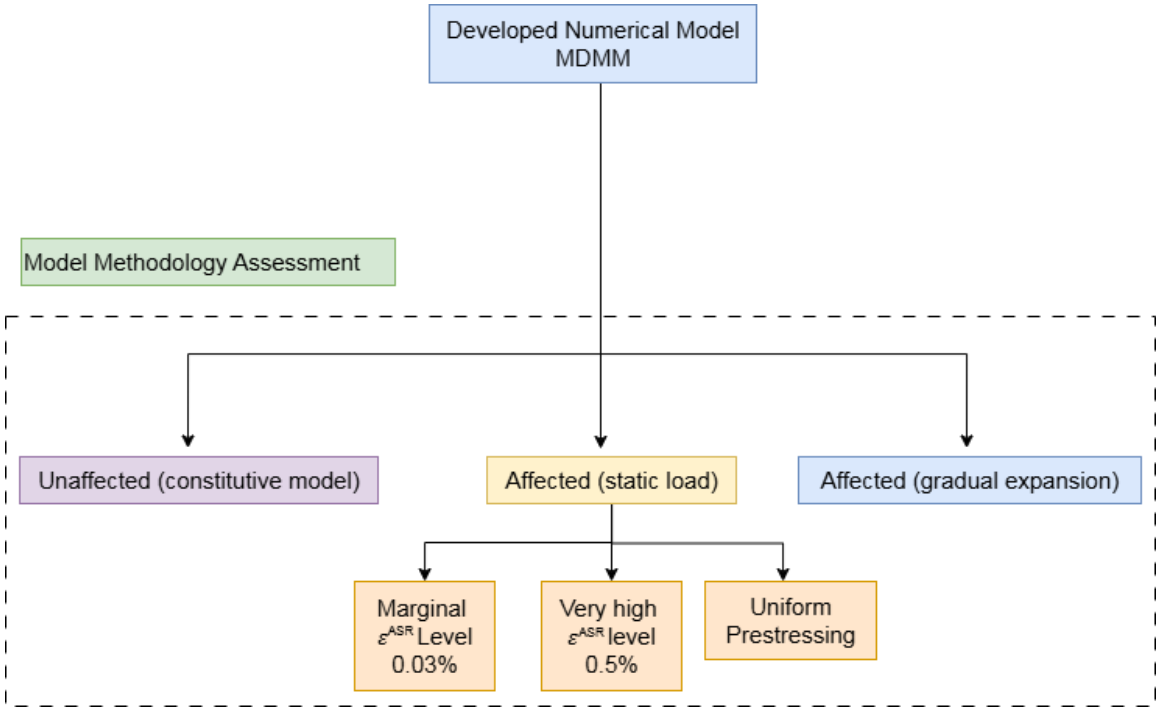

Figure 38 Workflow of model assessment

5.1 Benchmark Description: Toronto Beam Test VS-C3

The Toronto Beam Test VS-C3 from Vecchio et al. (2004) [71] serves as the benchmark for validating the developed MDMM. This experimental study involves a reinforced concrete (RC) beam subjected to increasing static loads until failure. The beam dimensions are as follows: a total length of 6.840 m, a depth of 0.552 m, and a width of 0.152 m. Detailed geometry, reinforcement, loading conditions, boundary conditions, and the experimental setup are illustrated in Figure 39.

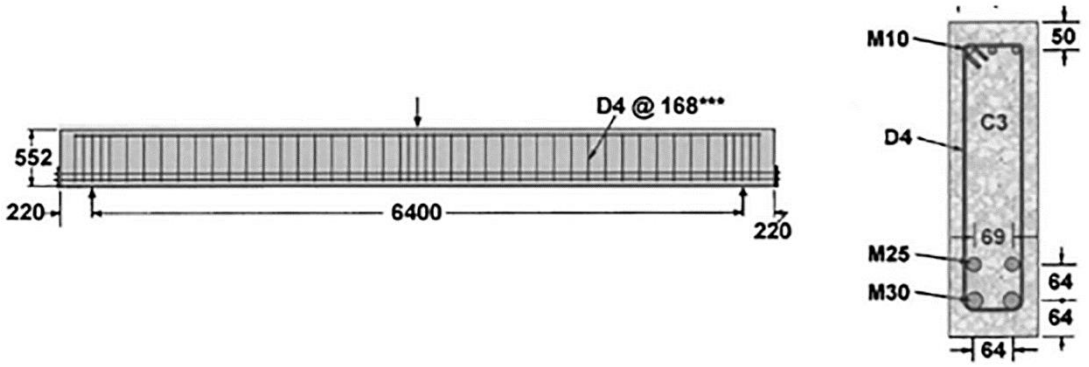

Figure 39 Characteristics of the Toronto beam test VS-C3 [71].

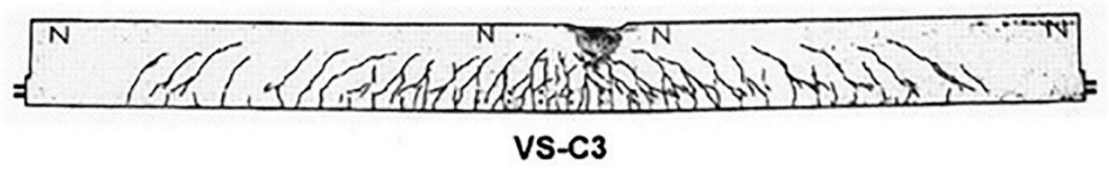

Figure 40 Toronto beam test VS-C3 at ultimate load [71].

Table 4 Cross section and elevation details [71].

Beam number	b (mm)	h (mm)	L (mm)	Span (mm)	Bottom steel	Top steel	Stirrups
C3	152	552	6840	6400	4 No. 9	2 No. 4	No. 2 at 210

The beam exhibited a flexural-compressive failure mode, as shown in Figure 40. The measured peak load was P_{exp} = 265 kN at a deflection of 44.3 mm. Most material properties are available from the original publication [71]. For parameters not specified, values were estimated according to the Model Code 2010 [72]. The material properties used in the numerical model are summarized in Table 4, Table 5 and Table 6

Table 5 Concrete Properties (C3 Beam)

Beam Number	**Cylinder Compressive Strength (MPa)**	**Splitting Tensile Strength (MPa)**	**Tensile Fracture Energy (N/mm)**	**Young's Modulus (GPa)**
C3	43.5	3.13	0.144*	34.3

**Calculated based on Mode code 2010* [72].

Table 6 Reinforcement Properties

Bar Size	**Diameter (mm)**	**Area (mm^2)**	**Yield Stress (MPa)**	**Ultimate Strength (MPa)**	**Young's Modulus (GPa)**
M10	11.3	100	315	460	200
M25	25.2	500	440	615	210
M30	29.9	700	436	700	200
D4	3.7	25.7	600	651	200

Experimental data, including the load-displacement curve and crack patterns at failure, are available for comparison with the numerical results. However, this data is utilized only for the unaffected beam case to verify the correct setup of the model and to assess the magnitude of the effects resulting from changes in the concrete constitutive model. For the other cases, the load-displacement curves and crack patterns from the numerical model of the unaffected beam itself are used as references. This approach ensures that the model is accurately calibrated before evaluating its performance under various ASR-induced damage scenarios.

5.2 Finite Element Model Description

The finite element model of the Toronto beam test VS-C3 is presented in Figure 41. This model includes the beam geometry with longitudinal reinforcements (3x M10, 2x M25, and 2x M30 bars), transverse reinforcements (D4), loading plate, support plates, and the shadow mesh used to simulate ASR-induced expansion.

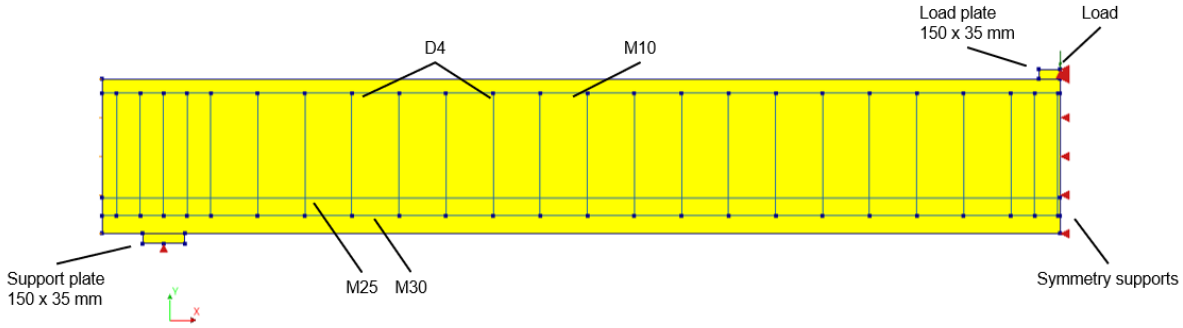

Figure 41 Model of the Toronto beam test VS-C3

Figure 42 gives a simplified details about the model. It should be noted that the model selection was done according to the guidelines of Hendriks and DIANA User's Manuals [73], [74]. Minor adjustments to the finite element model were made to accommodate different case studies, such as variations in material properties or loading conditions. These adjustments are specified in the validation process for each case and are detailed in Appendix E.

For comprehensive information regarding element types, mesh configurations, material properties, and modelling parameters, refer to Appendix E. This appendix provides an in-depth description of the finite element model setup, including tables and figures that support the summarized information presented here.

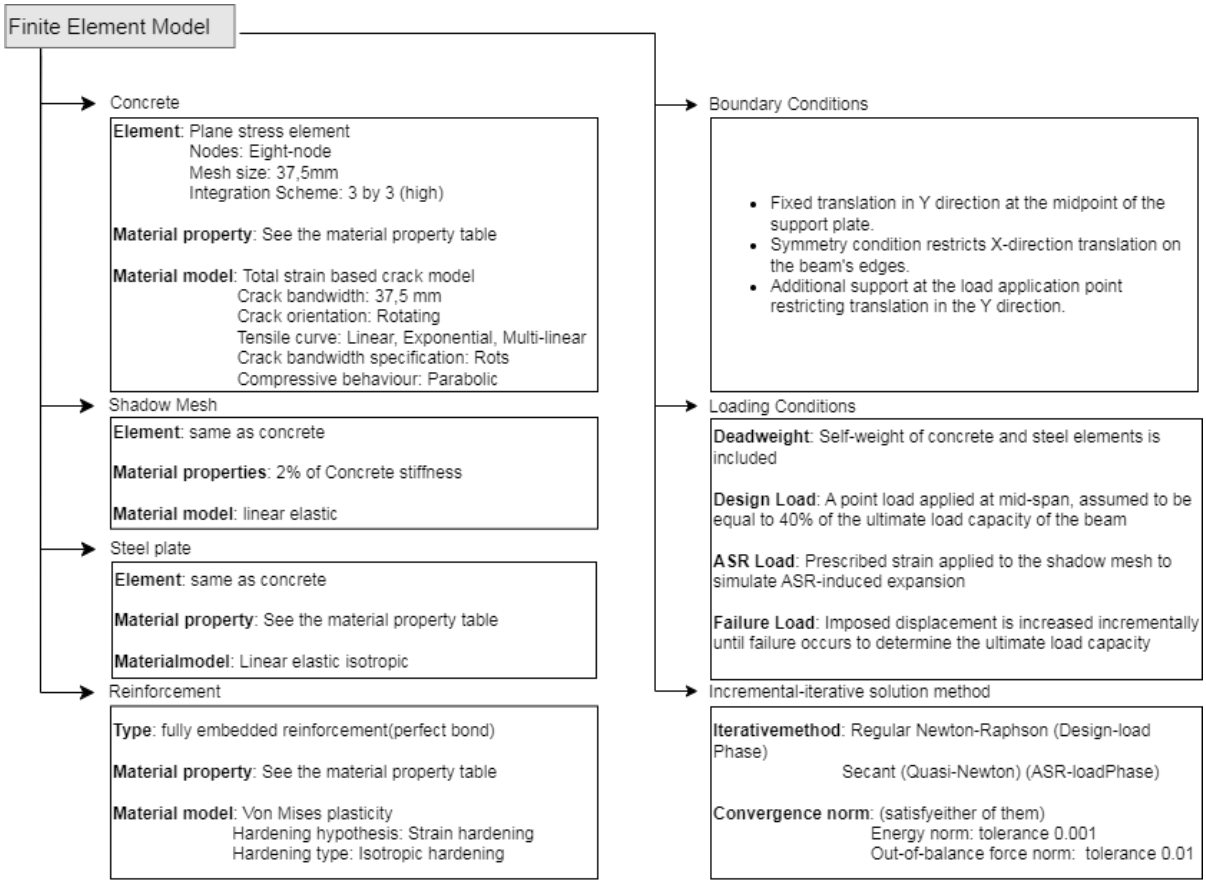

Figure 42 Finite Element Model Description

5.3 Unaffected beam: constitutive models

The initial step in the validation process focused on analysing an unaffected beam to ensure the finite element model was accurately set up and capable of replicating the structural behaviour observed in experiments. This analysis also aimed to evaluate the influence of the proposed Adapted Tensile Curve (ATC) on the model's response. Since the ATC introduces a novel approach to representing tensile strength degradation, this step was crucial to investigate how the model behaves under static loading conditions and to determine whether the ATC produces reasonable results or reveals unexpected behaviour.

Two Tensile curves within the constitutive model were compared:

1. **Multi-linear Model**: Shown in Figure 30, incorporating the adapted tensile curve proposed in Section 4.3 to provide a more accurate representation of tensile strength degradation with progressive loading.
2. **Linear Model**: Shown in Figure 17, used as a reference model for comparison

The beam was subjected to an incrementally increasing prescribed deformation until failure, with the resulting load-displacement behaviour and crack patterns compared against experimental data. This comparison ensured that the model could reliably replicate the structural response of an unaffected beam.

Additionally, a sensitivity study was performed to assess the influence of specific modelling choices on the simulation results. This included replacing the linear model with an exponential tensile model and introducing an interface between the beam and the steel plates. These adjustments aimed to evaluate the potential for improving accuracy and refining the modelling approach.

5.3.1 Results & Discussion

Figure 43 presents the load-displacement curves at the mid-span of the beam for the two numerical analyses using different tensile material models—linear and multilinear—compared with experimental data. Both numerical models align closely with the experimental curve in the elastic range. However, differences emerge near the ultimate load:

- **Linear Material Model**: Underestimates the peak load, reaching a maximum of 235 kN at a displacement of 39 mm, compared to the experimental peak load of 265 kN at 44.3 mm. This corresponds to a relative error of approximately 11.32%.
- **Multilinear Material Model**: Slightly overestimates the peak load, achieving 275 kN at a displacement of 37 mm, with a smaller relative error of 3.77%.

Both models exhibit less deflection at peak load than the experimental data, indicating a stiffer response. The post-peak behaviour shows a more brittle failure compared to the experiment, highlighting limitations in capturing the ductile post-peak response of the material.

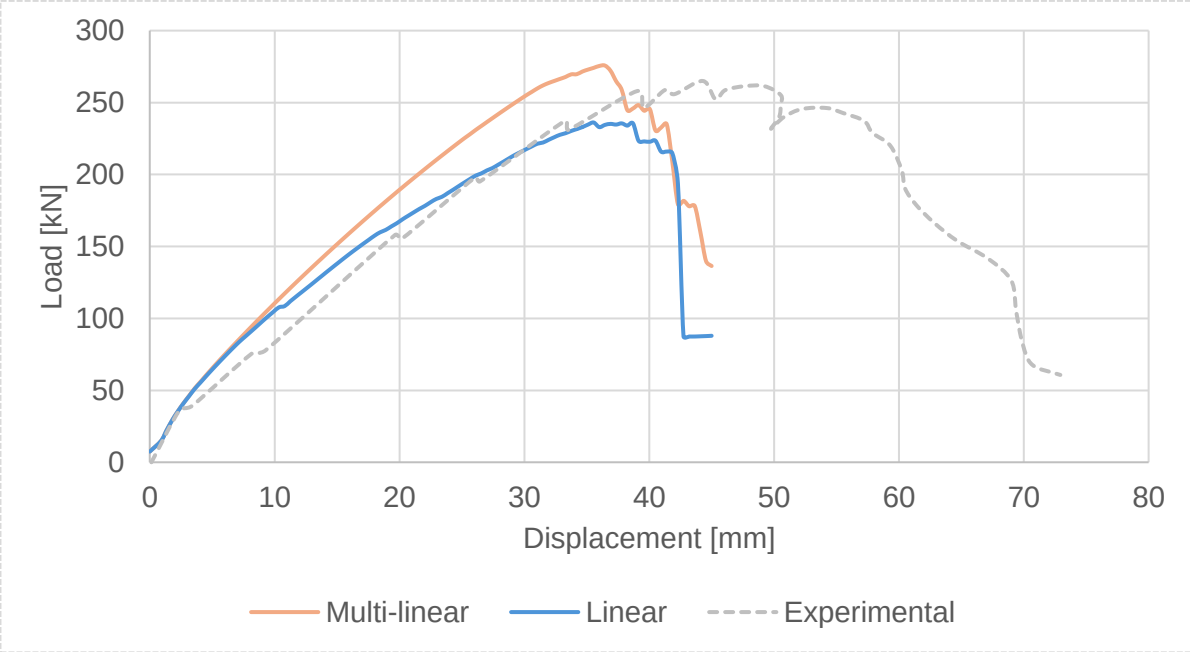

Figure 43 load-displacement curves comparing experimental data with numerical models using linear and multilinear tensile material properties.

Figure 44 (a) presents the experimental crack pattern observed at failure. In contrast, Figure 44 (b) and (c) show the crack widths and patterns at the peak load level for the linear and multilinear material models, respectively. Both numerical models replicate the general crack propagation and distribution seen in the experiment. However, the multilinear model shows smaller crack widths compared to both the linear model and the experimental results.

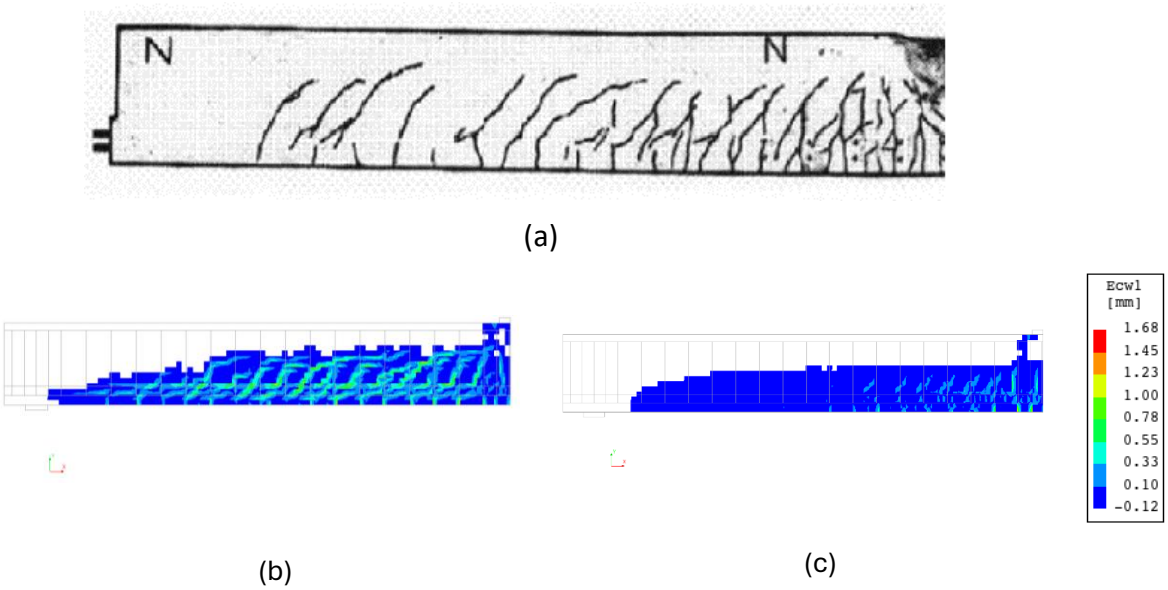

Figure 44 crack pattern comparison at failure load where (a) Experimental crack pattern at failure for beam test VS-C3; ***(b)*** *Principal crack widths and patterns at peak load using the linear material model;* ***(c)*** *Principal crack widths and patterns at peak load using the multilinear material model.*

5.3.2 Sensitivity

In the previous section, the C3 beam from Vecchio et. al was simulated using linear (simplified) and multilinear (more suitable for ASR prediction). While both models showed reasonable agreement with experimental data, deviations were observed at peak load and in the post-peak behaviour. This sensitivity analysis aims to investigate whether modifications in the modelling approach can improve the numerical results. Belletti et al. [75], proposed including interface between the steel plates and the beam and using exponential softening in tension. Therefore, the focus in this sensitive analyse will be on these two aspects, including interface and using exponential softening.

Two cases will be compared in the sensitive study. In the first one, instead of linear material model, the exponential softening will be used with 2D line interface is applied along the right edge boundary of the beam, featuring normal and shear stiffness values of 1×10^{6} N/mm^{2}. In the second one same multilinear model will be used in addition to interface same as previous.

The load-displacement curves for the numerical simulations incorporating an interface and two different tensile material models—exponential softening and multilinear—are presented alongside the experimental data in Figure 45. This figure illustrates three distinct curves: one representing the experimental data, another corresponding to the numerical simulation with the exponential softening material model and interface, and the third corresponding to the simulation with the multilinear material model and interface.

The inclusion of the interface between the steel plates and the beam significantly affects the behaviour of both models. The exponential softening model with the interface shows improved agreement with the experimental data, particularly in the post-peak region, compared to the previous linear and multilinear models without the interface. The curve for the multilinear model with the interface also shows an improvement in capturing the load-displacement behaviour, though its accuracy varies when compared to the exponential softening model.

The experimental data shows a peak load of 265 kN at a displacement of 44.3 mm. The numerical simulation using the exponential softening model with an interface reaches a peak load of 267 kN at a displacement of 48.6 mm, closely matching the experimental peak load with a minimal relative error. In comparison, the multilinear material model with an interface achieves a higher

peak load of 284 kN at the same displacement of 48.6 mm, indicating an overestimation of the peak load.

Both models exhibited better alignment with the experimental results compared to previous simulations without the interface. The exponential softening model provided a closer correlation with the experimental peak load and post-peak behaviour, suggesting a more accurate representation of the material's tensile response. While the multilinear model still overestimated the load-carrying capacity, it showed improvement over prior iterations. These findings highlight the importance of model selection in numerical analyses. To minimize the influence of modelling parameters when investigating the MDMM, consistency in model choices is essential. Despite some deviations, the proposed multilinear constitutive model does not significantly diverge from the experimental results and can thus be effectively used in further MDMM applications.

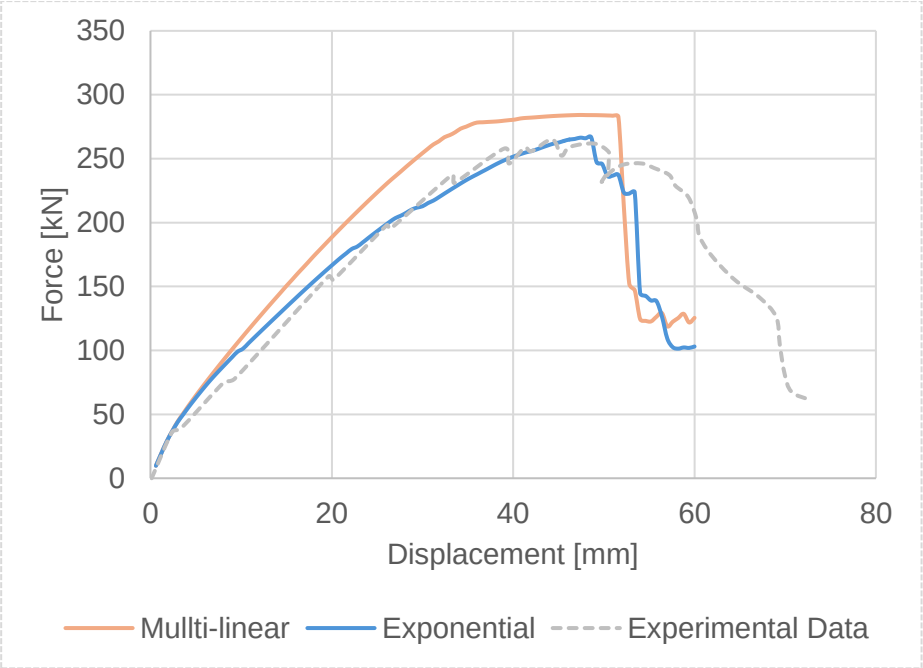

Figure 45 load-displacement curves comparing experimental data with numerical models using exponential and multilinear tensile material properties and interface between the beam and the steel plates.

5.4 ASR Affected beam under statical load

The next phase of the validation process focused on simulating ASR-induced damage under static load conditions using the same beam model and the proposed ATC. The primary objective is to evaluate the model's ability to capture the structural behaviour of an ASR-affected beam, with a focus on load-deflection response, load capacity, and failure mode.

Two modelling approaches were compared: the Modified Dual Mesh Method (MDMM), which simulated ASR as an applied expansion load, and the Reduced Material Properties Method (RMPM), which represented ASR effects through reductions in tensile strength and elastic modulus based on the expansion-material property relationship, Figure 28. To ensure consistency, a reference beam model without ASR effects was first tested until failure.

The MDMM simulations employed a phased procedure, as illustrated in Figure 46. Initially, self-weight and design load were applied with the shadow mesh inactive. Subsequently, prescribed strains representing ASR-induced expansion were applied to the structural mesh through the shadow mesh. In the final phase, the shadow mesh was deactivated, and deformation was incrementally applied until failure. Calibration was necessary to determine the equivalent free expansion on the structural mesh corresponding to the initial strain on the shadow mesh, as described in earlier chapters. In the RMPM, self-weight and design load were similarly applied first, followed by updating the material properties to reduced values reflecting the level of expansion, and then prescribed deformation was applied until failure, see Figure 46 .

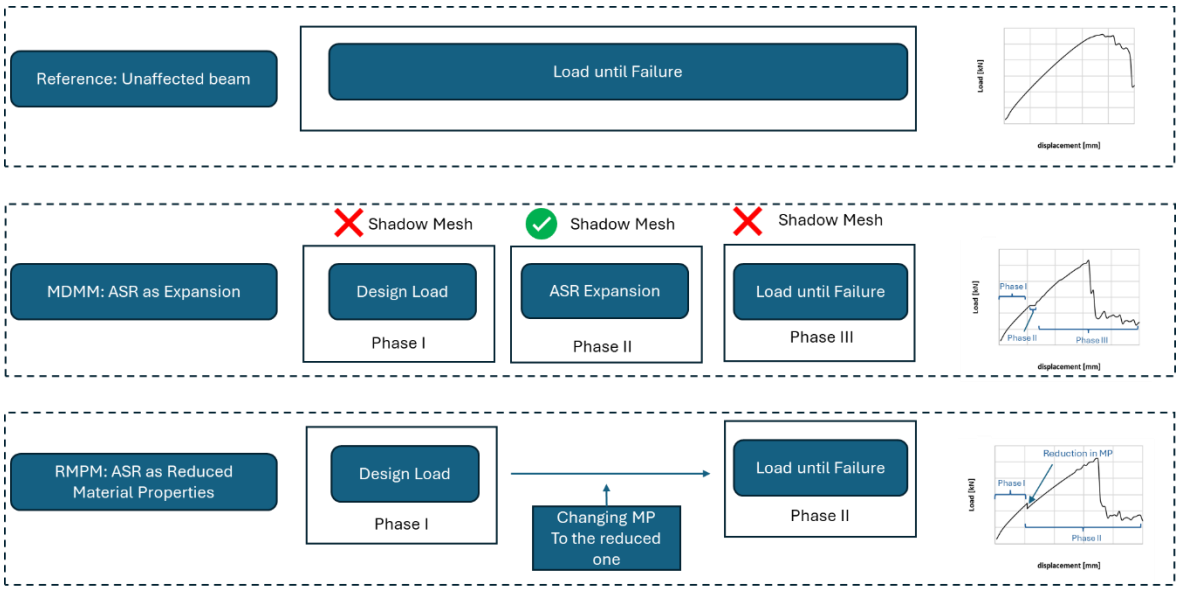

Figure 46 Simulation Procedure: ASR-Affected Beam Under Static Load

Three sub-cases were analysed to evaluate the performance of the two approaches under different conditions. The **first subcase**, Section 5.4.1, involved a marginal ASR expansion level of 0.03%, representing minor ASR effects. The **second subcase,** Section 5.4.2, simulated severe ASR-induced expansion with a high expansion level of 0.5%. The **third subcase,** Section 5.4.3, combined marginal ASR expansion (0.03%) with uniform prestressing equivalent to 20% of the concrete compressive strength, applied on the sides of the beam to investigate the combined effects of prestressing and ASR expansion.

Finally, a sensitivity study, in Section 5.4.4, was conducted to assess the influence of the numerical solution methods on the simulation's accuracy and robustness. This analysis compared the Regular Newton-Raphson method and the Secant method, examining their impact on convergence, computational efficiency, and the reliability of the simulation outcomes.

5.4.1 Subcase 1: Marginal ε^{ASR} Level (0.03%)

Figure 47 presents the load-displacement curves for three beams under different conditions. The reference beam serves as the baseline for comparison, showing the load-displacement behaviour of a beam with no ASR damage. This beam reaches a higher peak load and demonstrates greater deflection at peak load compared to the ASR-affected beams. In contrast, both ASR-affected beams show reduced peak loads and stiffer post-peak behaviour. MDMM demonstrates a lower peak load and reduced deflection at peak load compared to the reference beam, suggesting increased stiffness due to ASR-induced expansion. RMPM also shows a lower peak load and stiffer post-peak response. However, it exhibits more deflection at peak load than the ASR expansion model, though still less than the reference beam.

Both modelling approaches result in decreased peak loads and altered deflection behaviours compared to the reference beam. The difference in deflection at peak load between the two models highlights the importance of accurately representing ASR effects to predict the mechanical behaviour of affected concrete structures.

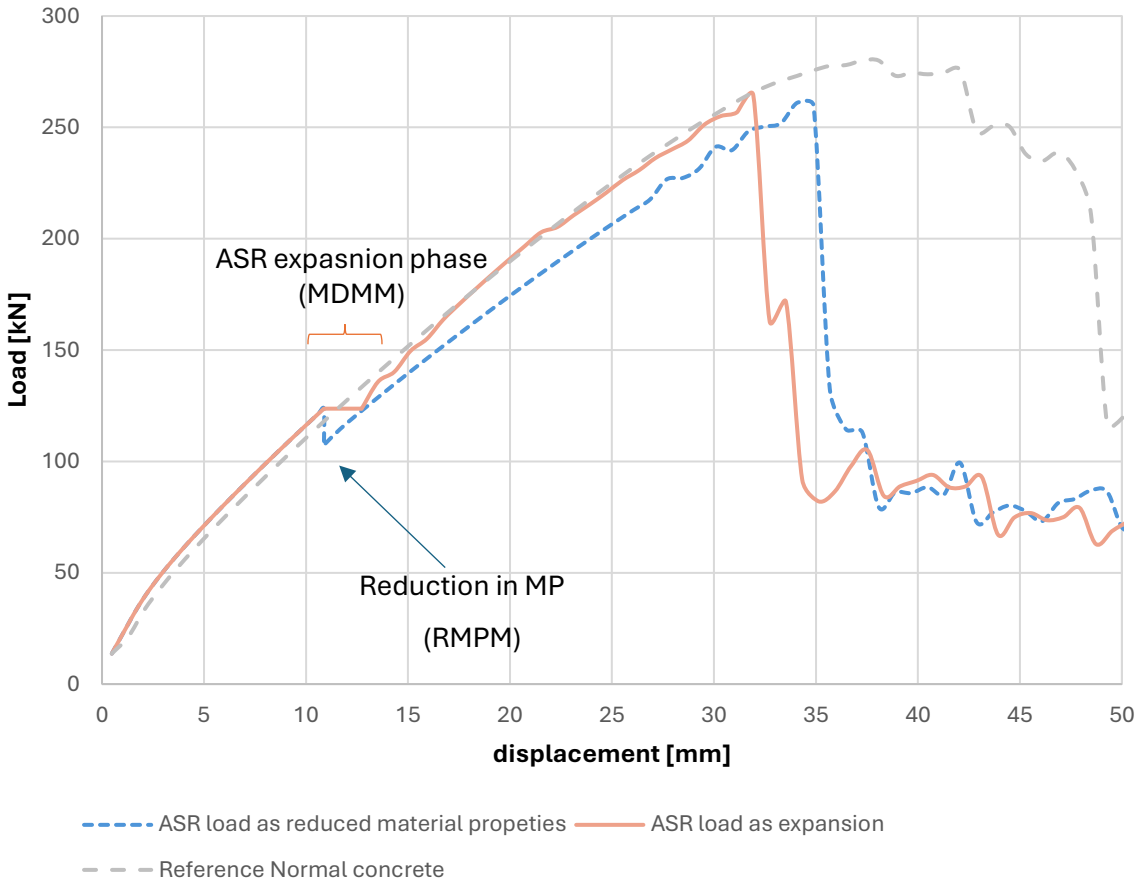

Figure 47 Load-displacement curves comparing the reference beam (unaffected), ASR-affected beam modelled using expansion (MDMM), and ASR-affected beam modelled using reduced material properties (RMPM).

Figure 48 compares the crack patterns at peak load for the three beams: Reference Beam Figure 48(a), Displays a typical crack pattern associated with flexural failure, with wider cracks indicative of ductile behaviour. MDMM, Figure 48(b) and RMPM , Figure 48(c), both exhibit similar crack patterns to the reference beam but with smaller crack widths.

Figure 49 illustrates the stress distributions at peak load, where Principal Concrete Stresses (S) indicate increased compressive stresses in the concrete, leading to crushing in the compression zone. And Steel Horizontal Stresses (SXX) and Steel Vertical Stresses (SYY) show the

development of tensile stresses in the reinforcement bars, with stress concentrations reflecting the altered load transfer due to ASR effects. The beams exhibit a flexural-compressive failure mode characterized by concrete crushing, consistent across all models. The ASR-affected beams reach this failure mode at lower loads, demonstrating that the developed models can simulate the reduction in structural capacity due to ASR.

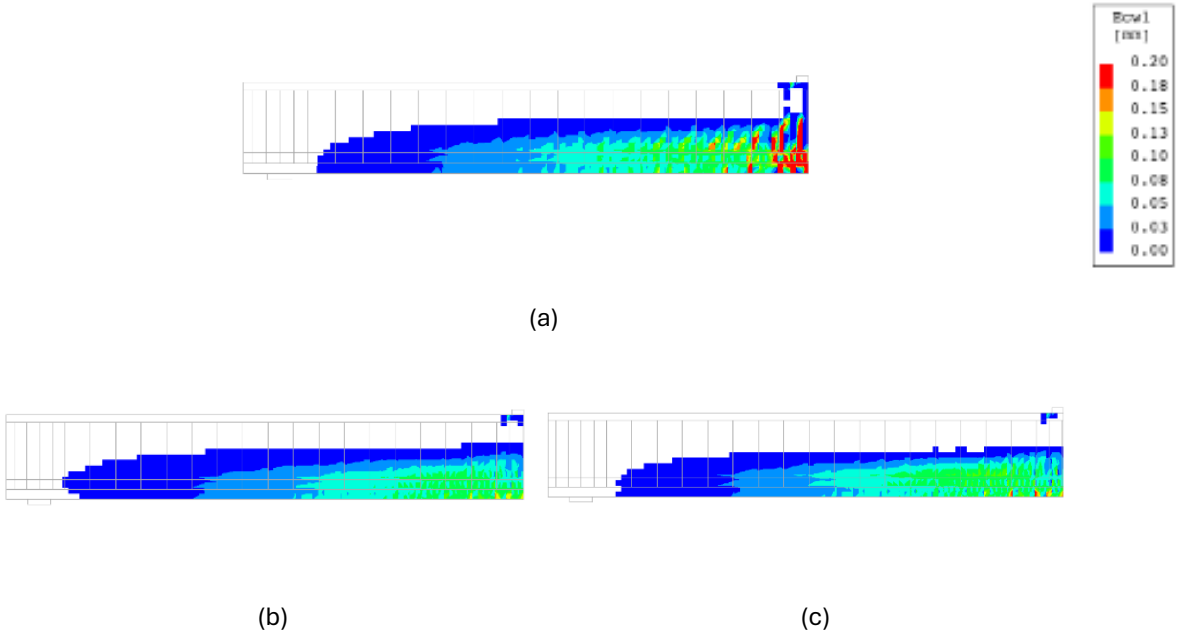

Figure 48 Ew1 crack width at peak load; (a) the reference beam; (b) MDMM; and (c) RMPM.

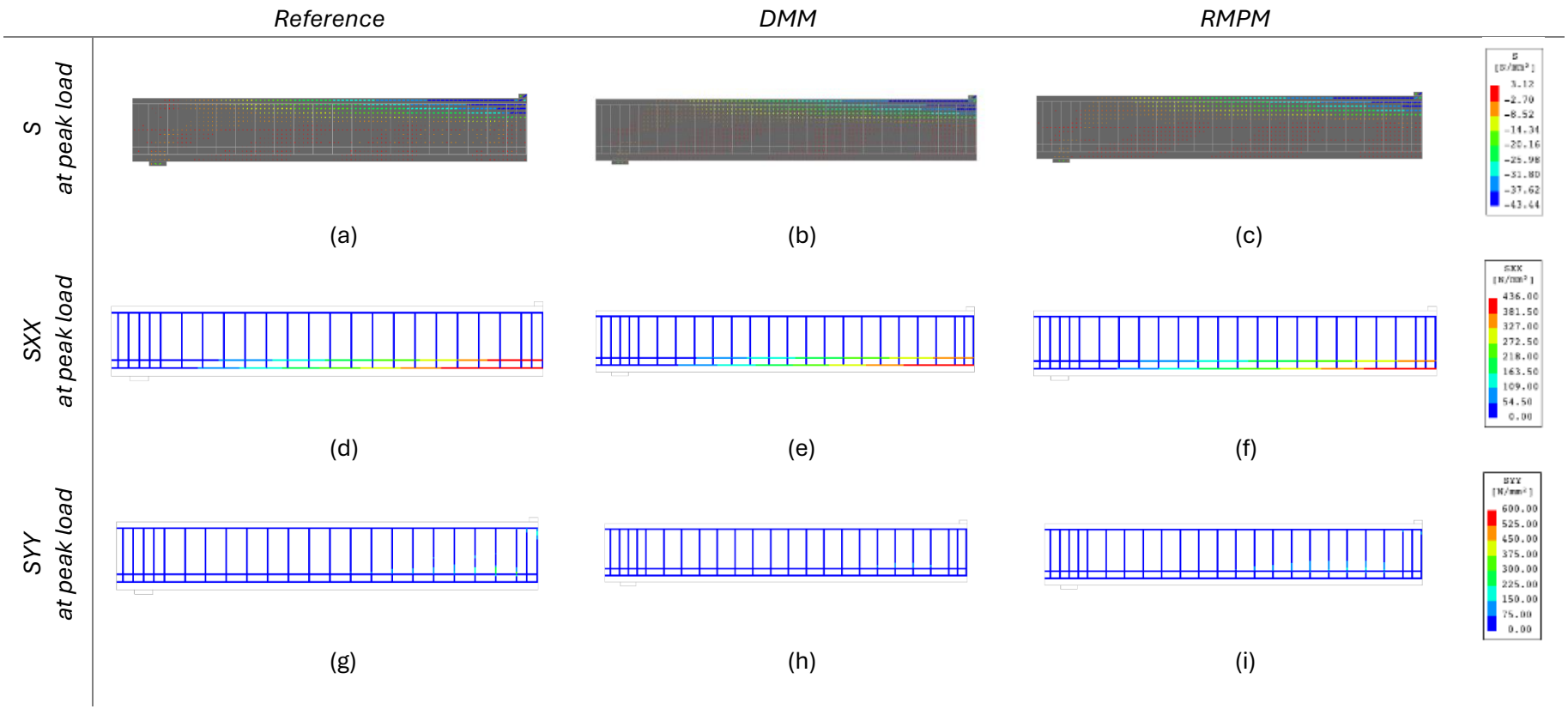

Figure 49 Principal concrete stresses (S), Horizontal steel stresses (SXX), and Vertical steel stresses (SYY) at peak load for reference (unaffected), MDMM, and RMPM

5.4.2 Subcase 2: Very High ε^{ASR} level (0.5%)

In this subcase, Figure 50 compares the load-displacement behaviour of three beams: the reference beam unaffected by ASR, the MDMM model simulating ASR-induced expansion, and the RMPM model simulating ASR effects through reduced material properties, both at an ASR expansion level of 0.5%. The reference beam achieves the highest peak load and greatest deflection at peak load. The MDMM model shows a significantly lower peak load and reduced deflection at peak load, indicating increased stiffness and decreased load capacity due to severe ASR-induced expansion. In contrast, the RMPM model also exhibits a lower peak load but displays more deflection at peak load than both the MDMM model and the reference beam, suggesting a more compliant response when ASR effects are modelled through material property reduction under severe conditions.

Figure 51 presents the crack patterns at peak load for the three beams. The reference beam exhibits typical flexural-compressive failure with cracks concentrated in the mid-span region and wider crack widths, indicative of ductile behaviour. The MDMM model shows damage distributed throughout the entire beam length, with numerous fine cracks and reduced crack widths, reflecting a more brittle failure mode due to severe ASR-induced expansion. The RMPM model displays a crack pattern similar to the reference beam, with cracks primarily in the mid-span region and comparable crack widths, indicating that the reduction in material properties affects load capacity but has less impact on crack distribution.

Figure 53 illustrates the stress distributions at peak load, where all models show increased compressive stresses in the concrete leading to crushing in the compression zone. The stress patterns in the reinforcement bars are similar across the models. The MDMM model's widespread damage highlights its capability to simulate the pervasive effects of severe ASR expansion on structural response and failure mode. In contrast, the RMPM model captures the reduction in load capacity but shows less alteration in crack patterns and stress distributions compared to the reference beam.

Figure 52 presents the load-displacement curves comparing the two ASR expansion levels, 0.03% and 0.5%, using the MDMM model. The 0.5% expansion level shows a slight reduction in load capacity compared to the 0.03% level. Additionally, the total deflection is higher for the 0.5% case. However, when focusing specifically on the static load portion, the 0.5% expansion results in less deflection than the 0.03% case, indicating a stiffer response under more severe ASR expansion.

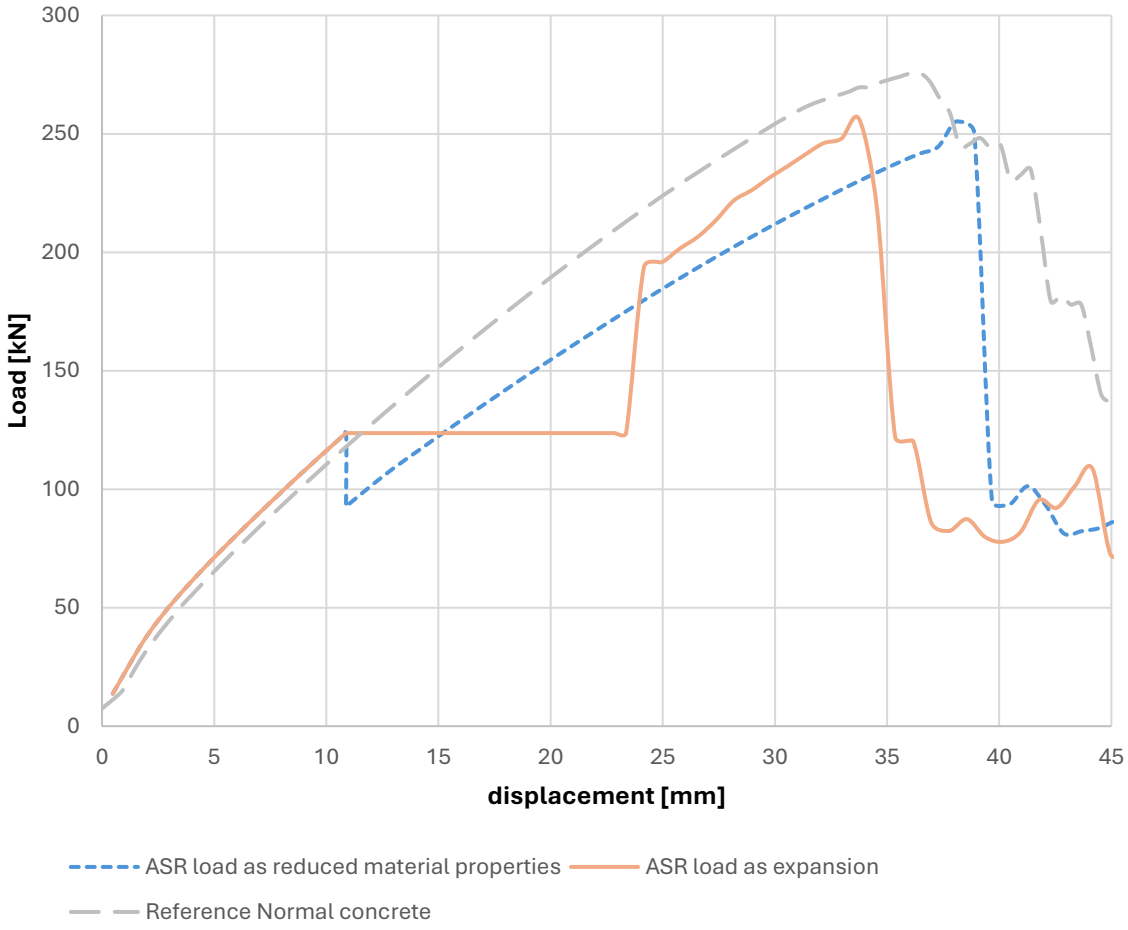

Figure 50 Load-displacement curves for the reference beam, MDMM, and RMPM under a very high ASR expansion level of 0.5%.

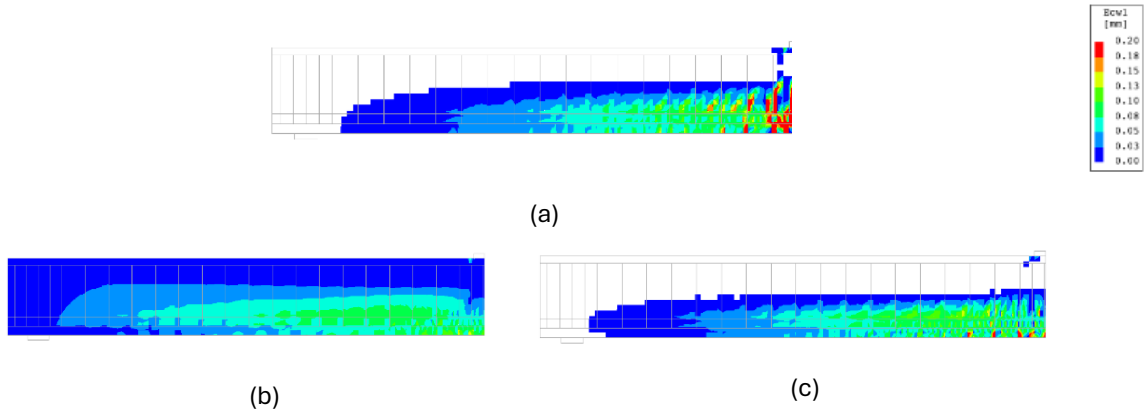

Figure 51 Ew1 crack width at peak load; (a) the reference beam; (b) (MDMM); (c) RMPM.

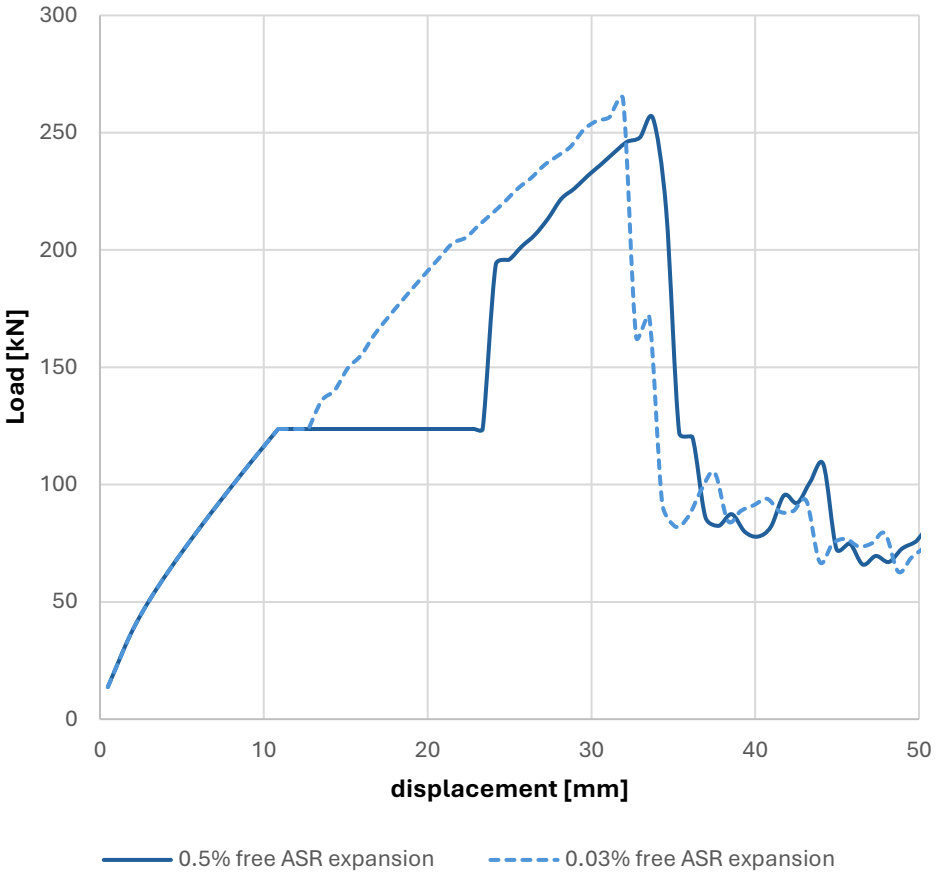

Figure 52 Load-displacement curves comparing ASR expansion levels of 0.03% and 0.5% using the MDMM.

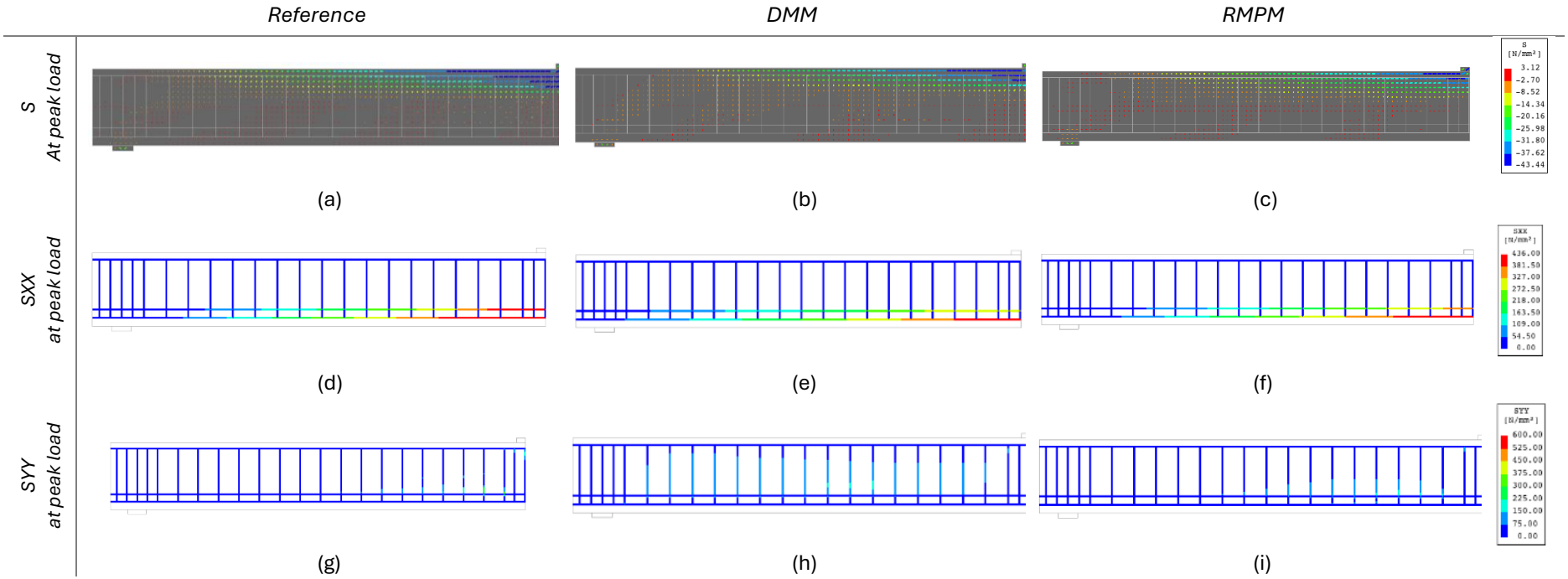

Figure 53 Stress distributions at peak load for the reference beam, MDMM model, and RMPM model under marginal ASR expansion (0.5%), Where: Principal concrete stresses (S), Horizontal steel stresses (SXX), and Vertical steel stresses (SYY)

5.4.3 Subcase 3: ASR Expansion with Uniform Prestressing

In this subcase, the beam is subjected to a marginal ASR expansion level of 0.03% combined with uniform prestressing applied on the sides of the beam, equivalent to 20% of the concrete compressive strength. Figure 54 presents the load-displacement curves for the reference beam, the MDMM model, and the RMPM model under the combined ASR expansion and uniform prestressing. The reference beam serves as the baseline. Both the MDMM and RMPM models exhibit a reduction in peak load compared to the reference beam, consistent with observations from previous subcases. The MDMM model shows reduced deflection at peak load, indicating increased stiffness due to the combined effects of ASR-induced expansion and prestressing. The RMPM model displays more deflection at peak load than the MDMM model but less than the reference beam, suggesting a differing influence of material property reduction on deflection behaviour.

Figure 55 illustrates the crack patterns at peak load for the three beams. The Reference Beam, Figure 55(a) shows typical flexural cracking. The RMPM Model, Figure 55(c), exhibits crack patterns similar to the reference beam but with less intensity with smaller crack width. The MDMM Model, Figure 55(b), shows a comparable crack pattern with slightly less distributed cracking and similar crack widths with RMPM. Additionally, Figure 56 presents the stress distributions at peak load, where no significant changes in failure mode or stress distribution patterns are observed compared to the previous cases.

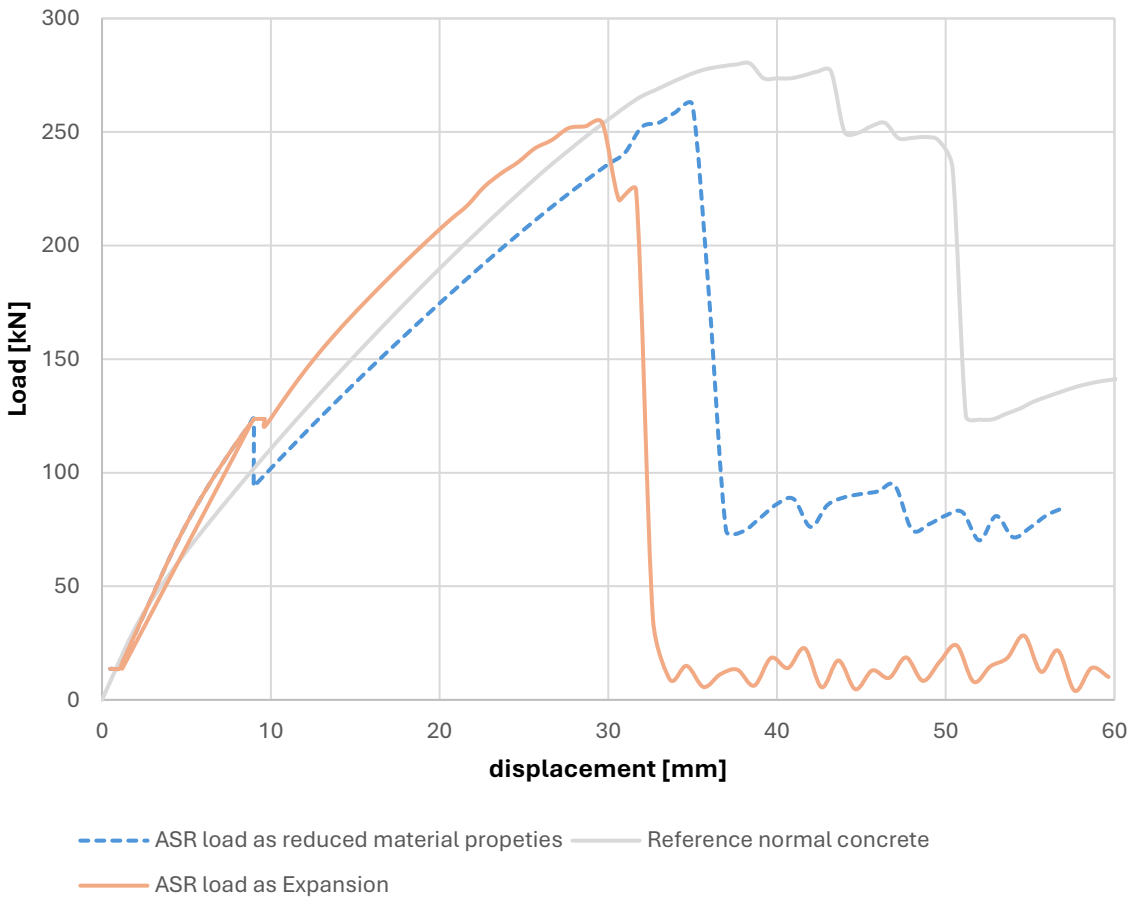

Figure 54 Load-displacement curves comparing the reference beam, MDMM model, and RMPM model under marginal ASR expansion (0.03%) with uniform prestressing.

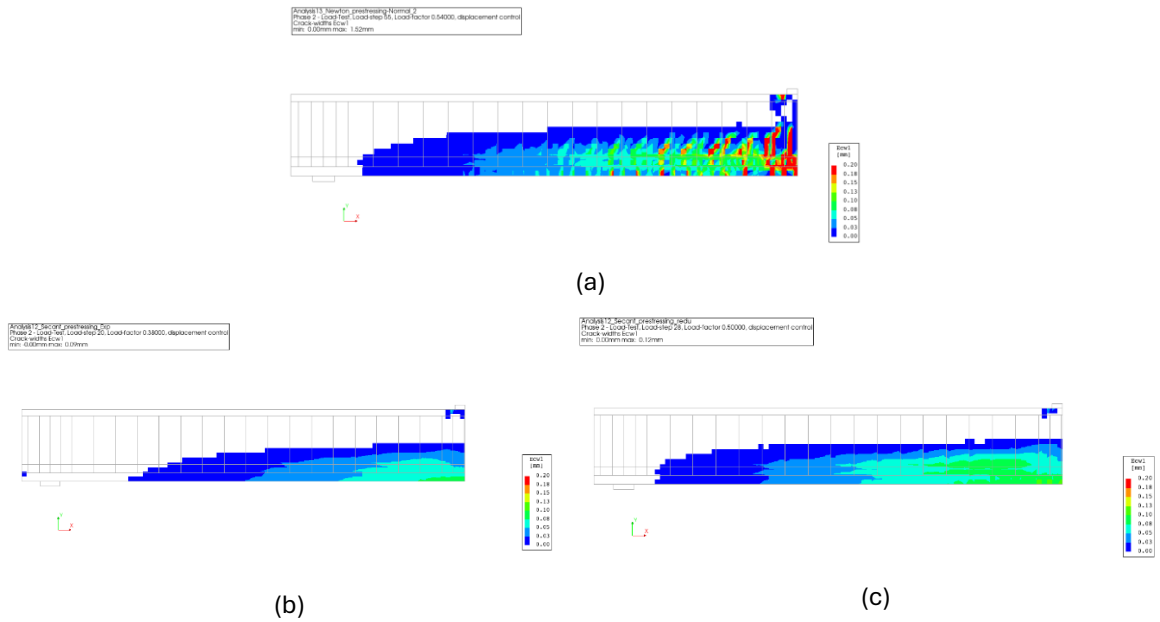

(a)

(b) (c)

Figure 55 Crack patterns at peak load for the reference beam (a), MDMM model (b), and RMPM model (c) under marginal ASR expansion (0.03%) with uniform prestressing.

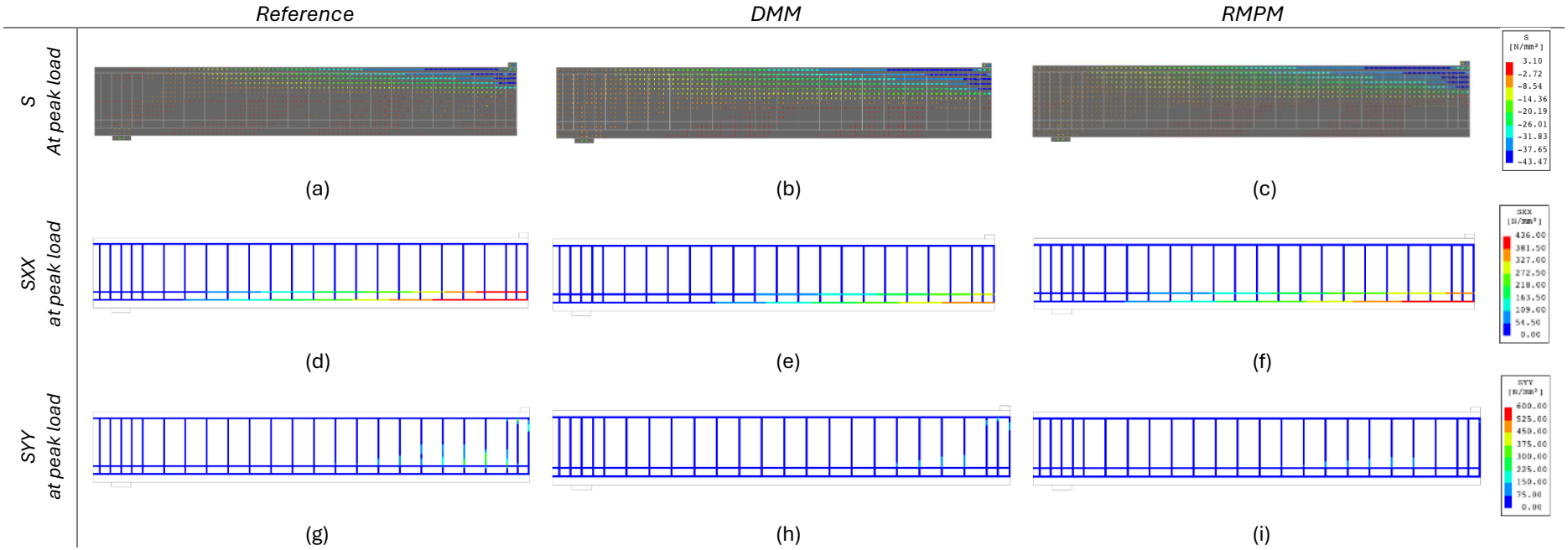

Figure 56 Stress distributions at peak load for the reference beam, MDMM model, and RMPM model under marginal ASR expansion (0.03%) with uniform prestressing, where: Principal concrete stresses (S), Horizontal steel stresses (SXX), and Vertical steel stresses (SYY)

5.4.4 Sensitivity Study on Structural Nonlinear Analysis: Newton Regular and Secant Methods

This sensitivity analysis aims to investigate the influence of the nonlinear iteration solution method on simulation results, specifically comparing the Regular Newton-Raphson method with the Secant solution method (Quasi-Newton). This analysis was prompted by computational challenges encountered during the phased analyses used for modelling Alkali-Silica Reaction (ASR) effects in both the Modified Dual Mesh Method (MDMM) and the Reduced Material Properties Method (RMPM).

During the analyses, transitioning between phases faced significant computational difficulties. For the RMPM, these challenges arose when material properties were updated to reflect ASR-induced degradation in the next phase. Similarly, in the MDMM, activating the shadow mesh and applying strain in subsequent phases caused non convergence and fatal errors. Despite efforts to address these issues by increasing step sizes, refining the mesh, or increasing the number of iterations, the errors remained, often with substantially increased computational time.

To resolve these challenges, the Secant solution method was employed during the expansion phase in MDMM and during the phase where the material properties were updated in RMPM. This method effectively addressed the fatal errors and allowed the analysis to proceed. However, initial observations suggested that the Secant method produced slightly lower peak loads and a more brittle post-peak response compared to the Regular Newton-Raphson method. Therefore, this sensitivity study was conducted to compare the computational and structural outcomes of these two methods and assess the implications of using the Secant method.

Results and Discussion

Figure 57 presents the load-displacement curves for Subcases 1, 2, and 3 using both the Regular Newton-Raphson method and the Secant solution method for all phases. It should be noted, in some cases, Figure 57 (c) and (e), curves generated using the Regular Newton-Raphson method are incomplete or missing due to analysis termination caused by fatal errors, despite adjustments to computational parameters.

The results indicate that both methods produce similar pre-peak behaviour. For MDMM simulations, both methods demonstrate lower ultimate capacity and reduced displacements compared to the reference beam. For RMPM simulations, lower peak loads and higher displacements are observed relative to the reference beam. This consistency confirms that the findings of the previous section are independent of the iteration method, reinforcing their validity. In the case of marginal ASR expansion with uniform prestressing, Figure 57 (e) , the MDMM's ultimate capacity, when using the Regular method, is comparable to that of the unaffected reference beam, showing no significant reduction. This is likely due to the combined effects of prestressing and the relatively low expansion level.

Key observations include:

1- The Regular Newton-Raphson method predicts slightly higher peak loads compared to the Secant method.
2- The Regular Newton-Raphson method exhibits more ductile post-peak behaviour, while the Secant method results in a more brittle response.
3- The Secant method is computationally faster and resolves convergence issues that arise with the Regular Newton-Raphson method in complex phased analyses.

These differences stem from the computational characteristics of the methods. The Regular Newton-Raphson method calculates an exact Jacobian matrix at each iteration, achieving high accuracy but at a higher computational cost. The Secant method uses an approximate Jacobian

matrix that is iteratively updated, reducing computational demands but introducing slight inaccuracies, particularly in post-peak behaviour [73].

Convergence behaviour also varies between the two. The Regular Newton-Raphson method exhibits quadratic convergence near the solution, enabling rapid convergence with an accurate initial guess, while the Secant method achieves superlinear convergence, [73], which is slightly slower but more robust in addressing complex nonlinear problems.

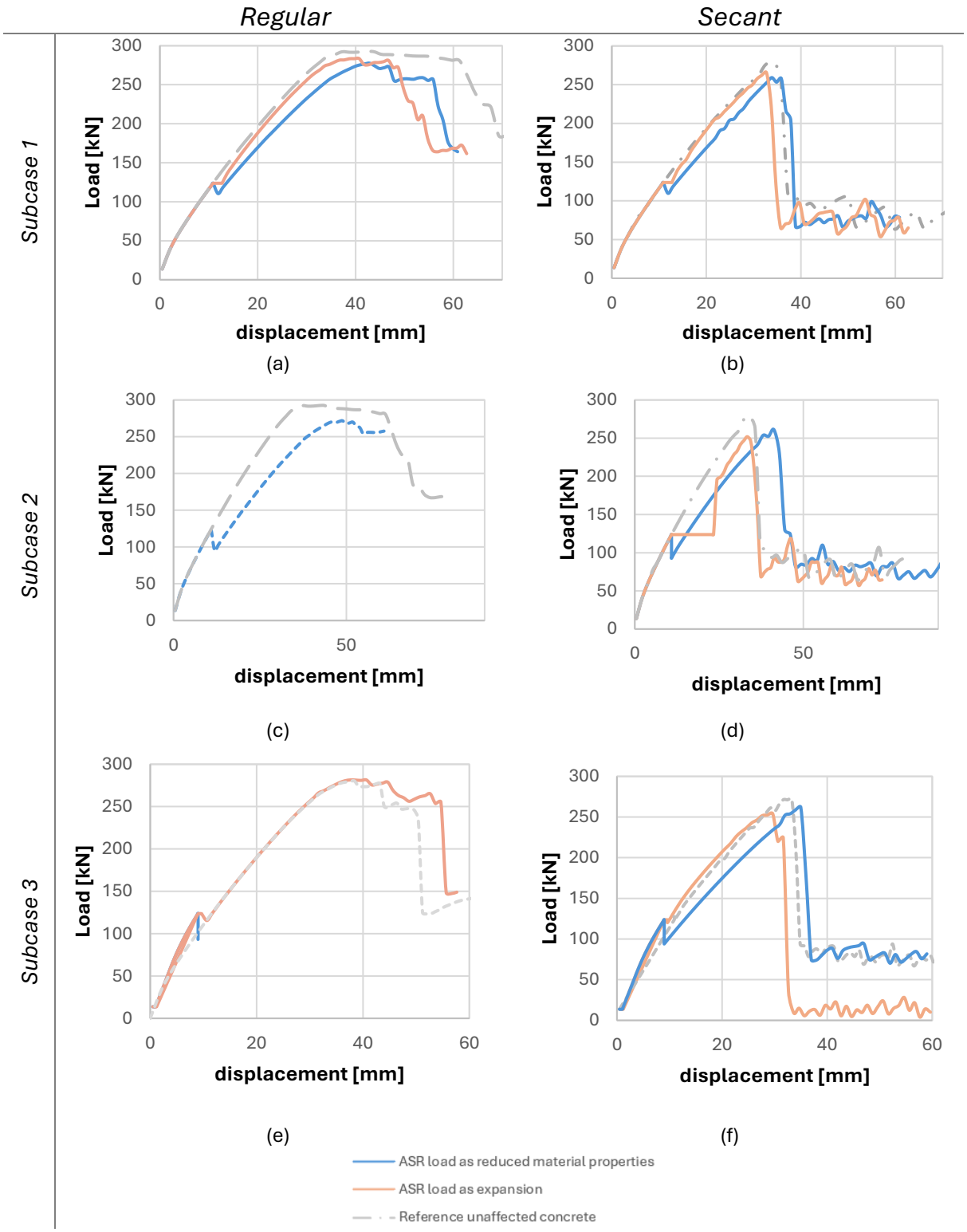

Figure 57 Load-displacement curves for Subcase 1, 2 and 3 using: Regular Newton-Raphson method and Secant solution method.

To further investigate the differences between the two iteration methods, a detailed comparison was conducted for a selected case involving a normal beam loaded until failure. Figure 58 displays the load-displacement curves, while Figure 59 and Figure 60 present the crack width (Ew1), principal stresses (S), and reinforcement stresses in the x-direction (SXX) and y-direction (SYY) at peak load and at a displacement of 60 mm, respectively.

From the load-displacement curves in Figure 58, similar observations to those mentioned earlier can be noted: both methods exhibit similar pre-peak behaviour, slightly lower peak load with the Secant method, and distinct differences in post-peak behaviour. The comparison of crack patterns, principal concrete stresses, and reinforcement stresses, shown in Figure 59 and Figure 60, at both peak load and 60 mm displacement revealed comparable failure modes predicted by the two solution methods. Both methods effectively captured the key structural response characteristics despite the observed differences in post-peak behaviour. The convergence results, shown in Figure 61, indicate that for both cases, where all steps successfully converged, the Secant method requires fewer iterations, further demonstrating its computational efficiency.

In conclusion, this sensitivity study highlights that while the Secant method effectively resolves convergence issues and reduces computational time, it may slightly underestimate peak loads and influence the accuracy of post-peak responses. These trade-offs should be carefully considered when selecting solution methods for nonlinear structural analyses involving phased processes, particularly for ASR-affected structures.

It should also be noted that a different iteration solution method can be chosen for each phase of the analysis. If the Secant method is used for all phases, approximation errors will accumulate across all phases. However, if the Secant method is applied only from a specific phase onward, the approximation effects will begin from that phase.

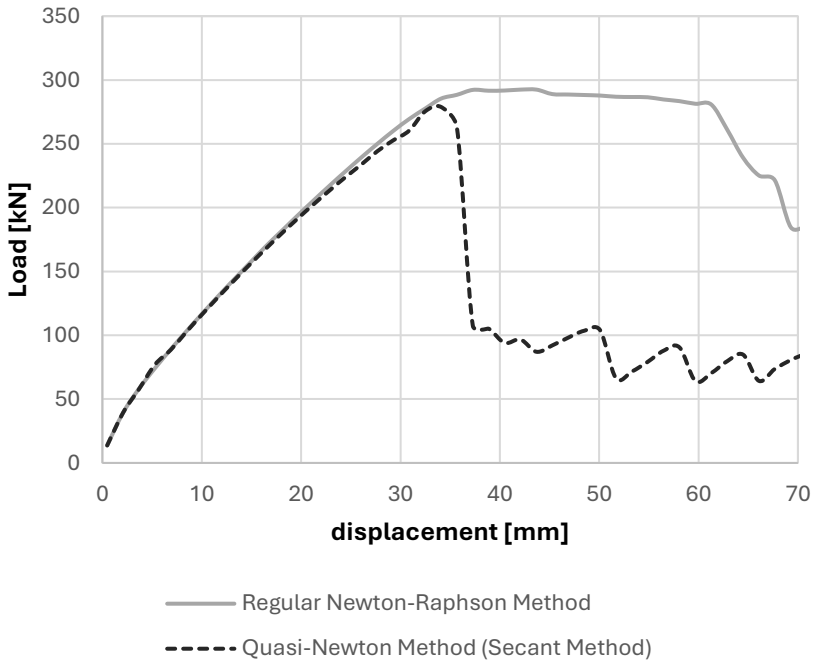

Figure 58 Detailed load-displacement curves comparing the two iteration methods for the selected case.

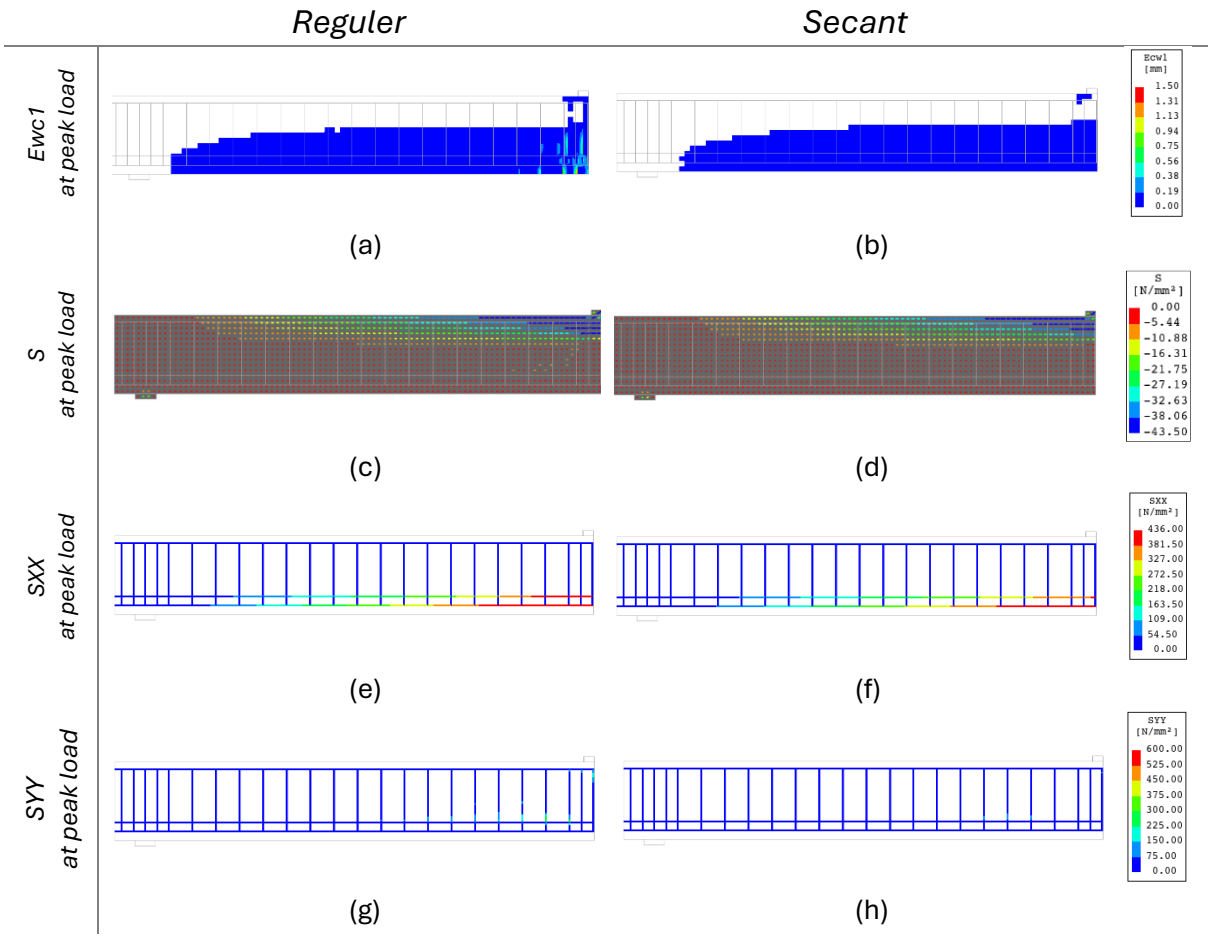

Figure 59 Crack width (Ew1), principal stresses (S), and reinforcement stresses (SXX, SYY) at peak load for both solution methods.

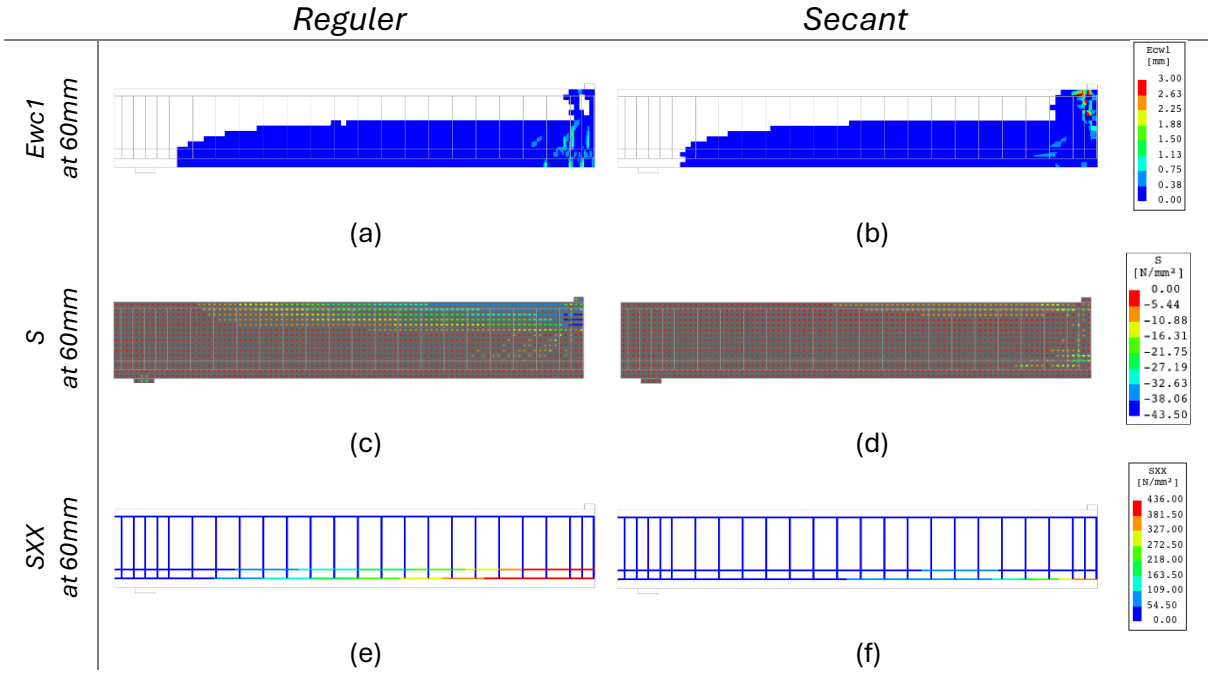

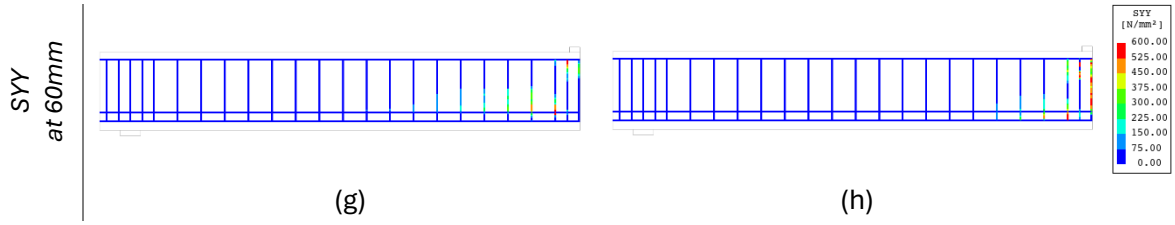

Figure 60 Crack width (Ew1), principal stresses (S), and reinforcement stresses (SXX, SYY) at 60 mm displacement for both solution methods.

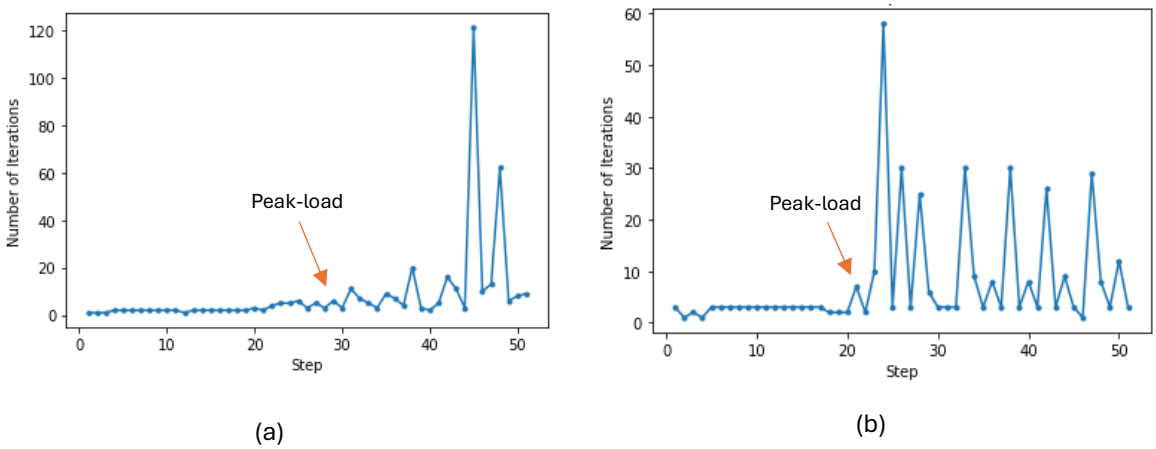

Figure 61 Results of convergence behaviour of the two iteration methods (a) Regular; and (b) Secant .

5.4.5 Discussion

In this analysis, a beam affected by ASR was modelled using two different approaches: the Advance Dual Mesh Method (MDMM) and a reduced material properties method (RMPM). An unaffected beam model tested until failure was used as a reference for comparison. For the ASR-affected beam, self-weight and design load were first applied. In the MDMM approach, ASR-induced expansion was simulated by applying strains of 0.03% (Marginal expansion) and 0.5% (Very high expansion) to the shadow mesh. In the RMPM, the concrete properties were degraded to represent the equivalent levels of expansion (0.03% and 0.5%), and both models were tested until failure.

The results demonstrated that both methods led to a reduced ultimate capacity for the ASR-affected beams, which aligns with existing literature on the influence of ASR on structural behaviour. However, key differences emerged between the two approaches:

1. **Ultimate Capacity**: Both the MDMM and RMPM approaches resulted in a lower ultimate load capacity compared to the reference beam, which agrees with the general observation that ASR weakens structural capacity. This reduction in strength is consistent with studies that highlight ASR-induced damage as a factor in structural degradation.
2. **Displacement Behaviour**: A notable difference was observed in displacement behaviour. According to the literature, ASR typically causes reduced displacement in affected structures due to the internal restraint induced by the ASR expansion. This was accurately captured by the MDMM approach, where the shadow mesh simulates the internal expansion forces and leads to restrained displacement. However, the RMPM approach resulted in greater displacement. This can be attributed to the lower stiffness of the material in this model, which did not introduce damage mechanisms in the concrete, thus delaying the activation of reinforcement and the onset of failure.
3. **Post-Peak Behaviour**: In both methods, the post-peak behaviour was more brittle compared to the unaffected beam, which is consistent with the brittleness commonly observed in ASR-affected concrete structures. However, the sensitivity analysis revealed that the iterative solution method had a significant influence on post-peak behaviour, contributing to variations in results and affecting the ultimate capacity by approximately 5%. This observation underscores the need for careful selection of numerical parameters to ensure that results are interpreted correctly and not misattributed to physical phenomena.

The MDMM approach, by simulating the actual expansion behaviour of ASR, provides a more realistic representation of the internal stress and displacement changes caused by ASR-induced expansion. In contrast, the reduced material properties approach, while simpler, does not capture the same level of internal strain development, leading to differences in displacement behaviour and delayed reinforcement activation.

Furthermore, the sensitivity of post-peak behaviour to numerical solution methods emphasizes the importance of understanding the limitations of modelling techniques. Variations in numerical choices can significantly impact the interpretation of results, and careful consideration is required to avoid attributing numerical artifacts to physical phenomena.

5.5 ASR affected beam under gradual expansion

This section presents the simulation of ASR-induced damage development in concrete structures, using the same beam model as in the previous analyses. The objective is to assess the MDMM's ability to capture the progression of ASR effects under gradual expansion conditions.

The analysis consists of two primary phases, as illustrated in Figure 62:

1. **Initial Phase**: The beam is subjected to self-weight and a design load equivalent to 40% of its ultimate load capacity. During this phase, the shadow mesh remains inactive.
2. **ASR Expansion Phase**: The shadow mesh is activated, and an initial strain equivalent to free ASR expansion is applied. In this scenario, the structural mesh restrains the ASR-induced expansion, simulating the real-world conditions where structural components limit expansion.

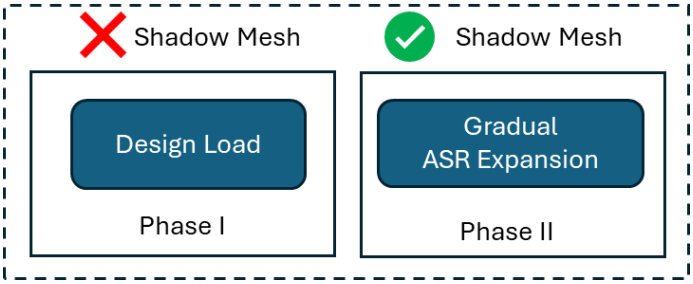

Figure 62 Simulation Procedure: ASR affected beam under gradual expansion.

Before applying ASR expansion in the beam model, a calibration step was performed to determine the equivalent free expansion on the structural mesh associated with the imposed strain on the shadow mesh. This calibration was conducted using a 2D concrete model as described in the previous chapter. Figure 60 illustrates the relationship between the initial imposed strain on the shadow mesh and the resulting free expansion on the structural mesh.

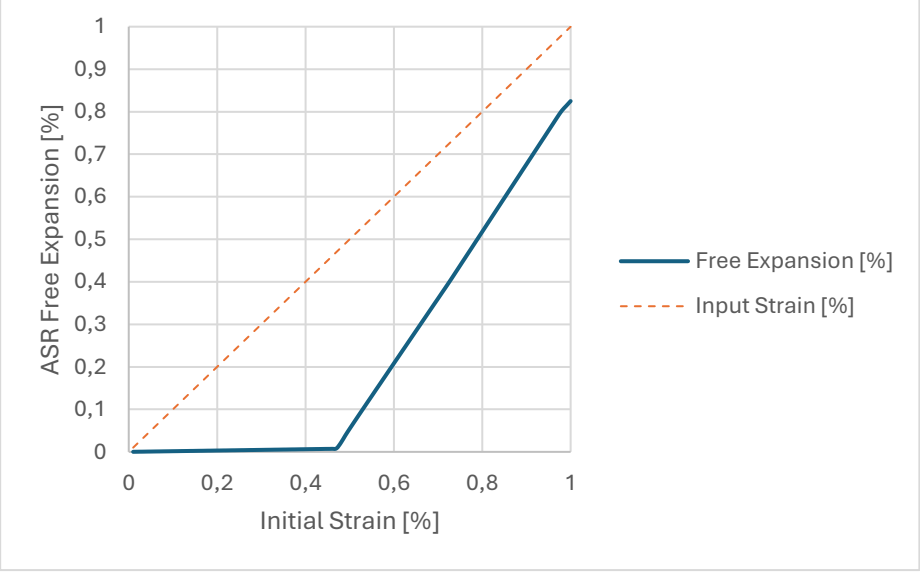

Figure 63 Calibration curve where the equivalent free expansion on the structural mesh associated with the initial imposed strain on the shadow mesh.

5.5.1 Results & Discussion

Figure 64 and Figure 65 show the progression of cracking strain and patterns at various expansion levels. The model results show:

- **Before ASR Initiation (0% Expansion)**: Under self-weight and the applied design load, vertical cracks appear at the bottom mid-span of the beam, typical of bending-induced cracking due to flexural stresses.
- **Early ASR Expansion Stages (0.005%, 0.007%, 0.07%, 0.21% Expansion)**: As ASR expansion begins, existing cracks propagate, and new cracks emerge adjacent to them. Crack orientation starts to shift, with horizontal cracks forming parallel to the longitudinal reinforcement at the top and bottom of the beam. Diagonal cracks also develop around the stirrups, indicating changing stress distribution.
- **At 0.5% Expansion (First Instance of Steel Yielding)**: The first stirrup yields, indicating a critical expansion level where the reinforcement begins to experience significant stress. The crack pattern becomes more extensive, with numerous cracks developing throughout the beam.
- **At 0.83% Expansion**: Cracking becomes widespread, and the beam experiences substantial degradation, demonstrating the model's ability to simulate the severe effects of advanced ASR-induced damage.

Figure 64 also presents the reinforcement stresses in both the x-direction (SXX) and y-direction (SYY) at key expansion levels:

- **At 0% Expansion**: Reinforcement stresses remain within elastic limits, corresponding to the initial loading conditions without ASR effects.
- **At 0.5% Expansion**: The stirrups begin to yield as ASR-induced expansion generates internal stresses that exceed the yield strength of the steel reinforcement.
- **At 0.83% Expansion**: More reinforcement elements surpass the yield point, reflecting the increased stresses due to ongoing ASR expansion.

To conclude, the MDMM effectively simulates the initiation and evolution of cracks, capturing the transition from vertical bending cracks to horizontal and diagonal cracks as ASR expansion increases. The model also successfully identifies the point at which the stirrups yield, marking a critical threshold where the structural integrity begins to significantly deteriorate. Additionally, the restrained expansion by the structural mesh leads to widespread cracking and a notable loss of structural performance, accurately reflecting the interaction between ASR-induced expansion and the structural elements.

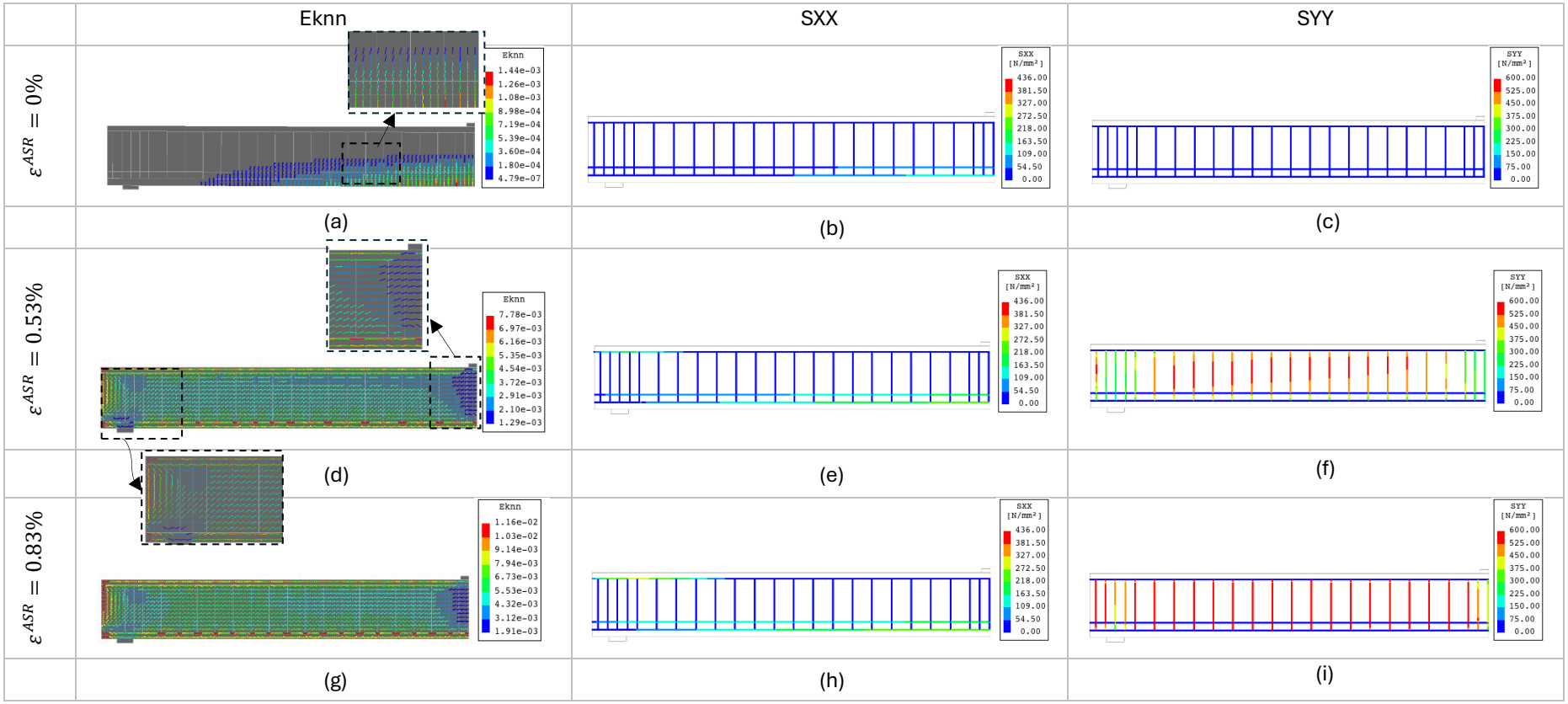

Figure 64 Cracking strain (Eknn) and patterns, along with reinforcement stresses (SXX and SYY), at expansion levels of 0%, 0.53%, and 0.83%.

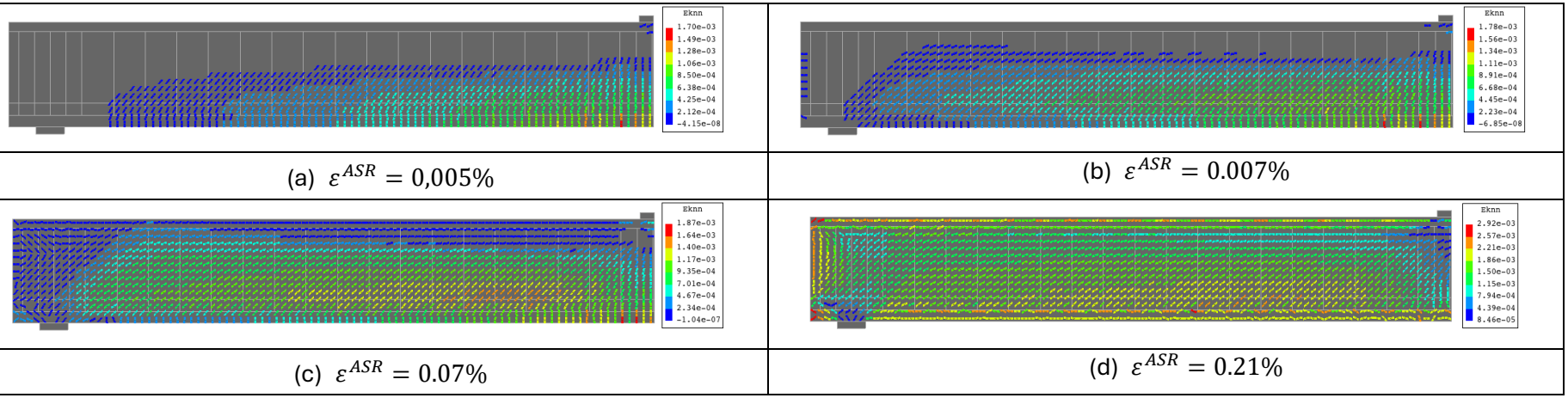

(a) $\varepsilon^{ASR} = 0{,}005\%$ (b) $\varepsilon^{ASR} = 0.007\%$

(c) $\varepsilon^{ASR} = 0.07\%$ (d) $\varepsilon^{ASR} = 0.21\%$

Figure 65 Cracking strain and patterns at various ASR expansion levels: (a) 0.005%, (b) 0.007%, (c) 0.07%, and (d) 0.21%

5.6 Conclusion

This chapter evaluated the Modified Dual Mesh Method (MDMM) by applying it to a concrete beam fails in bending and comparing its performance against alternative modelling approaches. The key findings and insights from the validation and analysis are as follows:

The similar configuration of Toronto Beam Test VS-C3 was employed to validate the MDMM. Numerical simulations using both linear and multilinear constitutive models aligned reasonably well with experimental data in terms of load-displacement behaviour and crack patterns. While the multilinear model demonstrated improved accuracy over the linear model, some deviations in post-peak behaviour and peak load were noted, underscoring the limitations of the selected material models in fully capturing ductile behaviour.

The MDMM was evaluated for its ability to simulate ASR-induced expansion in beams under static load conditions. Comparisons between the MDMM and the Reduced Material Properties Method (RMPM) highlighted distinct differences:

- The MDMM captured the internal stresses and displacement behaviour due to ASR expansion more realistically.
- The RMPM, while simpler, showed greater deflection at peak load due to the absence of internal expansion forces, leading to delayed reinforcement activation. These results confirmed the MDMM's superior capability in representing the internal mechanics of ASR-induced damage.

The MDMM successfully simulated the progression of ASR-induced damage under gradual expansion conditions. It captured critical stages of structural degradation, including crack evolution and reinforcement yielding, reflecting real-world damage progression. The transition from bending-induced vertical cracks to horizontal and diagonal cracks due to ASR expansion was effectively represented.

A sensitivity analysis comparing solution methods revealed differences in convergence behaviour and post-peak responses. The Secant solution method proved more robust for complex models, although it introduced a slightly more brittle response. These findings highlight the importance of selecting appropriate numerical settings to ensure reliable results.

This chapter demonstrated the MDMM's ability to simulate ASR-induced damage under various conditions, showcasing its potential as a practical and reliable tool for structural assessments. The comparative analysis highlights the importance of accurately modelling ASR-induced expansion to capture internal stress development and structural degradation. The findings also highlighted the need for further refinement of material models to improve post-peak behaviour representation and ensure alignment with experimental observations.

6. Material Models

In the previous two chapters, MDMM was developed and tested, demonstrating its potential to model ASR effects on structural performance. Within the MDMM framework, ASR-free expansion is introduced as an input through a shadow mesh, and the tensile curve is adapted to reflect strength degradation and potential damage. However, the input parameters previously used to represent ASR expansion and material degradation were not necessarily drawn from realistic field conditions. Moreover, a direct and reliable correlation between expansion increments and time is still needed to more accurately predict the progression of ASR in concrete structures.

This chapter will focus on forecasting long-term free ASR-induced expansion and the resulting degradation of material properties based on experimental data. the main objectives of this chapter are:

1. **Time-Expansion Correlation (Section 6.1):** Develop a relationship that links ASR-free expansion to time, enabling the structural model to predict ASR progression over time.
2. **Expansion-Material Degradation Correlation (Section 6.2):** Determine how ASR-induced expansion relates to the reduction of material properties, allowing for representation of tensile strength and stiffness changes as expansion increments increase.

By integrating established phenomenological models—Larive's expansion prediction model [55] and Esposito's material degradation model [27] —with available case study data and relevant literature, this chapter provides a consistent framework for characterizing ASR behaviour. The results of this chapter will be employed in the following chapter, Chapter 7, where a hypothetical bridge pier cap is analysed to demonstrate how the proposed approach works within a practical, structural-scale scenario.

6.1 Larive's Expansion- time Prediction Model

6.1.1 Larive's Equations

The time-based correlation for ASR-induced expansion is established using Larive's semi-empirical model. This model characterizes the kinetics of ASR-induced expansion through three primary parameters: ultimate expansion ($\varepsilon\infty$), latency time (τ_L), and characteristic time (τ_C), as shown in Equation (2), [55]:

$$\varepsilon(t,\theta) = \frac{1 - e^{-\frac{t}{\tau_c(\theta)}}}{1 + e^{-\frac{t-\tau_L(\theta)}{\tau_c(\theta)}}} \times \varepsilon^{\infty} \tag{2}$$

In this equation, ε (t, θ) represents the ASR-induced expansion at time t and temperature θ. The latency time τ_L corresponds to the initial phase before significant expansion occurs, while the characteristic time τ_C indicates the rate at which expansion progresses after this initial period. Both τ_L and τ_C are temperature-dependent, defined by the following equations adapted from Ulm et al. [56]:

$$\tau_c(\theta) = \tau_c(\theta_0)\left[U_C\left(\frac{1}{\theta} - \frac{1}{\theta_0}\right)\right] \tag{3}$$

$$\tau_L(\theta) = \tau_L(\theta_0)\left[U_L\left(\frac{1}{\theta} - \frac{1}{\theta_0}\right)\right] \tag{4}$$

Here, θ is the absolute temperature (where θ in K = 273 + T °C), and θ_0 is the reference absolute temperature, usually corresponding to the exposure temperature used in laboratory tests. The constants U_C and U_L are thermal activation parameters derived from the Arrhenius equation, with values:

$$U_c = 5400 \pm 500K \quad (5)$$

$$U_L = 9400 \pm 500K \quad (6)$$

Each set of parameters is specific to a given temperature (θ). It's important to note that both characteristic and latency times are primarily mathematical parameters without a clear physical meaning.

6.1.2 Parameters Determination

To apply Larive's model for time-expansion correlation, specific parameters are determined:

- **θ_0, U_C, and U_L**: These are obtained according to the accelerated tests. In this study, these values are assumed based on the available data, see Table 7.
- **$\tau_C(\theta_0)$ and $\tau_L(\theta_0)$**: These parameters are iteratively fitted to achieve the best alignment with available expansion data, see Table 7.
- **Ultimate Expansion (ε^∞)**: This critical parameter represents the total expected expansion, comprising both past expansion (ε_1) and residual (future) expansion (ε_1) also referred as (ε^{Res}):

$$\varepsilon^{Res} = \varepsilon_2 \quad (7)$$

$$\varepsilon^{\infty} = \varepsilon_2 + \varepsilon_1 \quad (8)$$

The residual expansion (ε_2) was estimated from the results of accelerated expansion tests on extracted core samples, which were available for this case. However, estimating past expansion (ε_1) can be challenging due to limited historical data. While detailed petrographic analyses and historical records can provide insights into ASR progression to date [2], [15], as illustrated in Figure 66, these data are unavailable for this study. To address this limitation, an alternative back-calculation method was employed, utilizing literature-based data on material degradation. The observed reductions in material properties were correlated with an appropriate level of expansion using data collected by Esposito et al.'s [27]. Subsequently, a curve-fitting approach, based on the accelerated expansion test results available from the case study, was applied to determine the ultimate expansion level and to upscale the laboratory time scale to real-world time scales.

Table 7 Larive's parameters

θ_0	U_C	U_L	τ_c (θ0) *	τ_L (θ0) *
311 K	5400	9400	50	200

*Initial assumption

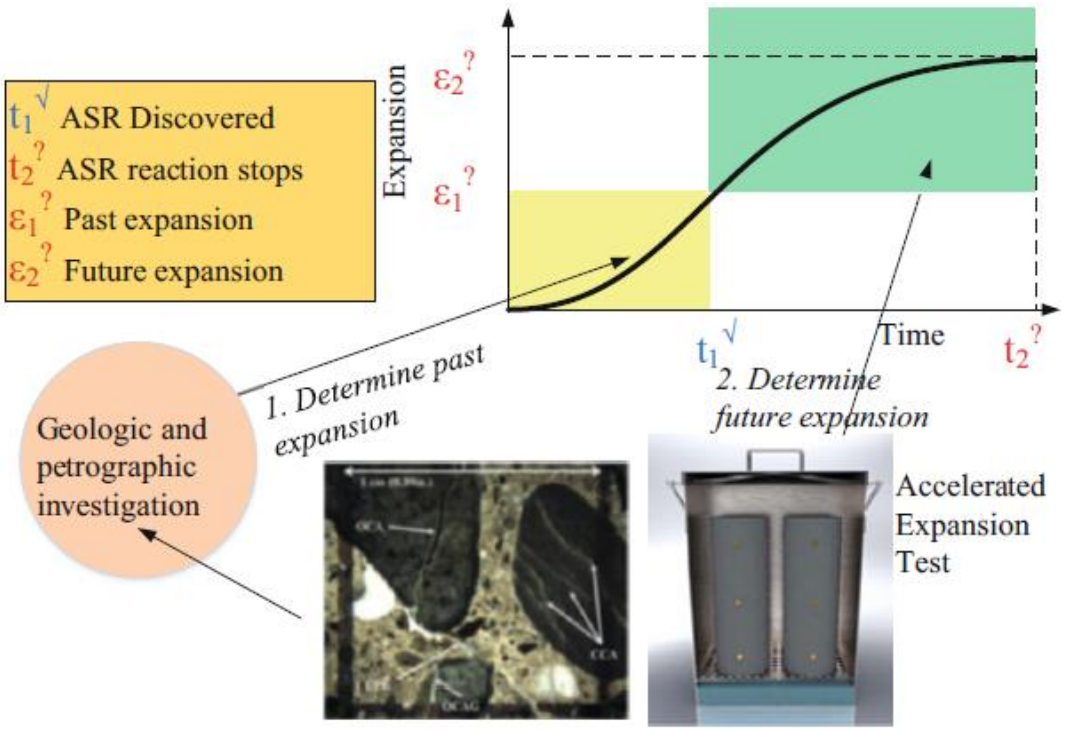

Figure 66 Estimate of past and future expansion [15]

6.1.3 Available data from a Case Study

An existing concrete infrastructure, constructed approximately 60 years ago, has been diagnosed with Alkali-Silica Reaction (ASR). To evaluate the extent of the damage and predict future expansion, core samples were extracted from the structure and subjected to accelerated expansion tests, see Figure 67. The original design material properties, estimated from historical data, are summarized in Table 8. Over time, these properties have been reduced due to the ASR expansion (ε_1), as shown in Table 9. The specific percentage reductions attributable to residual expansion are detailed in Table 10, while the reductions associated with total expansion are presented in Table 11.

Material Properties

Table 8 Original Design Material Properties

Property	Design Value
Mean Compressive Strength	36 MPa
Mean Tensile Strength	2.77 MPa
Mean Splitting Tensile Strength	3.1 MPa
Modulus of Elasticity	32310 MPa

Table 9 Current Material Properties at t_1= 60 years

Property	Design Value
Mean Compressive Strength	48 MPa
Mean Tensile Strength	3.10 MPa

Mean Splitting Tensile Strength	2.99 MPa
Modulus of Elasticity	25,000 MPa

Table 10 Material Property Reduction only due to Residual Expansion

Property	**Reduction due to Residual Expansion (%)**
Mean Compressive Strength	± 15%
Mean Tensile Strength	± 10%
Modulus of Elasticity	± 10%

Table 11 Material Property Reduction due to Ultimate Expansion

Property	**Reduction at Total Expansion (%)**
Mean Compressive Strength	± 25%
Mean Tensile Strength	± 60%
Modulus of Elasticity	± 40%

Accelerated Expansion Test Results

The accelerated expansion tests performed on the extracted core samples indicate a total residual expansion (ε^{Res}) of 0.04%, as illustrated in Figure 67. Additionally, laboratory samples replicating the design material properties were subjected to similar tests. These tests, which have so far shown a free expansion of 0.0004% after 100 days, are critical not only for predicting future damage but also for more accurately estimating past expansion. However, this approach requires additional time and effort, as the detailed comparison between the laboratory samples and the residual expansion observed in the core samples is necessary to achieve a precise reconstruction of the structure's historical ASR progression.

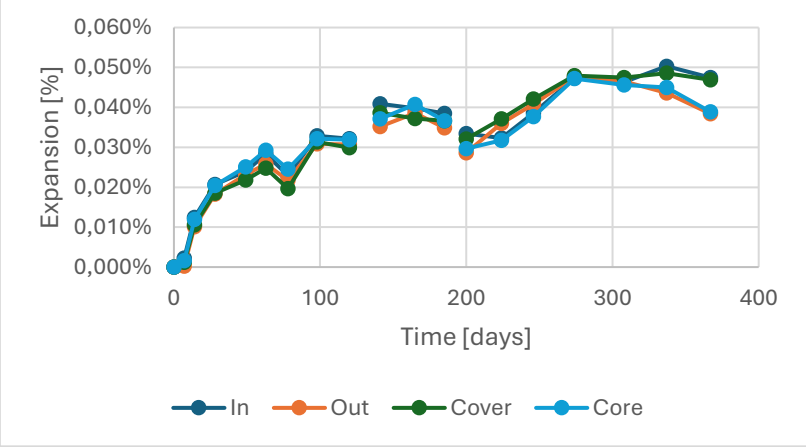

Figure 67 Residual Free Expansion Curves of Extracted Core Samples from Various Locations within the Structure exposed to accelerated expansion test.

6.1.4 Proposed Process

The following process outlines the steps to determine the time-expansion correlation using Larive's model, available case study data, literature. The results of this process are presented in **Section 6.1.5.**

Input Requirements

- **t0**: the original design properties of the concrete at the time of construction, including mean compressive strength, tensile strength, splitting tensile strength, and modulus of elasticity, listed in Table 8.
- **t1 = 60 years**: the current material properties and chemical composition of the concrete mixture at the time of extraction, 60 years post-construction, listed in Table 9.
- **t2**: residual expansion and updated material properties at the point of ultimate expansion (t_2) determined from accelerated tests on extracted core samples, Table 11 and Figure 67.

Step 1: Determine Past expansion (ϵ_1)

To estimate the past expansion (ϵ_1), the splitting tensile strength reduction observed at t_1, Equation (9), was matched to the corresponding expansion level on literature-based data curve from Esposito et al.'s [27] .

From Table 8 and Table 9, the splitting tensile strength at t_0 was 3.1 MPa and at t_1 was 2.99 MPa, resulting in a normalized value:

$$\frac{2.99}{3.11} = 0.96 \tag{9}$$

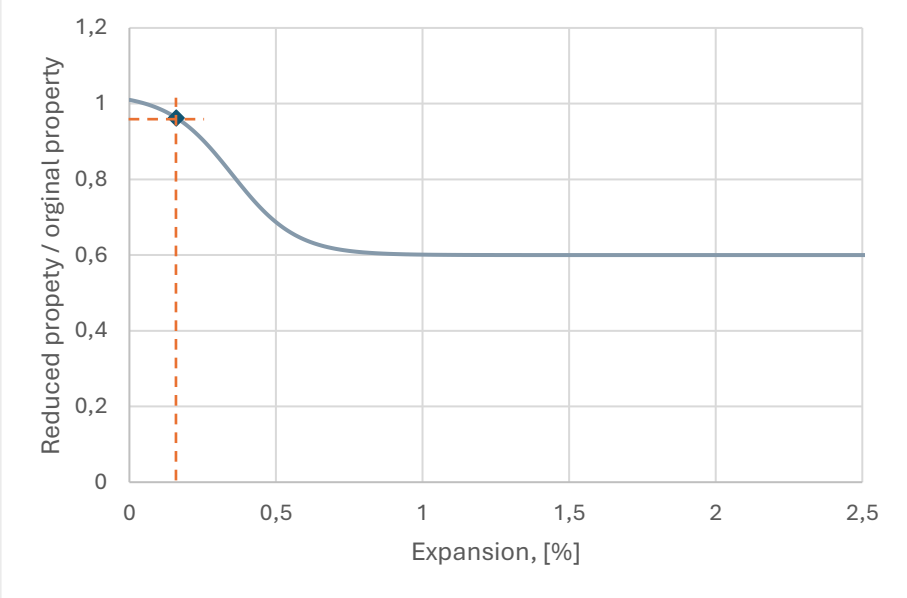

Figure 68 Normalized splitting tensile strength reduction curve based on collection of literature data adopted from [27].

From Figure 68, the equivalent expansion to this reduction at t_1 (expansion to-date) can be estimated:

$$\varepsilon_1 \approx 0.16\% \tag{10}$$

Step 2: Determine Total Expansion (ϵ^{∞})

The residual expansion (ϵ_2) was obtained from the accelerated expansion test results, where:

$$\varepsilon_2 = \varepsilon^{Res} \approx 0.04\% \tag{11}$$

Combining the past expansion (ϵ_1) and residual expansion (ϵ_2), the ultimate expansion ($\epsilon\infty$) was calculated as:

$$\varepsilon^{\infty} = 0.20\% \quad (12)$$

Step 3: Plot, Calibrate and Fit the Expansion Curve

The estimated ultimate expansion (ϵ∞) and the results from residual expansion tests were used to plot, calibrate, and fit an initial expansion curve.

Step 4: Refine the Expansion Curve Using Laboratory Data

The calibrated expansion curve was further refined by incorporating measured expansion values from laboratory samples (e.g., 0.0004% expansion after 100 days). These samples replicated the original design material properties of the structure, ensuring the relevance of the curve to the specific ASR-affected structure. The final Larive's model parameters are listed in Table 12.

Table 12 final Larive's equation parameters

θ_0	U_C	U_L	τ_c (θ0)	τ_L (θ0)	ε^{∞}
311 K	5400	9400	49	150	0.20%

Step 5: Upscale Laboratory Time Scale to Real Time Scale

After fitting the expansion-time relationship, the curve initially reflected the laboratory time scale. To apply it to real-world time scale, the laboratory time scale was proportionally adjusted to the real-time scale. Since the past expansion (ϵ_1) corresponds to t_1 = 60 years, the entire laboratory time scale was recalibrated to align with actual time passed. This adjustment allowed the expansion curve to represent the material behaviour over the lifespan of the structure, from construction to the present day.

6.1.5 Results & Discussion

Figure 69 presents the expansion-time curve derived from Larive's model, incorporating results from accelerated expansion tests and laboratory samples. In this curve, the past expansion over 60 years has been back-calculated, providing a visualization of the ASR expansion progression under the specific conditions of the case study. The model was able to capture the time-dependent nature of ASR-induced expansion, reflecting both historical and projected future expansions.

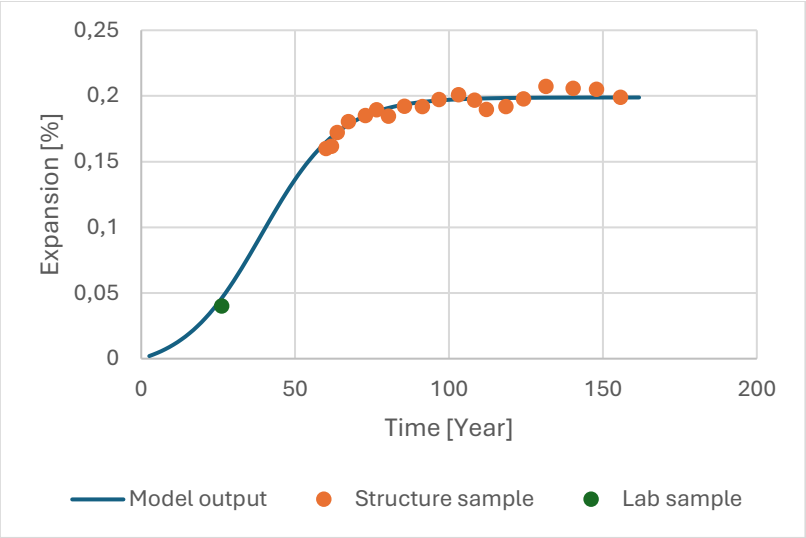

Figure 69 Expansion-time curve based on Larive's model, showing the back-calculated past expansion over 60 years and the projected future expansion, with data points from accelerated expansion tests and laboratory samples for the available case study.

To validate the back-calculated past expansion and the model's final results, a comparison was made with the study by Sanchez et al. [12], who assessed twenty concrete mixtures with varying strengths and a wide range of aggregate types. One of their mixtures, NM+Lav —comprising coarse NM R from New Mexico, USA (polymictic gravel with mixed volcanics, quartzite, chert), and fine Lav NR from Quebec, Canada (derived from granite)—closely resembles the reactive aggregates of the available case study data. The mechanical property losses reported by Sanchez et al., approximately 60% reduction in tensile strength and 40% reduction in elastic modulus, can be observed in Figure 70 (b) and (c) of their study and are comparable to the available case study data (refer to Table 11). Based on the similarity in reactive aggregate types and mechanical property losses, the ultimate expansion values were compared. The estimated ultimate expansion of the available case study data is 0.20%, while Sanchez et al. reported approximately 0.23%, as shown in Figure 70 (a). This close agreement supports the validity of the back-calculated past expansion and the overall model predictions.

Nevertheless, the reliance on literature-data from single source, which is Esposito et al.'s [27], introduces limitations. While the chosen literature-based data provides a useful reference, its generality—spanning diverse material characteristics, exposure conditions, and testing setups—may not fully account for the specific context of the case study. To enhance the generalizability and accuracy of the method, it is recommended to involve a larger set of targeted literature-based data that closely aligns with the material and environmental characteristics of the case study. Additionally, incorporating factors such as environmental conditions and leaching into Larive's model, as in [76]–[79], where data is available, would further refine the expansion predictions and better represent the progression of expansion in existing structures.

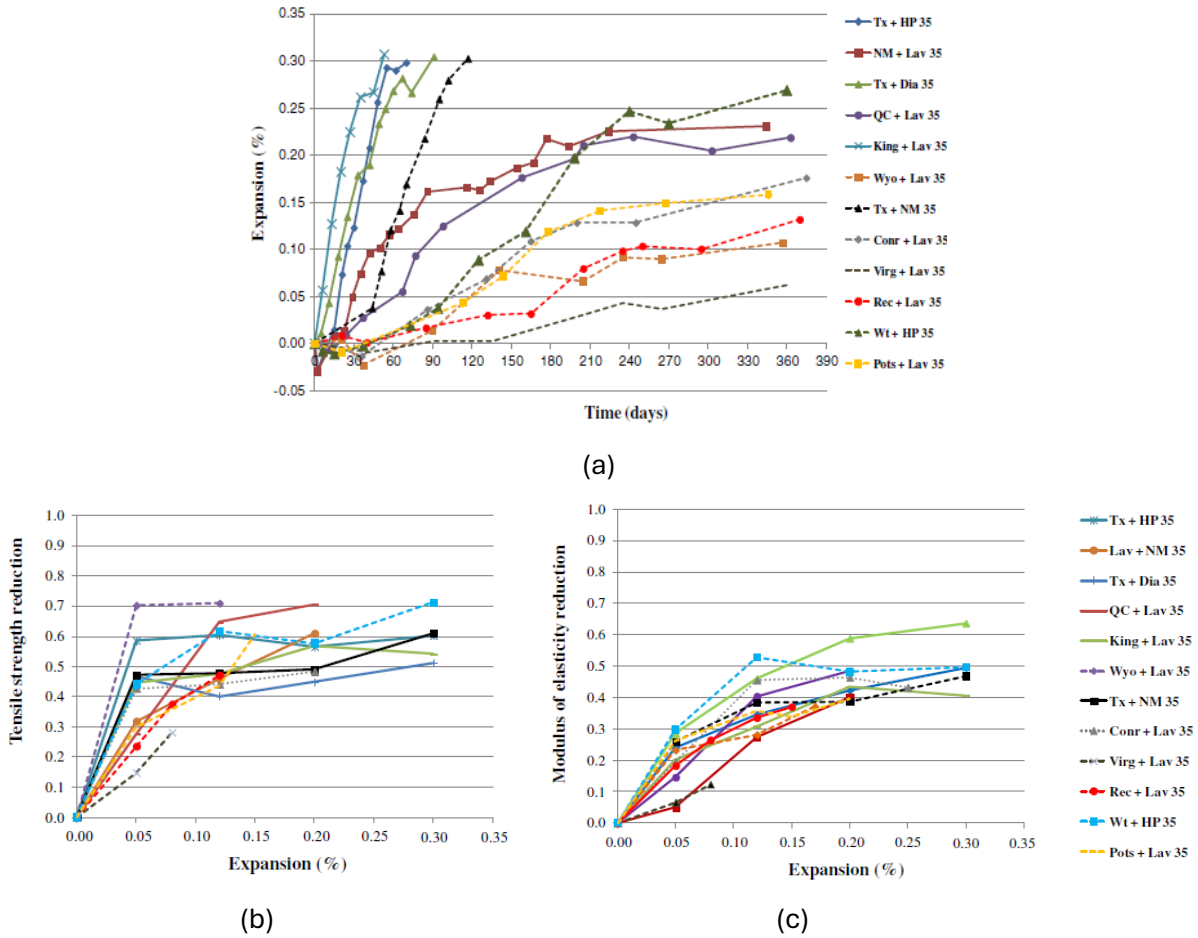

Figure 70 Results from Sanchez et al. [12]: (a) AAR kinetics (expansion vs. time), (b) Tensile strength reduction, and (c) Elastic modulus reduction.

6.2 Esposito's Expansion-Dependent Material Deterioration Model

6.2.1 Esposito's equation

The Expansion-Material Degradation Correlation is established using Esposito's model. This model, based on statistical analysis of laboratory test results and literature data —a revised version of the degradation law proposed by Saouma et al. [11] — to describe the degradation of mechanical properties such as tensile strength and elastic modulus as functions of ASR-induced expansion.

The model expresses the normalized mechanical property (βP) as a function of expansion (ε) using the following equation, which represents an inverse sigmoid function [80]:

$$\beta_P = \frac{P}{P^{\text{ref}}} = \beta_0 - (\beta_0 - \beta_\infty)\frac{1 - \exp\left(-\frac{\varepsilon}{\varepsilon_c}\right)}{1 + \exp\left(-\frac{\varepsilon - \varepsilon_l}{\varepsilon_c}\right)} \tag{13}$$

Where:

- P and P_{ref} represent the current and reference values of the chosen property, respectively.
- β_0 and β_∞ denote the normalized property values at zero expansion and at the asymptotic expansion, respectively.
- ϵ represents the expansion.
- ϵ_l and ϵ_c are the latency and characteristic expansion values, respectively. The latency expansion (ϵ_l) defines the delay before a relevant degradation of the mechanical property is observed. The lower the latency expansion, the earlier the degradation is observed. The characteristic expansion (ϵ_c) contributes to the degradation rate, defined as the average decrease between ϵ_l and $\epsilon_l+2\epsilon_c$.

6.2.2 Parameters Determination

- **Latency Expansion (ϵ_l) and Characteristic Expansion (ϵ_c)**: Initially assumed based on the values proposed by Esposito et al. [27] .
- **Normalized Property Values (β0 and β∞):** Determined from the available case study data, reflecting the initial and ultimate degradation states of the mechanical properties.

6.2.3 Proposed Process

The following process outlines the steps to determine the expansion- material Properties correlation using Esposito's model, Larive's model and available case study data. The results of this process are presented in Section 6.2.4**.**

Input Requirements

- Original material properties values, Table 8
- The residual reduction in the mechanical properties, Table 9
- The ultimate reduction in the mechanical properties, Table 11
- The ultimate expansion, Equation (9)

Step 1: Plot Initial Expansion-Material Degradation Curve

The initial curve is plotted using the proposed initial values for ϵc, ϵl, β0 and β∞ (see Table 13). This provides a baseline to visualize how the mechanical properties are expected to degrade as a function of ASR-induced expansion, based on default or literature-derived parameters.

Table 13 initial values of Esposito's model

	β0	β∞	ϵ_c	ϵ_l
Tensile strength ft	1.01	0.6	0.11	0.35
Elastic modulus E	1.06	0.19	0.37	1.13E-09

Step 2: Adjust Normalized Property Parameters

β0 and β∞ are adjusted to fit the observed reductions in mechanical properties:

- β0 is set to 1, representing the normalized initial property.
- β∞ is determined based on the ultimate reduction in the property.

Step 3: Fit Expansion Parameters

ϵ_c and ϵ_l are calibrated using the estimated ultimate expansion (ϵ^{∞}) in Section 6.1.5. Further, these parameters are adjusted to ensure the model reflects both the residual and ultimate reductions in mechanical properties.

Step 4: Finalize Model Parameters

the final set of parameters for the Expansion-Material Degradation Correlation, as presented in Table 14.

Table 14 the final set of parameters for Esposito's model

	Original value	β0	β∞	εc	εl
Tensile strength ft	2.77 MPa	1	0.4	0.023	0.13
Elastic modulus E	32308 MPa	1	0.6	0.06	9.00E-02

In addition to Expansion-Material Degradation Correlation, time-based correlation can be made further by coupling the results of the two models This coupling facilitates the establishment of a time-based correlation with the reduced material properties, to assist alternative approaches while assessing the existing structures numerically.

6.2.4 Results & Discussion

Figure 71 illustrates the relationship between normalized ASR-induced expansion and the reduction of material properties—specifically tensile strength and elastic modulus—as predicted by Esposito's model. The curves highlight the deterioration of these properties as a function of expansion. As the expansion increases, both tensile strength and elastic modulus decrease, with the rate of degradation accelerating after a certain expansion threshold. The red-striped lines represent a ±10% measured reduction from structure samples extracted at t_1 (60 years) and exposed to accelerated expansion tests.

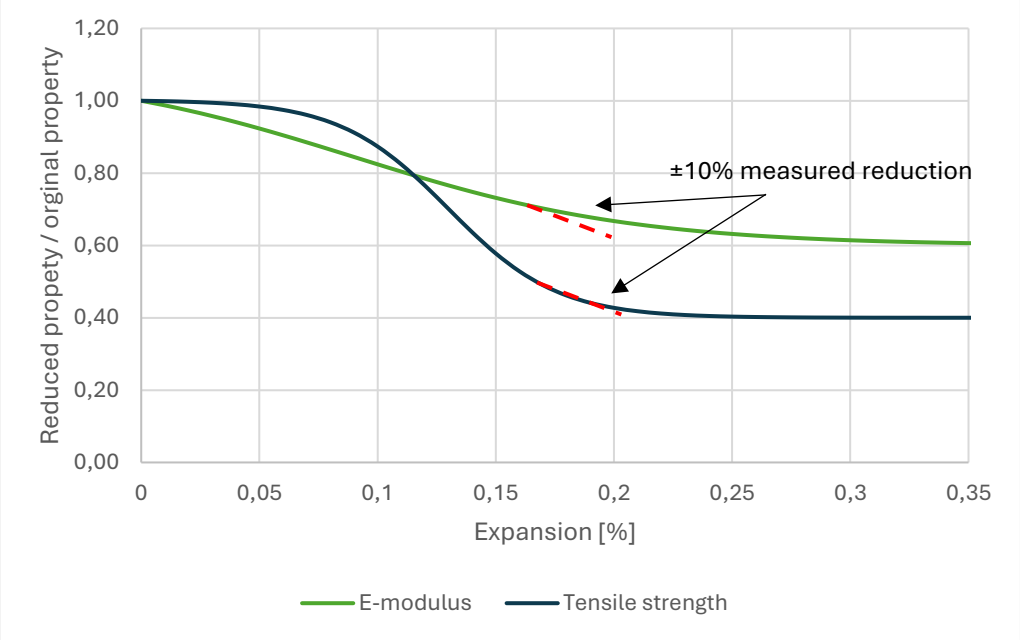

Figure 71 Relationship between ASR-induced expansion and normalized material properties deterioration (tensile strength and elastic modulus) based on Esposito's model.

The model effectively captures the nonlinear degradation behaviour observed in ASR-affected concrete. The correlation shown in Figure 71 can be integrated into the ASR-affected concrete constitutive model, as demonstrated in Section 4.3, to adapt the expansion-based tensile strength behaviour and enable the numerical model to capture strength degradation and predict potential damage. As noted by Esposito et al. [27] and illustrated in the results, stiffness and strength degrade at different rates. Furthermore, findings from the numerical model indicate a more rapid degradation of the elastic modulus, see Section 4.2.2.4, highlighting its limitations in simulating gradual stiffness reduction. These factors make it more appropriate in this research to base the reduction of material properties on tensile strength degradation for more accurate structural predictions.

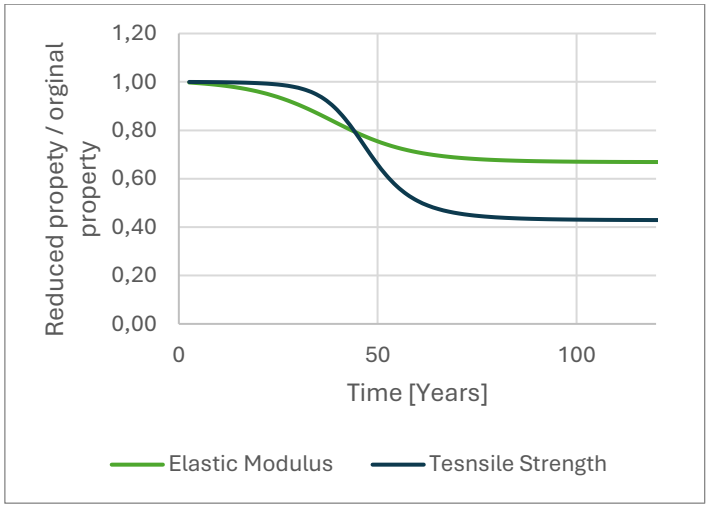

Figure 72 Normalized Time-based reduction in material properties (tensile strength and elastic modulus) due to ASR.

Figure 72 illustrate the normalized, time-based reduction in material properties resulting from the coupling of Larive's expansion prediction model and Esposito's material degradation model. The figure demonstrates that over the structure's lifespan, both tensile strength and elastic modulus diminish progressively, correlating with the expansion-time relationship established by Larive's model.

6.3 Conclusion

This chapter focused on establishing a reliable basis for forecasting ASR-induced expansion and related material degradation in concrete structures. To achieve this, two key objectives were addressed: developing a time-expansion correlation and determining how ASR-induced expansion relates to changes in tensile strength and stiffness. By integrating established phenomenological models with case study data and relevant literature, the chapter provided a structured approach to refining the input parameters for numerical simulations of long-term ASR behaviour.

Larive's model forecasted the long-term free ASR-induced expansion. The past expansion was estimated by relating observed reductions in material properties to an appropriate level of expansion. Accordingly, curve fitting was used to identify the ultimate expansion value. Despite this approach relying on literature-based data, the results showed good agreement with experiments on materials of similar characteristics. However, this approach requires further investigation, and it is recommended to involve a larger set of literature-based data oriented to materials of similar characteristics.

Further, Esposito's model related the free ASR-induced expansion to the progressive deterioration of tensile strength and elastic modulus. By using the results from Larive's model and the available case study data, Esposito's model parameters were calibrated to capture the degradation of material properties as expansion increases. This model was further integrated with Larive's time-expansion correlation, enabling long-term forecasting of both expansion and the resulting property reductions.

Building upon these findings, the estimated ultimate expansion from Larive's model can now be employed as an input to the structural model. Additionally, Larive's time-expansion relationship provides the link between the expansion increments in the structural model and the corresponding time scale. Similarly, the expansion-based tensile strength correlation derived from Esposito's model can be implemented in the tensile curve used within the numerical simulations. Together, these two phenomenological models provide a standardized solid framework for bridging the gap between structural analysis and material-level observations, setting the stage for the next chapter's demonstration of their application in a hypothetical bridge pier cap scenario.

7. Final Framework: Hypothetical Case Study

This chapter presents the final integrated framework for predicting the long-term behaviour of reinforced concrete structures affected by ASR. Previously, the individual components of this framework—a structural (numerical) model and two phenomenological material models—were developed, verified, and discussed. Here, these elements are combined into a single, coherent methodology. To demonstrate its application and capabilities, the framework is applied to a hypothetical bridge pier cap inspired by real-world ASR damage observations.

7.1 Framework Overview

The integrated framework combines the Modified Dual Mesh Method (MDMM) for structural modelling with Larive's time-dependent expansion model and Esposito's expansion-based material degradation model. As illustrated in Figure 73, the framework consists of two primary branches. The structural model branch implemented using the MDMM, detailed in 4, simulates the mechanical response of the structure under progressive ASR-induced degradation. Simultaneously, the material models branch, incorporating Larive's and Esposito's models, as described in 6, establishes the relationships between free ASR-induced expansion over time and the corresponding degradation of material properties.

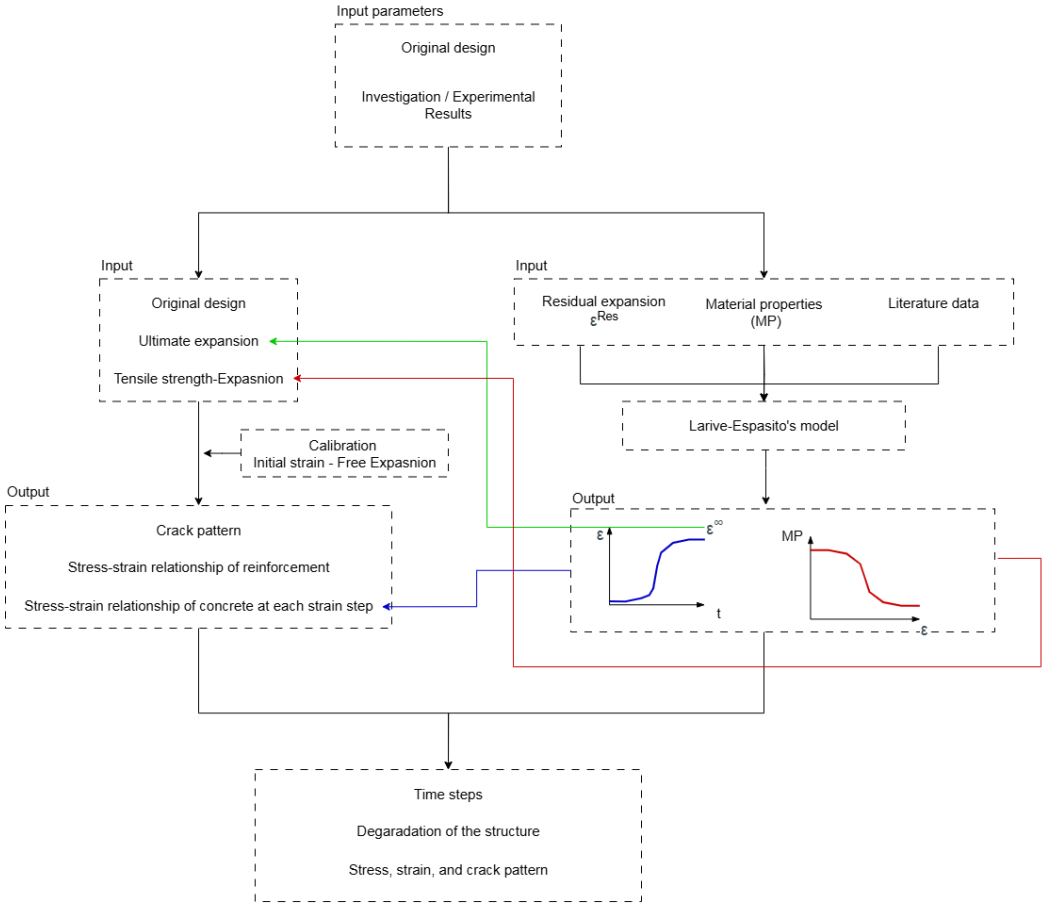

Figure 73 Framework for predicting the long-term behaviour of reinforced concrete structures affected by ASR

These branches interact in two keyways. First, the material models provide essential inputs—such as ultimate expansion and the tensile strength–expansion relationship—to the structural model.

Second, by referencing the expansion-time curve, targeted expansion levels are linked to specific time points, enabling the determination of when the structure's integrity is compromised. Within the scope of this study, the structure is considered compromised when the steel reinforcement reaches its yield point, even if it has not fully collapsed.

7.2 Hypothetical Case Study

This case study represents an existing infrastructure element of a post-tensioned bridge pier cap diagnosed with ASR. Figure 74 (a) illustrates typical ASR-induced surface cracking observed at the bottom of a pier cap, while Figure 74 (b) provides a conceptual depiction of the structure. The case study focuses on the upper part of the structure—the pier cap—while excluding the supporting pier column beneath it.

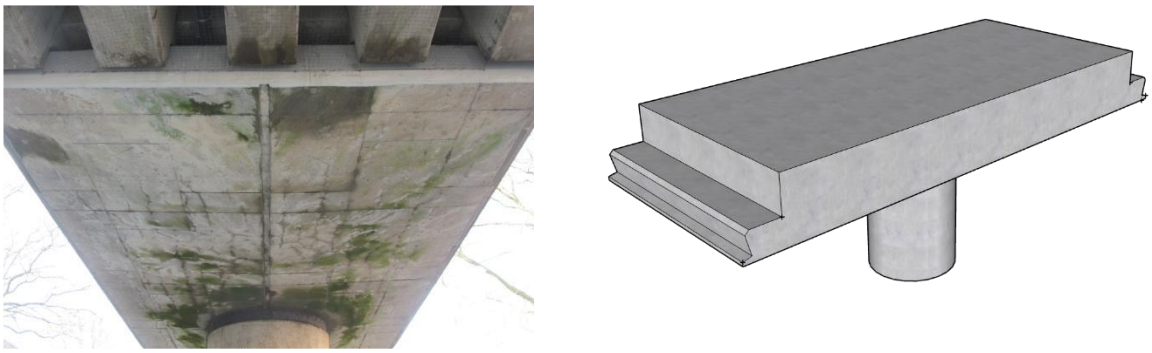

(a) (b)

Figure 74 (a) typical ASR-induced surface cracking observed on the underside of a pier cap [81]; (b) conceptual depiction of the bridge structure.

The pier cap measures 15 m in length, 6 m in width, and 1.76 m in height. It is reinforced and post-tensioned in both the longitudinal and transverse directions. In addition, the design material properties, as well as the degraded material properties and ASR expansion values relevant to this study, were presented earlier in Section 6.1.3. These parameters will be utilized to simulate the structural response and assess the impact of ASR-induced damage. Further details regarding the structure's design, reinforcement layout, material properties, and loading conditions will be provided in the subsequent Section 7.3.

7.3 Numerical Model Description

This section describes the finite element model of the pier cap used to demonstrate the proposed framework and the 3D application of the MDMM. While reflecting realistic structural settings, the model is not tied to a specific structure. Additionally, simplifications were made to reduce computational costs while preserving representativeness.

7.3.1 Structure Overview and Geometry

The pier cap is modelled as a simplified cuboid with dimensions of 15 m × 6 m × 1.76 m, as shown in Figure 75. The column support is represented as a circular support within the model. The reinforcement includes longitudinal and transverse bars, along with stirrups of 16 mm diameter spaced at 600 mm. While an initial spacing of 300 mm was considered, the 600 mm spacing was chosen to reduce model complexity and computational intensity. Additional reinforcement is provided around the column support to prevent punching failure. Curved post-tensioning cables, each with a diameter of 32 mm, are included in both longitudinal and transverse directions, with 12 cables in the longitudinal direction and 24 in the transverse direction. Figure 75 and Figure 76 illustrate the reinforcement and post-tensioning cable details.

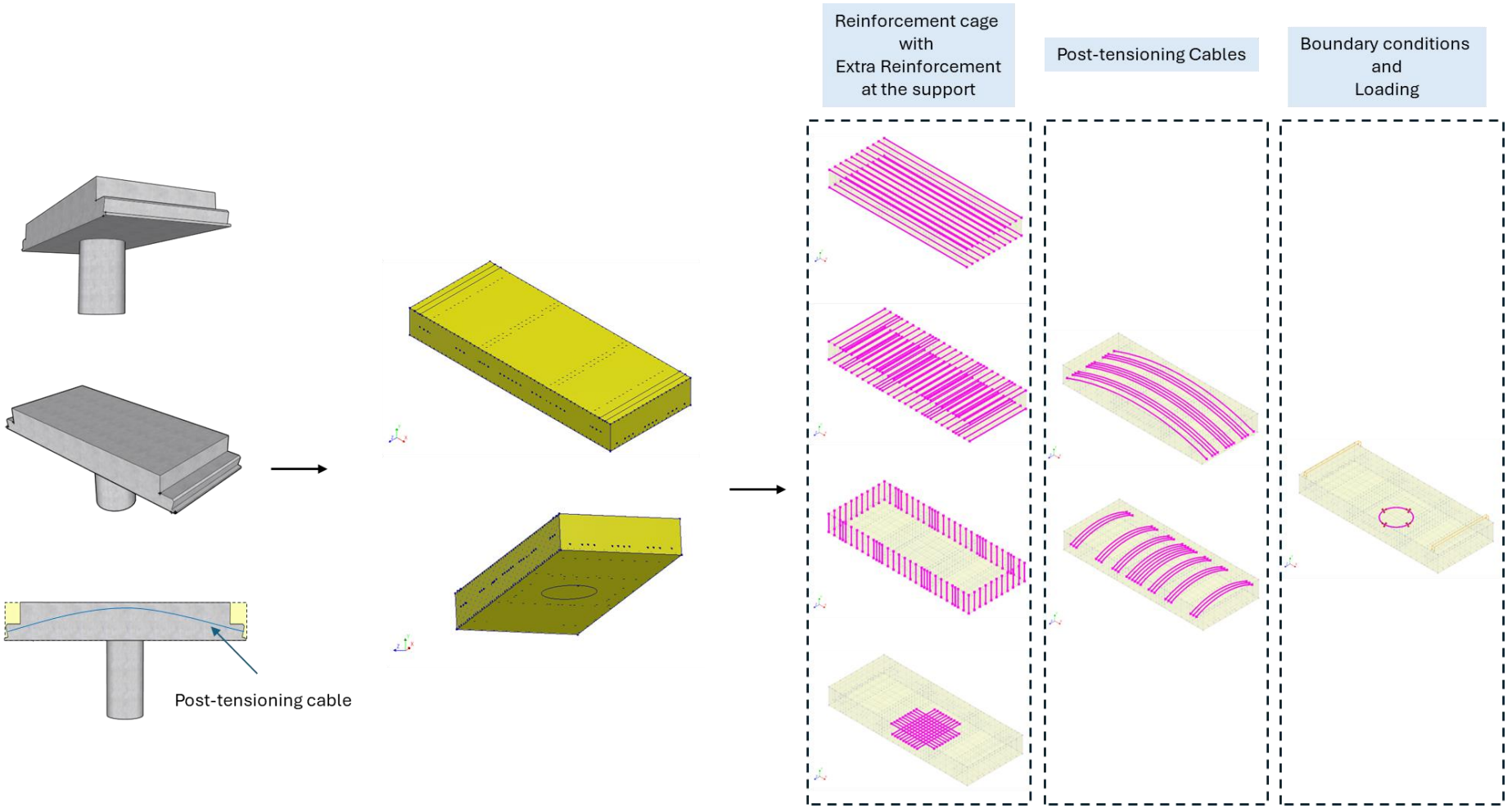

Figure 75 Simplified pier cap FEM model with its components

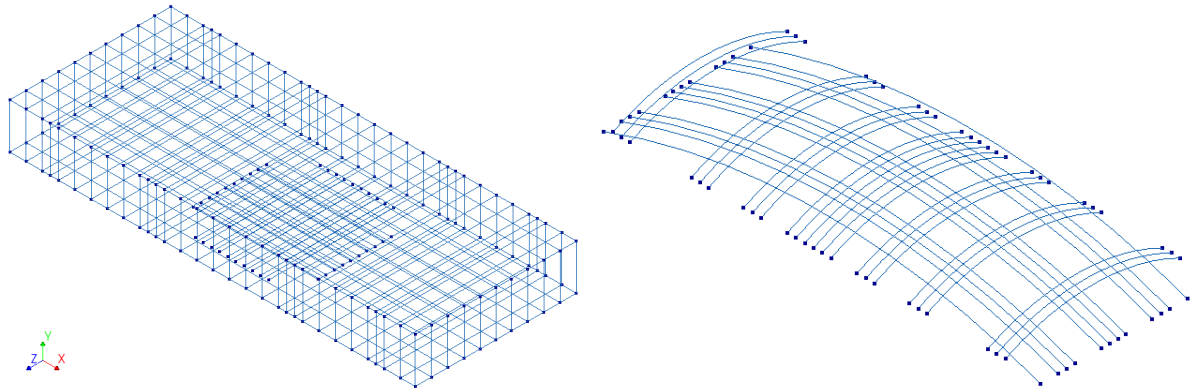

(a) (b)

Figure 76 (a) Reinforcement Cage; (b) post-tensioning cables

7.3.2 Integration of Material Models

In Chapter 6, expansion-time and expansion-material degradation correlations were established using the available case study data. These correlations are now integrated into the current analysis framework:

- **Expansion-Material Degradation Correlation:** Figure 77 (a) provides the expansion-based tensile curve. This curve was calibrated to produce a multi-linear model, as shown in Figure 78, which is implemented as the tensile curve for the concrete material model.
- **Expansion-Time Correlation:** Figure 77 (b) presents the time-based expansion curve. The ultimate expansion from this curve is set as the targeted maximum free ASR-expansion in the simulation. Expansion increments applied through the shadow mesh can be indirectly linked to time using the curve in Figure 77 (b).

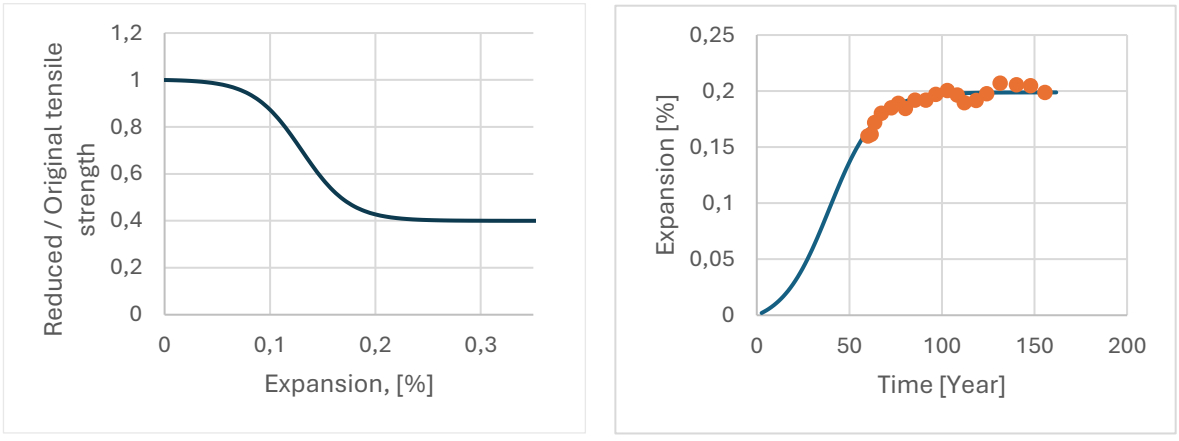

(a) (b)

Figure 77 (a) Expansion-based tensile strength curve for ASR-affected concrete; (b) Time-based expansion curve

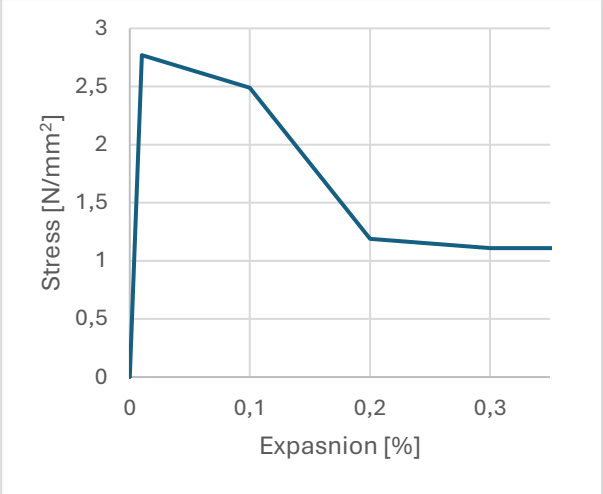

Figure 78 multi-linear tensile strength-expansion model

7.3.3 Element Type and Discretization

The pier cap is modelled using TE12L elements, four-node, three-sided isoparametric solid tetrahedrons, Figure 79, with a mesh size of 400 mm. This element type and mesh size were selected to minimize the risk of analysis failure due to irregular element shapes or excessively small angles.

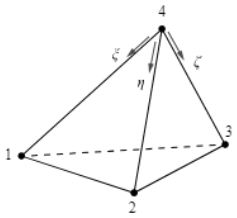

Figure 79 TE12L [73]

The reinforcement bars are fully embedded within the concrete elements, assuming a perfect bond. For simplicity, the post-tensioning cables are modelled as embedded reinforcement with no bond to the surrounding concrete.

7.3.4 Material Properties

The material properties for concrete, reinforcement, and post-tensioning cables used in the finite element model are summarized in Table 15**.**

Table 15 Design Material Properties of Concrete

Material	**Parameter**	**Input**
Concrete	Young's modulus (E_c)	32308 MPa
	Poisson's ratio (v)	0.2
	Tensile strength (f_{tm})	2.77 MPa
	Compressive strength (f_{cm})	36 MPa
	Fracture energy in compression (G_c)	32.7 N/mm
	Mass density (ρ)	2.4E-9 T/mm^3
Dual Mesh (DM)	Young's modulus (E_{DM})	2% E_C MPa
	Poisson's ratio (v)	0

	Mass density (ρ)	0 T/mm^3
Reinforcement	Young's modulus (E)	200000 MPa
	Yielding strength (f_{ym})	440 MPa
	Ultimate strength (f_{um})	475 MPa
	Ultimate strain (ε_{su})	0.05
Post-tensioning Cables	Young's modulus (E)	200000 MPa
	Yielding strength (f_{ym})	1674 MPa
	Ultimate strength (f_{um})	1770 MPa
	Ultimate strain (ε_{su})	0.035

7.3.5 Material Models

The material models and their specifications for concrete, shadow mesh, reinforcement, and tendons are provided in Table 16.

Table 16 Material Models Specification

	Specifications	**Input data**
Concrete	Class	Concrete and masonry
	Material Model	Total strain-based crack model
	Crack Bandwidth	Element size
	Crack Orientation	Rotating
	Tensile curve	Multi-linear[2]
	Crack bandwidth specification	Rots
	Poisson's ratio reduction	No reduction
	Compressive Behaviour	Parabolic
	Reduction model	Vecchio and Colline 1993
	Lower bound reduction curve	0.6
Shadow Mesh	Class	Composites and rubber
	Material Model	Linear elastic isotropic
Reinforcement	Class	Steel
	Material Model	Von Mises plasticity
	Hardening Hypothesis	Strain hardening
	Hardening Type	Isotropic hardening
Tendon	Class	Steel
	Material Model	Von Mises plasticity
	Hardening Hypothesis	Strain hardening
	Hardening Type	Isotropic hardening
	Bonding	No

7.3.6 Boundary Conditions

Fixed translations in all directions were applied to the circular support located at the centre of the bottom face of the pier cap. This boundary condition represents the fixed connection between the column and the pier cap, as illustrated in Figure 80.

[2] See Figure 78 **in section 7.3.2**, estimated from the expansion-based tensile strength reduction correlation of the case study

7.3.7 Loads

Several types of loads were applied to the pier cap in the analysis:

1. **Self-Weight**: The self-weight of the pier cap was automatically generated by the software, using a default gravitational acceleration of g=9.81 m/s^2.
2. **Design Load**: This load combines permanent loads (e.g., from girders) and variable loads (e.g., traffic on the bridge). It was applied as a surface load distributed over the strip area across the pier cap width with dimensions 6000 mm×400 mm^2, as shown in Figure 80. The magnitude of the load was initially estimated based on realistic values and subsequently adjusted to ensure no cracking occurred at the top middle section of the pier cap when self-weight, post-tensioning, and design load were applied. The resulting design load was set at 1 N/mm^2.
3. **Post-Tensioning Load**: Post-tensioning forces were applied at the anchor ends of the cables without accounting for losses. The magnitudes were set at 600 kN for longitudinal cables and 431 kN for transverse cables.
4. **Expansion Load**: Modelled as incremental expansion, where a prescribed strain (initial strain) is applied to the shadow mesh, resulting in corresponding expansion on the structural mesh. A calibration step is required to determine the initial strain increment that corresponds to the targeted free expansion increment (see subsequent Section 7.3.8 for details).

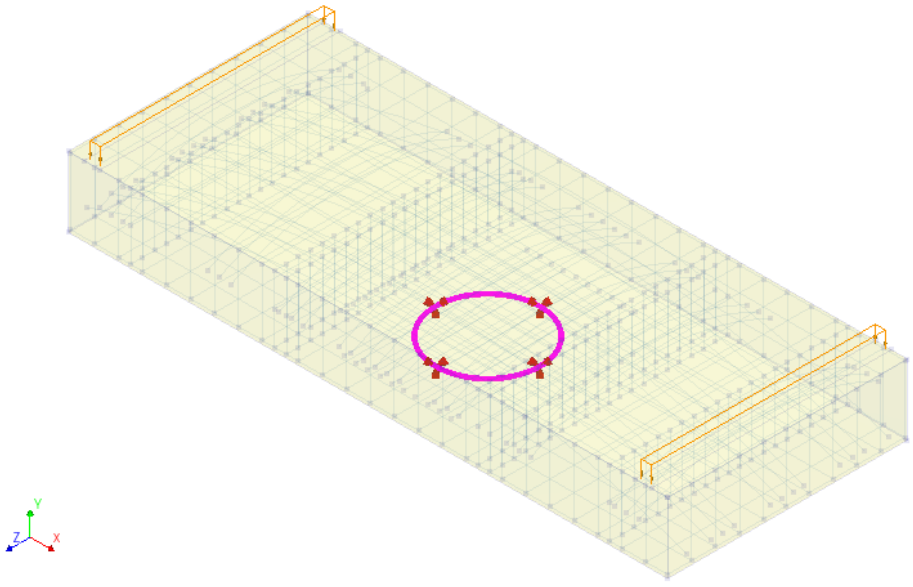

Figure 80 Loading and Boundary conditions of the pier cap

7.3.8 Calibration of Free Expansion

Calibration analysis was performed on a plain concrete model to determine the initial strain values required to achieve the desired free expansion on the structural mesh. Figure 81 shows the relationship, where the orange striped line represents the strain on the shadow mesh, and the blue line represents the resulting free expansion on the structural mesh.

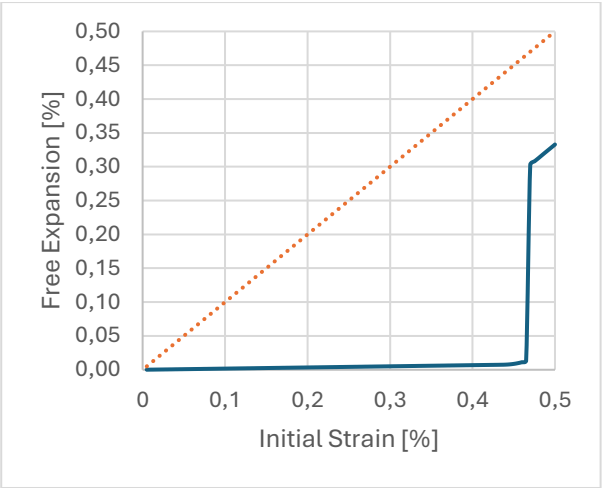

Figure 81 Calibration of Initial Strain and Corresponding Free Expansion

7.3.9 Analysis Procedure

Phased analysis is employed to manage the sequential application and interaction of various loads and the activation/deactivation of the shadow mesh.

1. **Phase I:** The self-weight of the structure is applied, followed by the post-tensioning forces.
2. **Phase II:** The design load is introduced as a surface load distributed over the strip area across the pier cap width.
3. **Phase III:** The shadow mesh is activated, and expansion is incrementally applied through prescribed initial strain on the shadow mesh.

Two iteration methods are utilized during the analysis: the Full Newton-Raphson method for Phases I and II, and the Secant method for Phase III, see Table 17. This combination ensures stability and computational efficiency across all phases of the simulation.

Table 17 the characteristics of the incremental-iterative solution method

Phase	*Iterative Scheme*	*Convergence norm*	*simultaneously satisfy*	*Tolerance*	*No convergence*	*Step size*	*Max iteration*
I and II	Full Newton-Raphson	Energy AND Out-of-balance force	Both	0.0001 (energy) 0.01 (Out-of-balance force)	Continue	Both 0.01(100)	300
III	Secant (Quasi-Newton)	Energy AND Out-of-balance force	Both	0.0001 (energy) 0.01 (Out-of-balance force)	Continue	Both 0.01(100)	400

7.4 Results and Discussion

Figure 82 illustrates the principal stress distribution in the pier cap due to self-weight, post-tensioning, and design load, prior to the onset of ASR-induced expansion. The highest stresses are concentrated at the top middle section of the plate near the supports, corresponding to the zone of maximum bending moment. However, these stresses remain below the tensile strength of the concrete, and no cracking is observed.

Once ASR expansion is introduced, initial cracks develop at the top surface where tensile stresses are highest, as shown in Figure 83. As the expansion progresses, these cracks propagate, following stress concentration paths, eventually forming a widespread network of cracks across the plate, as depicted in Figure 84. The crack propagation ultimately leads to full coverage of the plate, as illustrated in Figure 85.

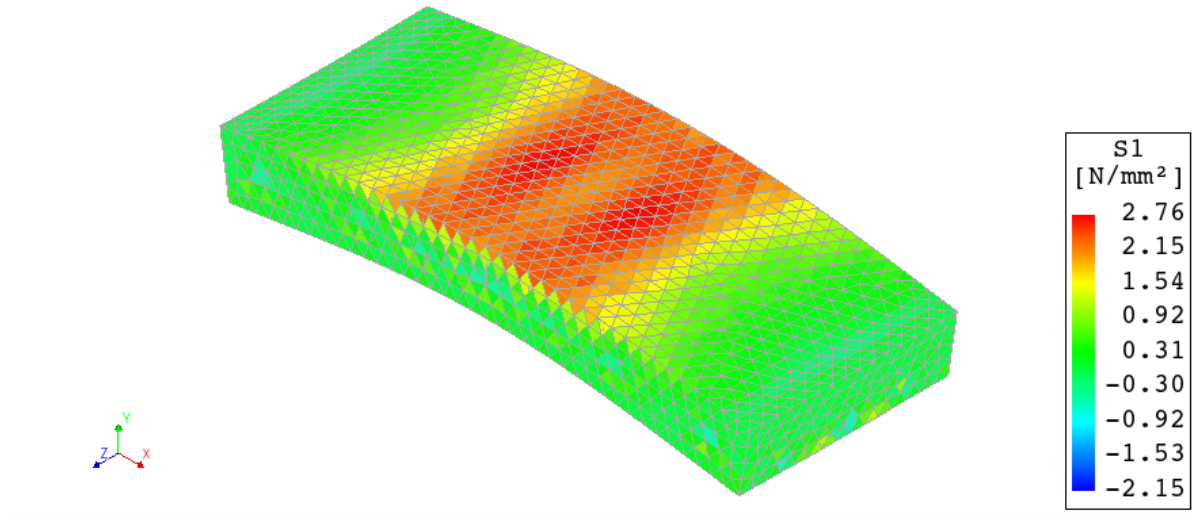

Figure 82 Contour plot of the principal stress distribution in the Pier Cap Before ASR-Induced Expansion.

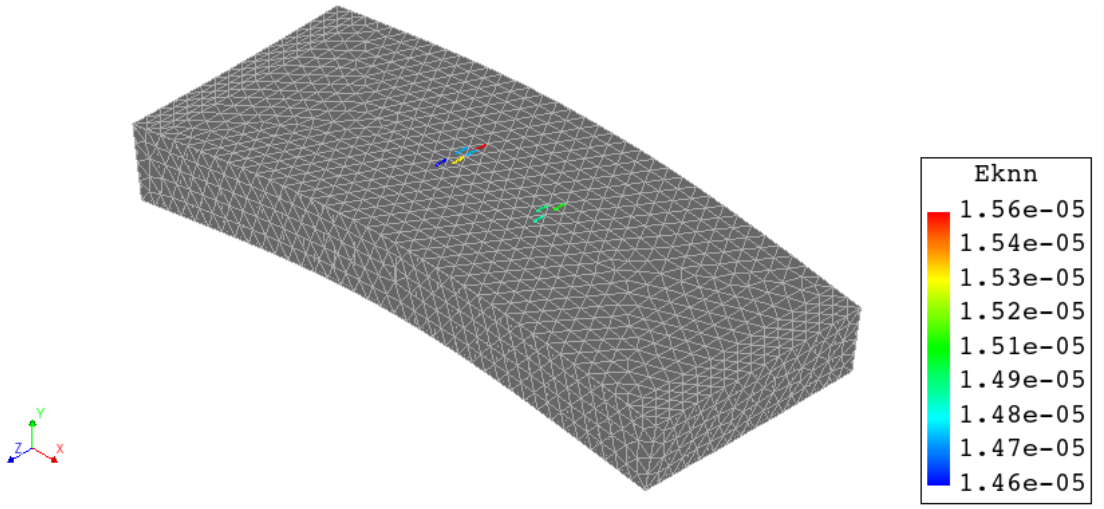

Figure 83 Initial Cracks at the Top Surface of the Pier Cap During Early Stages of ASR Expansion, where Eknn is crack strain.

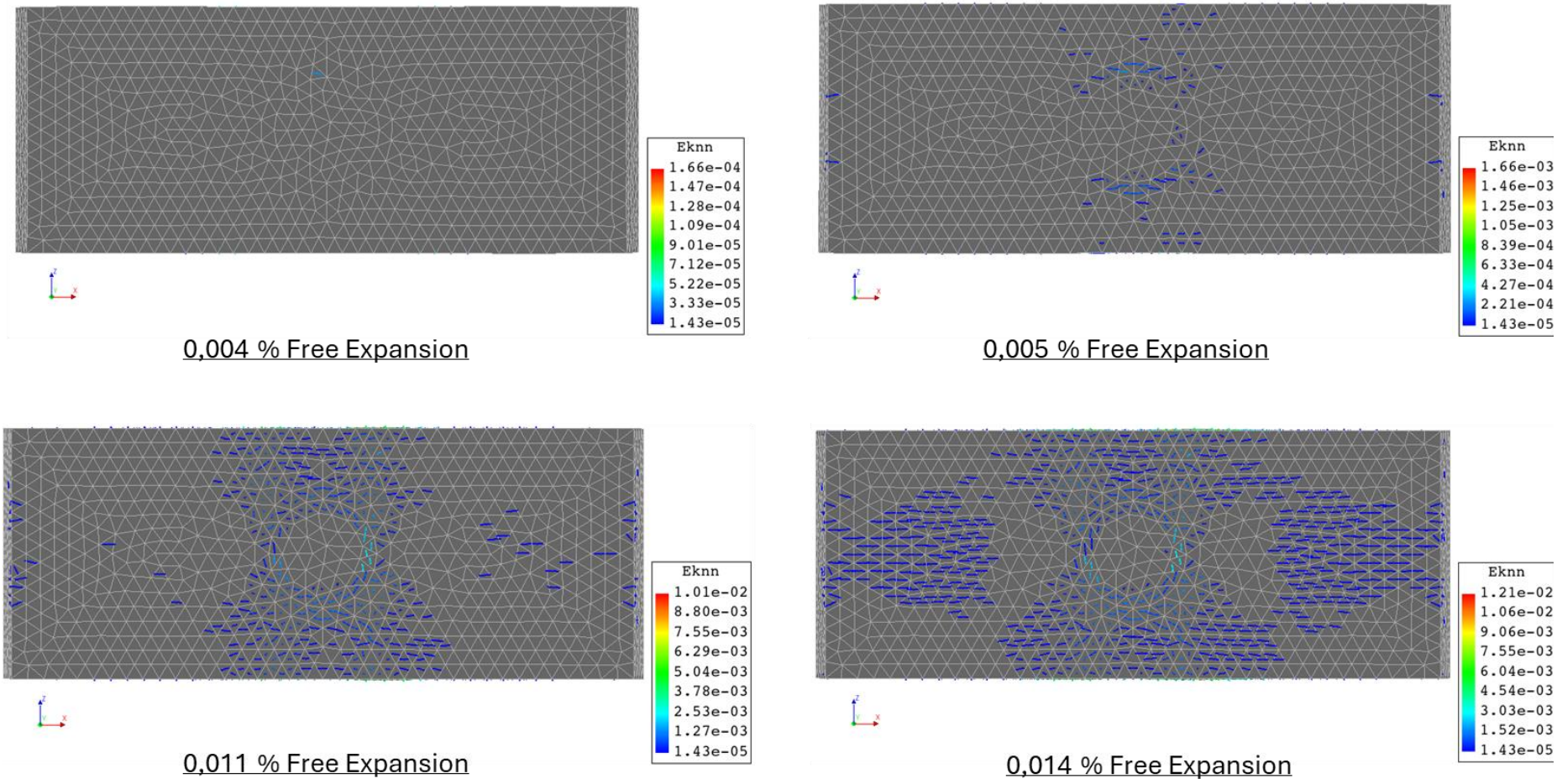

Figure 84 Evolution of Crack Patterns at the Bottom Surface of the Pier Cap with Increasing ASR Expansion.

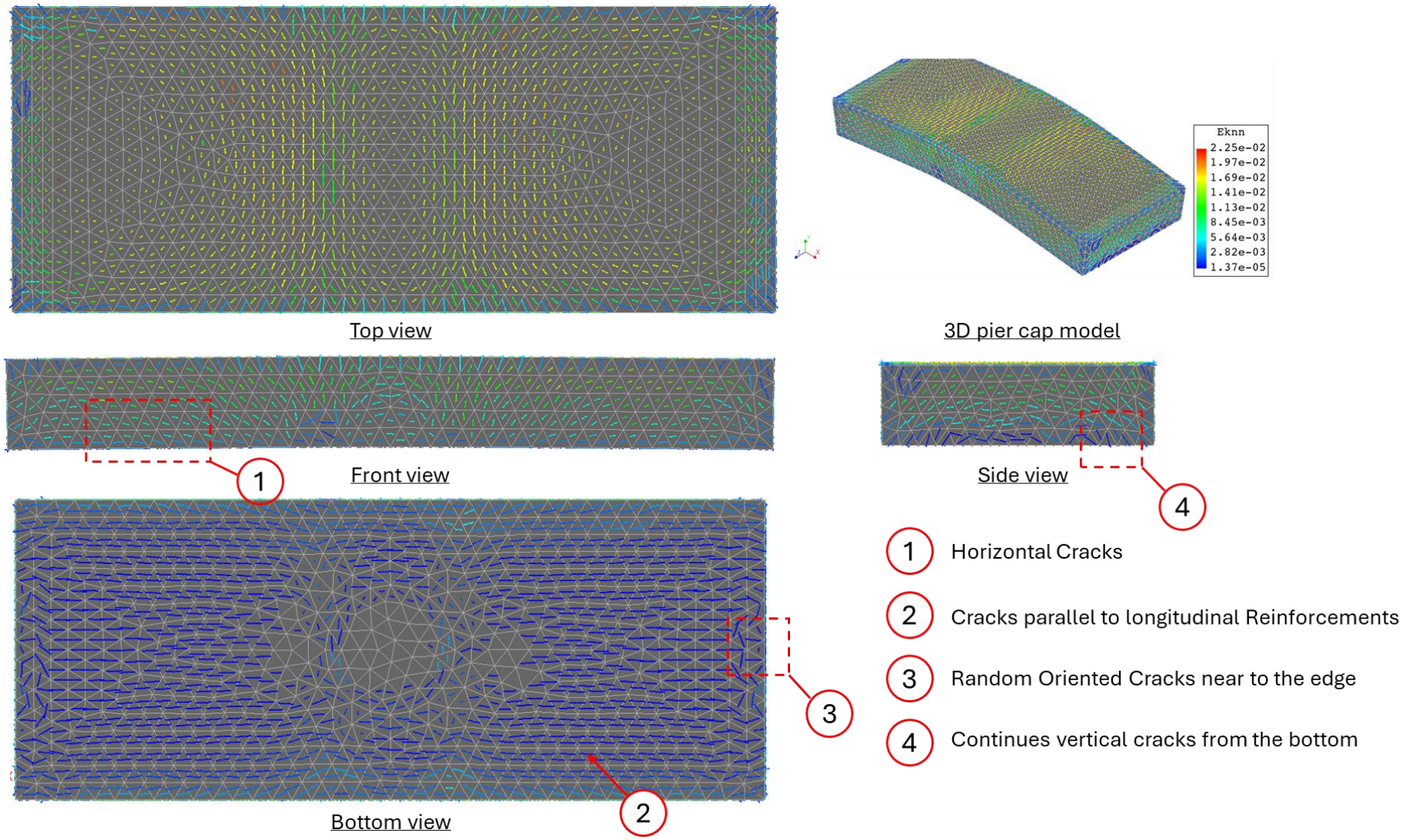

Figure 85 Final Crack Patterns and Orientation at 0.2% Ultimate ASR Expansion in the Pier Cap.

As the expansion reaches 0.2%, representing the ultimate expansion level, the crack patterns become well-defined, as shown in Figure 85. The largest cracks appear at the top, where bending stresses are greatest, while the bottom exhibits comparatively finer cracks. The model results indicate that crack orientation differs between the top and bottom surfaces, reflecting the combined effects of load-induced stresses, prestressing, and the stress- and confinement-dependent nature of expansion.

From the front view, the cracks are predominantly horizontal and concentrated between supports, closely following the principal stress paths while aligning with regions of reinforcement and confinement. At the bottom, cracks exhibit a more random orientation near the edges but tend to align parallel to the longitudinal reinforcement in the central regions. From the side view, cracks from the bottom continue upward as vertical cracks at the edges but transition to horizontal orientation at the mid-height of the plate's short side. Here, the horizontal crack pattern is less pronounced compared to the front view, likely due to geometric differences and their influence on stresses and confinement.

The crack patterns observed in the model align well with real-world observations and findings in the literature, further validating the simulation approach. Zahedi et al. [82] observed that ASR-induced cracks in confined concrete elements propagate parallel to the longitudinal reinforcement due to the directional restraint provided by steel bars, which transfer damage to the surrounding concrete. Similarly, Barbosa et al. [83] reported that cracks in slab bridges align with the reinforcement in both longitudinal and transverse directions, reflecting the direction of greatest restraint, as shown in *Figure* 86. Additionally, ISE [17], summarizing findings from various studies, noted that ASR-induced cracks tend to follow the path of least resistance, typically developing parallel to the steel reinforcement.

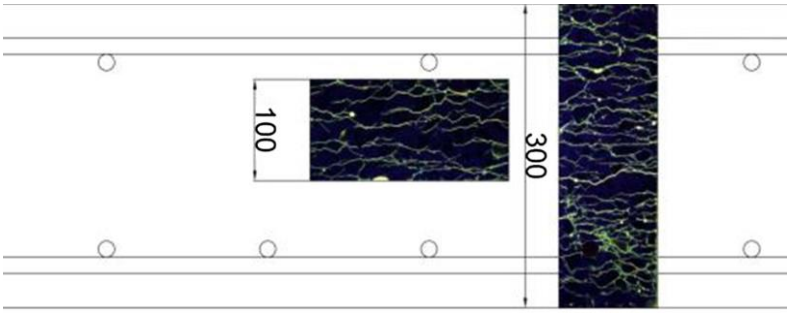

Figure 86 Horizontal ASR-induced crack shown in UV-light image of ASR cracks in a cross-section of a slab bridge [82].

Building on this, the model crack patterns are further compared with those observed in a similar ASR-affected structure, as shown in Figure 87. Figure 87 (a) presents the model output for the crack pattern on the bottom surface of the plate, while Figure 87 (b) illustrates the bottom surface of a real-world structure diagnosed with ASR. The observed structure, Figure 87 (b), exhibits primary cracks along with secondary cracking and branching. These secondary cracks connecting to the primary ones, reflecting a heterogeneous material response. In contrast, the model output in Figure 87 (a) primarily captures the primary crack pattern.

Despite the absence of secondary cracking in the model, focusing on the primary cracks reveals notable similarities with the observed structure. In both Figure 87 (a) and (b), the main cracks oriented parallel to the longitudinal reinforcement, indicating higher constraints in this direction. Furthermore, few or no primary cracks are observed near the supports in the observed structure, mirroring the model's results where additional reinforcement provides effective confinement. These comparisons, alongside the alignment with literature, highlight the framework's ability to replicate the progression of ASR-induced cracking behaviours as expansion levels develop, closely mirroring those observed in real-world scenarios.

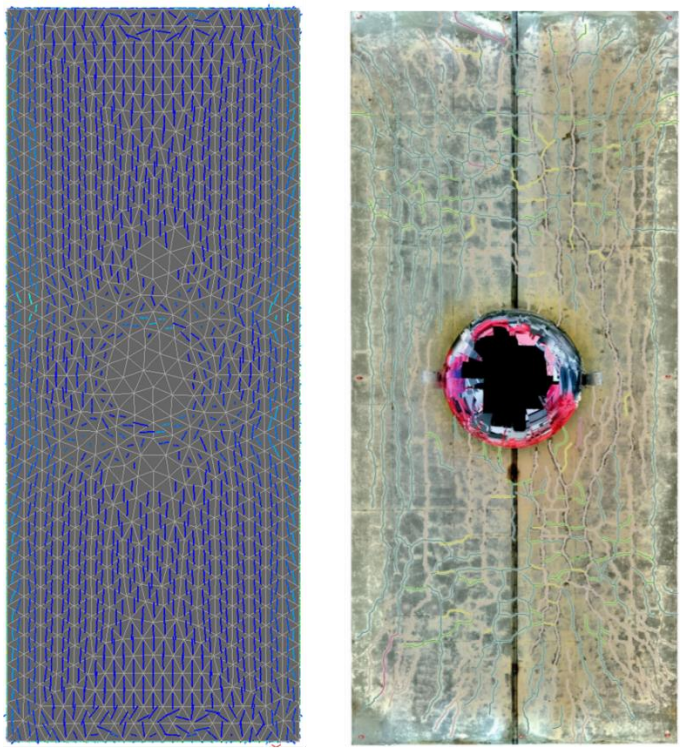

Figure 87 comparison between the crack pattern of bottom surface of the model and similar structure diagnosed with ASR (a) Model output at ≈ 0.16% free ASR-induced expansion; (b) similar ASR-affected structure [81] .

The analysis further indicates that at an ASR-induced expansion level of approximately 0.1%, the pier cap model experiences its first instance of reinforcement yielding. Figure 88 illustrates the crack patterns, orientations, and corresponding stress contour plot of the longitudinal reinforcement at this expansion threshold, highlighting that yielding initiates in the top longitudinal bars at the mid-span of the plate, directly above the column. By correlating this expansion level with the expansion-time curve shown in Figure 77 (b), it becomes possible to connect the onset of yielding to a specific timeframe, providing insights into when critical structural behaviours might emerge.

In the context of potential long-term monitoring, these findings underscore the top middle region of the pier cap—where the bending moment is greatest—as the most critical zone for early detection of reinforcement yielding, suggesting that placing strain sensors in this location could offer valuable indicators of initial structural distress. In addition, the model produces displacement outputs that could serve as an alternative approach for structural monitoring. However, it was not possible to verify these predictions due to a lack of corresponding field or experimental data, highlighting a potential area for future research.

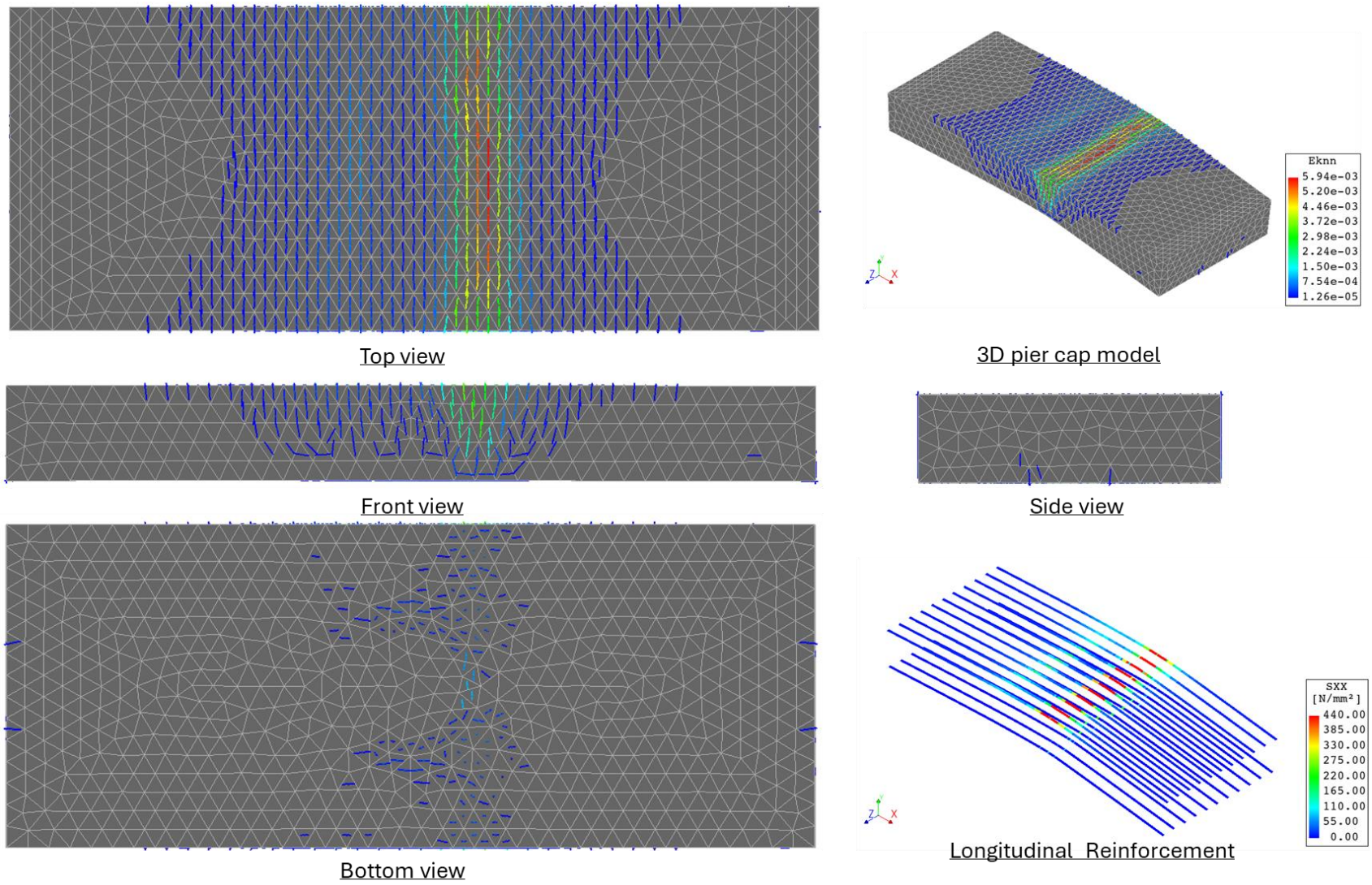

Figure 88 Crack Patterns and Orientation at 0.1% ASR Expansion when the First Reinforcement Yielding in the Pier Cap.

8. Conclusion & Recommendation

This thesis aimed to model and evaluate the structural behaviour of reinforced concrete structures affected by Alkali-Silica Reaction (ASR) over time. The research developed a modelling framework that incorporates numerical simulations and phenomenological models, offering a practical tool for assessing ASR-induced structural damage and its progression. The key conclusions are as follows:

1. The MDMM was established as an adaptable modelling tool for simulating ASR effects. Enhancements to the original Dual Mesh Method (DMM) included the introduction of an adapted tensile curve and phased analysis, enabling realistic representation of stress generation, crack propagation, and material degradation under ASR-induced expansion. The model effectively captured anisotropic expansion behaviour influenced by structural reinforcement.
2. Validation of the MDMM using benchmark tests demonstrated its ability to predict structural behaviour under static and gradual ASR-induced expansion. The results aligned well with experimental observations, particularly in capturing crack patterns and load-displacement responses. Comparisons with the Reduced Material Properties Method (RMPM) highlighted the MDMM's enhanced capability in simulating internal expansion forces and realistic structural degradation.
3. Larive's time-expansion model and Esposito's expansion-material degradation model were successfully integrated into the framework, providing a reliable link between time-dependent expansion, material property reduction, and structural analysis. This integration addressed the challenge of incorporating time-based predictions into numerical models, bridging material-level observations and structural behaviour.
4. The framework's application to a hypothetical bridge pier cap showcased its ability to replicate real-world ASR damage scenarios. Crack propagation trends, reinforcement yielding, and stress redistribution under combined ASR and mechanical loading were effectively simulated, validating the framework's practical utility.
5. While the MDMM captured tensile strength degradation accurately, it exhibited limitations in simulating the gradual reduction of elastic modulus. Additionally, computational efficiency issues due to reduced reinforcement levels highlight the need for further refinement. In addition, the effect of the reduction in compressive strength was not considered.
6. The developed framework provides a practical methodology for assessing the long-term performance of ASR-affected reinforced concrete structures. It offers insights into damage progression, aiding structural assessment, maintenance planning, and life-cycle management.

To advance the developed framework and enhance its applicability, the following recommendations are proposed:

1. Validate the framework using comprehensive case studies with detailed experimental data, allowing for reflection on limitations and identification of areas requiring further improvement.
2. Investigate the framework's performance on structures with varying geometries (shear failure) and confinement configurations to ensure its versatility across different structural scenarios.

3. Develop a direct correlation between tensile and compressive strength degradation to refine the material property model and improve its representation of ASR-affected concrete.
4. Introduce probabilistic models to account for the material heterogeneity in shadow mesh properties, enabling the investigation of uncertainties associated with ASR effects on non-uniform materials.
5. Expand the framework to include other deterioration mechanisms, such as carbonation and chloride ingress, for a more comprehensive structural assessment of concrete infrastructure.
6. Address the rapid decline of elastic modulus in the current model by exploring alternative calibration methods or integrating more accurate degradation functions.
7. Consider linking the reduction of tensile strength with the compressive strength, which can indirectly result in a realistic reduction of the elastic modulus and more accurate structural response.

By addressing these recommendations, the framework can be further refined to provide a reliable and practical tool for assessing and managing ASR-affected reinforced concrete structures in real-world scenarios.

References

[1] T. E. Stanton, 'Expansion of Concrete through Reaction between Cement and Aggregate', *Transactions of the American Society of Civil Engineers*, vol. 107, no. 1, pp. 54–84, Jan. 1942, doi: 10.1061/TACEAT.0005540.

[2] V. E. Saouma, *Diagnosis & Prognosis of AAR Affected Structures State-of-the-Art Report of the RILEM Technical Committee 259-ISR*, vol. 31. in RILEM State-of-the-Art Reports, vol. 31. Cham: Springer International Publishing, 2021. doi: 10.1007/978-3-030-44014-5.

[3] B. Godart, M. de Rooij, and J. G. M. Wood, *Guide to Diagnosis and Appraisal of AAR Damage to Concrete in Structures*, vol. 12. in RILEM State-of-the-Art Reports, vol. 12. Dordrecht: Springer, 2013. doi: 10.1007/978-94-007-6567-2.

[4] F. Rajabipour, E. Giannini, C. Dunant, J. H. Ideker, and M. D. A. Thomas, 'Alkali–silica reaction: Current understanding of the reaction mechanisms and the knowledge gaps', *Cem Concr Res*, vol. 76, pp. 130–146, Oct. 2015, doi: 10.1016/J.CEMCONRES.2015.05.024.

[5] R. B. Figueira *et al.*, 'Alkali-silica reaction in concrete: Mechanisms, mitigation and test methods', *Constr Build Mater*, vol. 222, pp. 903–931, Oct. 2019, doi: 10.1016/J.CONBUILDMAT.2019.07.230.

[6] R. Esposito, C. Anaç, M. A. N. Hendriks, and O. Çopuroğlu, 'Influence of the Alkali-Silica Reaction on the Mechanical Degradation of Concrete', *Journal of Materials in Civil Engineering*, vol. 28, no. 6, p. 04016007, Jan. 2016, doi: 10.1061/(ASCE)MT.1943-5533.0001486.

[7] R. Esposito and M. A. N. Hendriks, 'Literature review of modelling approaches for ASR in concrete: a new perspective', *European Journal of Environmental and Civil Engineering*, vol. 23, no. 11, pp. 1311–1331, 2017, doi: 10.1080/19648189.2017.1347068.

[8] Y. Takahashi *et al.*, 'A Review of Numerical Models for the Performance Assessment of Concrete Structures Affected by Alkali-Silica Reaction', *Journal of Advanced Concrete Technology*, vol. 21, no. 8, pp. 655–679, Aug. 2023, doi: 10.3151/JACT.21.655.

[9] S. Sørgaard Kongshaug, T. Kanstad Professor, M. Hendriks Professor, A. Professor, ntnuno Mahdi Kioumarsi Associate Professor, and G. Markeset Professor, 'Challenges related to structural modelling and assessment of concrete structures affected by alkali-silica reactions', *175-178*, 2017, Accessed: Oct. 17, 2024. [Online]. Available: https://ntnuopen.ntnu.no/ntnu-xmlui/handle/11250/2490058

[10] R. Esposito, C. Anaç, M. A. N. Hendriks, and O. Çopuroğlu, 'Influence of the Alkali-Silica Reaction on the Mechanical Degradation of Concrete', *Journal of Materials in Civil Engineering*, vol. 28, no. 6, p. 04016007, Jan. 2016, doi: 10.1061/(ASCE)MT.1943-5533.0001486.

[11] V. Saouma and L. Perotti, 'Constitutive Model for Alkali-Aggregate Reactions', *ACI Mater J*, vol. 103, no. 3, May 2006.

[12] L. F. M. Sanchez, B. Fournier, M. Jolin, D. Mitchell, and J. Bastien, 'Overall assessment of Alkali-Aggregate Reaction (AAR) in concretes presenting different strengths and incorporating a wide range of reactive aggregate types and natures', *Cem Concr Res*, vol. 93, pp. 17–31, Mar. 2017, doi: 10.1016/J.CEMCONRES.2016.12.001.

[13] R. Esposito and M. A. N. Hendriks, 'Literature review of modelling approaches for ASR in concrete: a new perspective', *European Journal of Environmental and Civil Engineering*, vol. 23, no. 11, pp. 1311–1331, 2019, doi: 10.1080/19648189.2017.1347068.

[14] V. E. Saouma, *Numerical Modeling of AAR*. CRC Press, 2014. doi: 10.1201/B16353/NUMERICAL-MODELING-AAR-VICTOR-SAOUMA.

[15] V. E. Saouma and M. A. Hariri-Ardebili, *Aging, shaking, and cracking of infrastructures: From mechanics to concrete dams and nuclear structures*. Springer International Publishing, 2021. doi: 10.1007/978-3-030-57434-5/COVER.

[16] ISE, *Structural effects of alkali-silica reaction : technical guidance on the appraisal of existing structures*. SETO, 1992. Accessed: Oct. 17, 2024. [Online]. Available: https://www.istructe.org/resources/guidance/structural-effects-alkali-silica-reaction/

[17] ISE, *Structural effects of alkali-silica reaction : technical guidance on the appraisal of existing structures*. SETO, 1992. Accessed: Oct. 17, 2024. [Online]. Available: https://www.istructe.org/resources/guidance/structural-effects-alkali-silica-reaction/

[18] N. Smaoui, M. A. Bérubé, B. Fournier, and B. Bissonnette, 'Influence of specimen geometry, orientation of casting plane, and mode of concrete consolidation on expansion due to ASR', *Cement, Concrete and Aggregates*, vol. 26, no. 2, pp. 58–70, 2004, doi: 10.1520/CCA11927.

[19] F.-J. Ulm, O. Coussy, L. Kefei, and C. Larive, 'Thermo-Chemo-Mechanics of ASR Expansion in Concrete Structures', *J Eng Mech*, vol. 126, no. 3, pp. 233–242, Mar. 2000, doi: 10.1061/(ASCE)0733-9399(2000)126:3(233).

[20] D. M. Wald, M. T. Allford, O. Bayrak, and T. D. Hrynyk, 'Development and multiaxial distribution of expansions in reinforced concrete elements affected by alkali–silica reaction', *Structural Concrete*, vol. 18, no. 6, pp. 914–928, Dec. 2017, doi: 10.1002/SUCO.201600220.

[21] T. U. Mohammed, H. Hamada, and T. Yamaji, 'Alkali-silica reaction-induced strains over concrete surface and steel bars in concrete', *ACI Mater J*, 2003, Accessed: Oct. 17, 2024. [Online]. Available: https://www.academia.edu/download/34668292/Alkali-Silica_Reaction-Induced_Strains_over_Concrete.pdf

[22] S. Fan and J. M. Hanson, 'EFFECT OF ALKALI SILICA REACTION EXPANSION AND CRACKING ON STRUCTURAL BEHAVIOR OF REINFORCED CONCRETE BEAMS', *ACI Struct J*, vol. 95, no. 5, pp. 498–505, Sep. 1998.

[23] N. Smaoui, B. Bissonnette, M. A. Bérubé, and B. Fournier, 'Stresses induced by alkali-silica reactivity in prototypes of reinforced concrete columns incorporating various types of reactive aggregates', *Canadian Journal of Civil Engineering*, vol. 34, no. 12, pp. 1554–1566, Dec. 2007, doi: 10.1139/L07-063.

[24] P. Li, N. Tan, X. An, K. Maekawa, and Z. Jiang, 'Restraint effect of reinforcing bar on ASR expansion and deterioration characteristic of the bond behavior', *Journal of Advanced Concrete Technology*, vol. 18, no. 4, pp. 192–210, Apr. 2020, doi: 10.3151/JACT.18.192.

[25] O. Zhychkovska, 'Effect of alkali-silica reaction (ASR) on steel-concrete bond', University of Toronto, 2020. Accessed: Oct. 16, 2024. [Online]. Available: https://tspace.library.utoronto.ca/bitstream/1807/101053/3/Zhychkovska_Olesya_%20_202003_MAS_thesis.pdf

[26] P. Li, N. Tan, X. An, K. Maekawa, and M. Ren, 'Effect of multi-directional restraint induced by reinforced steel bars on ASR expansion and bond performance', *Journal of Advanced Concrete Technology*, vol. 20, no. 4, pp. 342–358, 2022, doi: 10.3151/jact.20.342.

[27] R. Esposito, C. Anaç, M. A. N. Hendriks, and O. Çopuroğlu, 'Influence of the Alkali-Silica Reaction on the Mechanical Degradation of Concrete', *Journal of Materials in Civil Engineering*, vol. 28, no. 6, p. 04016007, Jan. 2016, doi: 10.1061/(ASCE)MT.1943-5533.0001486.

[28] L. F. M. Sanchez, B. Fournier, M. Jolin, D. Mitchell, and J. Bastien, 'Overall assessment of Alkali-Aggregate Reaction (AAR) in concretes presenting different strengths and incorporating a wide range of reactive aggregate types and natures', *Cem Concr Res*, vol. 93, pp. 17–31, Mar. 2017, doi: 10.1016/J.CEMCONRES.2016.12.001.

[29] H. Kirchner, J. van Rooyen, P. F. van der Spuy, and G. P. A. G. van Zijl, 'Structural assessment of an ASR-affected reinforced concrete bridge', *Journal of the South African Institution of Civil Engineering*, vol. 65, no. 4, pp. 23–35, Dec. 2023, doi: 10.17159/2309-8775/2023/V65N4A3.

[30] J. A. Den Uijl, 'Structural consequences of ASR: An example on shear capacity', *Heron*, vol. 47, no. 2, pp. 125–139, 2002, Accessed: Oct. 16, 2024. [Online]. Available: https://heronjournal.nl/47-2/5.pdf

[31] H. Aryan and B. Gencturk, 'Influence of alkali-silica reaction on the shear capacity of reinforced concrete beams with minimum transverse reinforcement', *Eng Struct*, vol. 235, p. 112020, May 2021, doi: 10.1016/J.ENGSTRUCT.2021.112020.

[32] T. Ahmed, E. Burley, and S. Rigden, 'THE STATIC AND FATIGUE STRENGTH OF REINFORCED CONCRETE BEAMS AFFECTED BY ALKALI-SILICA REACTION', *ACI Mater J*, vol. 95, no. 4, Jul. 1998.

[33] C. Anca, F. Vecchio, and F. J. Vecchio, 'Behavior of alkali-silica reaction-affected reinforced concrete elements subjected to shear', *ACI Struct J*, vol. 114, no. 4, pp. 163–174, 2021, Accessed: Oct. 16, 2024. [Online]. Available: https://sites.utexas.edu/ferche/files/2023/09/Behavior-of-Alkali-Silica-Reaction-Affected-Reinforced_2021.pdf

[34] S. Fan and J. M. Hanson, 'EFFECT OF ALKALI SILICA REACTION EXPANSION AND CRACKING ON STRUCTURAL BEHAVIOR OF REINFORCED CONCRETE BEAMS', *ACI Struct J*, vol. 95, no. 5, pp. 498–505, Sep. 1998.

[35] J. Cao, N. Gowripalan, V. Sirivivatnanon, and J. Nairn, 'Investigation of ASR Effects on the Load-Carrying Capacity of Reinforced Concrete Elements by Ultra-Accelerated Laboratory Test', *Lecture Notes in Civil Engineering*, vol. 356 LNCE, pp. 43–52, 2022, doi: 10.1007/978-981-99-3330-3_7.

[36] M. Abe, S. Kikuta, Y. Masuda, and F. Tomozawa, 'EXPERIMENTAL STUDY ON MECHANICAL BEHAVIOR OF REINFORCED CONCRETE MEMBERS AFFECTED BY ALKALI-AGGREGATE REACTION', in *8th Internationl Conference on Alkali-Aggregate Reaction*, ICAAR, 1989, pp. 691–696. Accessed: Oct. 17, 2024. [Online]. Available: https://icaarconcrete.org/wp-content/uploads/2021/10/8ICAAR-AbeM-2.pdf

[37] S. Ohno, Y. Yoshioka, Y. Shmozakl, and T. Morikawa, 'THE MECHANICAL BEHAVIOUR OF BEAMS COATED AFTER ALKALI SILICA REACTION DAMAGE', in *8th Internationl Conference on Alkali-Aggregate Reaction*, 1989, pp. 697–702.

[38] S. Inoue, M. Fujii, K. Kobayashi, and K.-I. Nakano, 'STRUCTURAL BEHAVIORS OF REINFORCED CONCRETE BEAMS AFFECTED BY ALKALI-SILICA REACTION', in *8th Internationl Conference on Alkali-Aggregate Reaction*, ICAAR, 1989. Accessed: Oct. 16, 2024. [Online]. Available: https://icaarconcrete.org/wp-content/uploads/2021/10/8ICAAR-InoueS-1.pdf

[39] Y. Murazumi, N. Matsumoto, K. Takiguchi, and Y. Watanabe, 'Study on the influence of alkali-silica reaction on structural behavior of reinforced concrete members', 2005, Accessed: Oct. 16, 2024. [Online]. Available: https://repository.lib.ncsu.edu/bitstream/handle/1840.20/31626/H03_2.pdf?sequence=1

[40] T. Ahmed, E. Burley, and S. Rigden, 'THE STATIC AND FATIGUE STRENGTH OF REINFORCED CONCRETE BEAMS AFFECTED BY ALKALI-SILICA REACTION', *ACI Mater J*, vol. 95, no. 4, Jul. 1998.

[41] K. Kobayashi, T. Fukushima, and K. Rokugo, 'SHEAR STRENGTH OF ASR-DETERIORATED RC MEMBERS AND SHEAR REINFORCING EFFECT OF REPAIR BY ADDING REBAR', in *VIII International Conference on Fracture Mechanics of Concrete and Concrete Structures*, 2013.

[42] M. C. R. Farage, J. L. D. Alves, and E. M. R. Fairbairn, 'Macroscopic model of concrete subjected to alkali–aggregate reaction', *Cem Concr Res*, vol. 34, no. 3, pp. 495–505, Mar. 2004, doi: 10.1016/J.CEMCONRES.2003.09.001.

[43] M. Juliani, L. Juliani, T. Juliani, D. David, and L. Becocci, 'MODELLING OF ALKALI-AGGREGATE REACTION IN CONCRETE PILE CAPS STRUCTURES', *ICAAR*, 2008, Accessed: Oct. 16, 2024. [Online]. Available: https://icaarconcrete.org/wp-content/uploads/2020/11/15ICAAR-JulianiM-2.pdf

[44] A. C. Ferche, D. K. Panesar, S. A. Sheikh, and F. J. Vecchio, 'Toward Macro-Modeling of Alkali-Silica Reaction-Affected Structures', *Structural Journal*, vol. 114, no. 5, pp. 1121–1129, Sep. 2017, doi: 10.14359/51700778.

[45] X. Chen, 'Finite Element Modelling of ASR Affected Reinforced Concrete Beams Based on Realistic Pre-damage', 2018. Accessed: Oct. 16, 2024. [Online]. Available: https://resolver.tudelft.nl/uuid:3bf440ca-8644-47a6-8a0d-6af9927fa3dc

[46] R. V. Gorga, L. F. M. Sanchez, and B. Martín-Pérez, 'FE approach to perform the condition assessment of a concrete overpass damaged by ASR after 50 years in service', *Eng Struct*, vol. 177, pp. 133–146, Dec. 2018, doi: 10.1016/J.ENGSTRUCT.2018.09.043.

[47] D. Vo *et al.*, 'Evaluation of structures affected by Alkali-Silica reaction (ASR) using homogenized modelling of reinforced concrete', *Eng Struct*, vol. 246, p. 112845, Nov. 2021, doi: 10.1016/J.ENGSTRUCT.2021.112845.

[48] R. Z. Alrousan and B. R. Alnemrawi, 'The behavior of alkali-silica reaction-damaged full-scale concrete bridge deck slabs reinforced with CFRP bars', *Results in Engineering*, vol. 16, p. 100651, Dec. 2022, doi: 10.1016/J.RINENG.2022.100651.

[49] S. S. Kongshaug, R. M. Larssen, M. A. N. Hendriks, T. Kanstad, and G. Markeset, 'Load effects in reinforced concrete beam bridges affected by alkali–silica reaction—Constitutive modelling including expansion, cracking, creep and crushing', *Eng Struct*, vol. 245, p. 112945, Oct. 2021, doi: 10.1016/J.ENGSTRUCT.2021.112945.

[50] S. S. Kongshaug, M. A. N. Hendriks, T. Kanstad, and G. Markeset, 'Toward identifying the ASR-induced stresses from displacement measurements and crack observations—Demonstration on a beam bridge in Norway', *Eng Struct*, vol. 263, p. 114337, Jul. 2022, doi: 10.1016/J.ENGSTRUCT.2022.114337.

[51] S. Multon and F. Toutlemonde, 'Effect of applied stresses on alkali–silica reaction-induced expansions', *Cem Concr Res*, vol. 36, no. 5, pp. 912–920, May 2006, doi: 10.1016/J.CEMCONRES.2005.11.012.

[52] S. Poyet *et al.*, 'Influence of Water on Alkali-Silica Reaction: Experimental Study and Numerical Simulations', *Journal of Materials in Civil Engineering*, vol. 18, no. 4, 2006, doi: 10.1061/(ASCE)0899-1561(2006)18:4(588)ï.

[53] V. E. Saouma, R. A. Martin, M. A. Hariri-Ardebili, and T. Katayama, 'A mathematical model for the kinetics of the alkali-silica chemical reaction', *Cem Concr Res*, vol. 68, pp. 184–195, 2015, doi: 10.1016/j.cemconres.2014.10.021.

[54] C. Comi, B. Kirchmayr, and R. Pignatelli, 'Two-phase damage modeling of concrete affected by alkali–silica reaction under variable temperature and humidity conditions', *Int J Solids Struct*, vol. 49, no. 23–24, pp. 3367–3380, Nov. 2012, doi: 10.1016/J.IJSOLSTR.2012.07.015.

[55] C. Larive, 'Apports combinés de l'expérimentation et de la modélisation à la compréhension de l'alcali-réaction et de ses effets mécaniques', Jun. 1997, Accessed: Aug. 29, 2024. [Online]. Available: https://pastel.hal.science/tel-00520676

[56] F.-J. Ulm, O. Coussy, L. Kefei, and C. Larive, 'Thermo-Chemo-Mechanics of ASR Expansion in Concrete Structures', *J Eng Mech*, vol. 126, no. 3, pp. 233–242, Mar. 2000, doi: 10.1061/(ASCE)0733-9399(2000)126:3(233).

[57] T. Prinčič, P. Štukovnik, S. Pejovnik, G. De Schutter, and V. Bokan Bosiljkov, 'Observations on dedolomitization of carbonate concrete aggregates, implications for ACR and expansion', *Cem Concr Res*, vol. 54, pp. 151–160, Dec. 2013, doi: 10.1016/J.CEMCONRES.2013.09.005.

[58] M. Rashidi, J. Y. Kim, L. J. Jacobs, and K. E. Kurtis, 'Insights into alkali-silica reaction damage in mortar through acoustic nonlinearity', *AIP Conf Proc*, vol. 1706, no. 1, p. 60009, Feb. 2016, doi: 10.1063/1.4940515/586096.

[59] L. F. M. Sanchez, T. Drimalas, B. Fournier, D. Mitchell, and J. Bastien, 'Comprehensive damage assessment in concrete affected by different internal swelling reaction (ISR) mechanisms', *Cem Concr Res*, vol. 107, pp. 284–303, May 2018, doi: 10.1016/J.CEMCONRES.2018.02.017.

[60] L. F. M. Sanchez, B. Fournier, M. Jolin, and J. Duchesne, 'Reliable quantification of AAR damage through assessment of the Damage Rating Index (DRI)', *Cem Concr Res*, vol. 67, pp. 74–92, Jan. 2015, doi: 10.1016/J.CEMCONRES.2014.08.002.

[61] T. N. Nguyen, L. F. M. Sanchez, J. Li, B. Fournier, and V. Sirivivatnanon, 'Correlating alkali-silica reaction (ASR) induced expansion from short-term laboratory testings to long-term field performance: A semi-empirical model', *Cem Concr Compos*, vol. 134, p. 104817, Nov. 2022, doi: 10.1016/J.CEMCONCOMP.2022.104817.

[62] J. Lindgård *et al.*, 'Alkali–silica reaction (ASR)—performance testing: Influence of specimen pre-treatment, exposure conditions and prism size on alkali leaching and prism expansion', *Cem Concr Res*, vol. 53, pp. 68–90, Nov. 2013, doi: 10.1016/J.CEMCONRES.2013.05.017.

[63] B. Capra and J. P. Bournazel, 'Modeling of Induced Mechanical Effects of Alkali-Aggregate Reactions', *Cem Concr Res*, vol. 28, no. 2, pp. 251–260, Feb. 1998, doi: 10.1016/S0008-8846(97)00261-5.

[64] M. T. De Grazia, N. Goshayeshi, R. Gorga, L. F. M. Sanchez, A. C. Santos, and D. J. Souza, 'Comprehensive semi-empirical approach to describe alkali aggregate reaction (AAR) induced expansion in the laboratory', *Journal of Building Engineering*, vol. 40, p. 102298, Aug. 2021, doi: 10.1016/J.JOBE.2021.102298.

[65] R. Esposito, C. Anaç, M. A. N. Hendriks, and O. Çopuroğlu, 'Influence of the Alkali-Silica Reaction on the Mechanical Degradation of Concrete', *Journal of Materials in Civil Engineering*, vol. 28, no. 6, p. 04016007, Jan. 2016, doi: 10.1061/(ASCE)MT.1943-5533.0001486.

[66] J. N. Reddy, 'A dual mesh finite domain method for the numerical solution of differential equations', *International Journal for Computational Methods in Engineering Science and Mechanics*, vol. 20, no. 3, pp. 212–228, May 2019, doi: 10.1080/15502287.2019.1610987.

[67] H. Huang, N. Ma, H. Murakawa, and Z. Feng, 'A dual-mesh method for efficient thermal stress analysis of large-scale welded structures', *International Journal of Advanced Manufacturing Technology*, vol. 103, no. 1–4, pp. 769–780, Jul. 2019, doi: 10.1007/S00170-019-03606-4/METRICS.

[68] J. N. Reddy and P. Nampally, 'A dual mesh finite domain method for the analysis of functionally graded beams', *Compos Struct*, vol. 251, p. 112648, Nov. 2020, doi: 10.1016/J.COMPSTRUCT.2020.112648.

[69] J. N. Reddy, P. Nampally, and A. R. Srinivasa, 'Nonlinear analysis of functionally graded beams using the dual mesh finite domain method and the finite element method', *Int J Non Linear Mech*, vol. 127, p. 103575, Dec. 2020, doi: 10.1016/J.IJNONLINMEC.2020.103575.

[70] S. Farooq, G. Aoki, T. Miura, Y. Kawabata, and H. Nakamura, 'Anisotropic expansion behavior and crack orientation of reinforced concrete due to the alkali–silica reaction', *Cem Concr Compos*, vol. 151, p. 105568, Aug. 2024, doi: 10.1016/J.CEMCONCOMP.2024.105568.

[71] F. J. Vecchio and W. Shim, 'Experimental and Analytical Reexamination of Classic Concrete Beam Tests', *Journal of Structural Engineering*, vol. 130, no. 3, pp. 460–469, Mar. 2004, doi: 10.1061/(ASCE)0733-9445(2004)130:3(460).

[72] K. R. Kordina, G. Mancini, K. Schäfer, A. Schieβl, and K. Zilch, *Model Code 2010 - First complete draft, Volume 1*. in fib Bulletins. fib. The International Federation for Structural Concrete, 2010. doi: 10.35789/FIB.BULL.0055.

[73] 'DIANA User's Manuals', 2023, *DIANA FEA BV*. Accessed: Oct. 17, 2024. [Online]. Available: https://manuals.dianafea.com/d107/en/index-en.html

[74] M. Hendriks, 'Nonlinear FEA guideline for modelling of concrete infrastructure objects', 2020, *Rijkswaterstaat Centre for Infrastructure*. doi: 10.1201/b16645-109.

[75] B. Belletti, C. Damoni, and M. A. N. Hendriks, 'Validating the Guidelines for Nonlinear Finite Element Analysis of Concrete Structures - Part: Reinforced Beams', 2017, *Rijkswaterstaat Technisch Document, Utrecht*. doi: 10.1080/19648189.2011.9714859.

[76] V. Saouma and L. Perotti, 'Constitutive Model for Alkali-Aggregate Reactions', *ACI Mater J*, vol. 103, no. 3, May 2006.

[77] B. Capra and J. P. Bournazel, 'Modeling of Induced Mechanical Effects of Alkali-Aggregate Reactions', *Cem Concr Res*, vol. 28, no. 2, pp. 251–260, Feb. 1998, doi: 10.1016/S0008-8846(97)00261-5.

[78] C. Comi, B. Kirchmayr, and R. Pignatelli, 'Two-phase damage modeling of concrete affected by alkali–silica reaction under variable temperature and humidity conditions', *Int J Solids Struct*, vol. 49, no. 23–24, pp. 3367–3380, Nov. 2012, doi: 10.1016/J.IJSOLSTR.2012.07.015.

[79] M. T. De Grazia, N. Goshayeshi, R. Gorga, L. F. M. Sanchez, A. C. Santos, and D. J. Souza, 'Comprehensive semi-empirical approach to describe alkali aggregate reaction (AAR) induced expansion in the laboratory', *Journal of Building Engineering*, vol. 40, p. 102298, Aug. 2021, doi: 10.1016/J.JOBE.2021.102298.

[80] R. Esposito, C. Anaç, M. A. N. Hendriks, and O. Çopuroğlu, 'Influence of the Alkali-Silica Reaction on the Mechanical Degradation of Concrete', *Journal of Materials in Civil Engineering*, vol. 28, no. 6, p. 04016007, Jan. 2016, doi: 10.1061/(ASCE)MT.1943-5533.0001486.

[81] 'Internal source', 2024.

[82] A. Zahedi, C. Trottier, L. F. Leandro, and M. Noël, 'Condition assessment of alkali-silica reaction affected concrete under various confinement conditions incorporating fine and coarse reactive aggregates', *Cem Concr Res*, vol. 153, p. 106694, Mar. 2022, doi: 10.1016/J.CEMCONRES.2021.106694.

[83] R. A. Barbosa, S. G. Hansen, K. K. Hansen, L. C. Hoang, and B. Grelk, 'Influence of alkali-silica reaction and crack orientation on the uniaxial compressive strength of concrete cores from slab bridges', *Constr Build Mater*, vol. 176, pp. 440–451, Jul. 2018, doi: 10.1016/J.CONBUILDMAT.2018.03.096.

Appendix A: Software Selection Justification

In conducting finite element analysis (FEA) for this thesis, selecting the appropriate software was crucial to ensure accurate results and an efficient workflow. Several FEA software packages were evaluated, including DIANA FEA, ABAQUS, and ANSYS. The following table provides a comparative analysis of these options, justifying the selection of DIANA FEA for this research.

Table A.1: Comparative Analysis of FEA Software Options

Criteria	DIANA FEA	ABAQUS	ANSYS
User Interface	- Intuitive and user-friendly interface - Simplifies model setup and analysis execution	- Complex interface with a steep learning curve - Requires significant time to master	- Complex interface with a steep learning curve - Interface may be less intuitive for beginners
Material Models Availability	- Extensive library of pre-defined material models - Easy selection and assignment within the interface	- Requires manual definition of many material properties - Less intuitive material assignment	- Requires manual input for many material models - Material assignment can be complex
Specialization	- Tailored for structural, geotechnical, and civil engineering applications - Specialized features align with thesis requirements	- General-purpose FEA software - May lack specialized tools specific to civil engineering	- General-purpose FEA software - Specialized modules may require additional licensing
Nonlinear Analysis Capabilities	- Advanced nonlinear analysis features - Efficient handling of material and geometric nonlinearities	- Robust nonlinear analysis but setup can be complex - May require advanced knowledge	- Strong nonlinear capabilities but complex to configure - Advanced features may increase complexity
Learning Curve	- Shorter learning curve due to user-friendly design - Ideal for projects with time constraints	- Longer learning curve - Significant time investment needed to become proficient	- Longer learning curve - Mastery requires extensive training
Error Handling and Troubleshooting	- Reduced risk of input errors - Helpful error messages guide troubleshooting	- Higher risk of errors due to complex input requirements - Errors can be difficult to diagnose	- Complex error messages - Troubleshooting can be time-consuming
Documentation and Support	- Limited online resources due to being relatively newer - Official documentation is comprehensive but fewer third-party tutorials available	- Extensive documentation with abundant online tutorials - Large user community for support	- Extensive documentation - Numerous online resources and forums - Strong user community support
Licensing and Accessibility	- Academic licensing available - More accessible for	- Higher licensing costs - May be less accessible for individual students	- Higher licensing costs - Academic licenses may be limited

	students and educational institutions		
Computational Efficiency	- **Optimized for standard hardware setups** - Efficient performance without the need for high-end computational resources	- May require **more powerful hardware** for optimal performance - Longer computation times	- May require **significant computational resources** - Performance can be hardware-dependent
Compatibility and Integration	- Supports various data formats - **Easy integration** with other engineering tools and software	- Good compatibility but may require **additional configuration**	- Good compatibility - Integration may require **additional plugins or modules**
Previous Use in Similar Studies	- **Recognized** in civil engineering research - Used in specialized studies, though fewer in number due to its newer presence	- **Widely used** in engineering studies - Frequently cited in academic research	- **Popular in industry and academia** - Extensively used and cited in engineering research
Customization and Flexibility	- Allows for **some customization** - User-defined functions can be implemented if needed	- Highly customizable but **requires advanced knowledge** - Customization increases complexity	- Highly flexible with **extensive customization options** - May overwhelm users who require standard analyses
Cost-Benefit for Thesis Scope	- **Cost-effective** for the scope of the thesis - Provides all necessary features without unnecessary complexity	- **Higher cost** may not be justified for thesis scope - Extra features may remain unused	- **Higher cost** with features beyond thesis requirements - May not provide proportional benefits for the cost

Appendix B: Analytical Solution of the Dual Mesh Method (Review)

This appendix provides a brief review of Chen's work [45] on the dual mesh concept through an analytical solution. For a more detailed explanation and comprehensive analysis, please refer to Chen's original publication [45].

1D Linear Analysis of Dual Mesh Method

Chen [45] introduced a 1D analytical demonstration, to simplify the concept and gain a clearer understanding of the interaction between the two meshes in the Dual Mesh Method (DMM) concept. In this model, the structural mesh and the shadow mesh are assigned stiffness values, denoted as K_{st} and K_{sh}, respectively. The process begins with both meshes in their original, unloaded positions. When an initial strain is applied to the shadow mesh, it induces an initial displacement Δ_0. This displacement does not immediately generate stress but disrupts deformation compatibility, as only the shadow mesh is strained initially. This incompatibility leads to further deformation until both meshes reach equilibrium, sharing the same displacement due to their shared nodes.

The equilibrium and compatibility conditions are mathematically expressed as follows:

$$K_{st}\Delta_{st} = K_{sh}\Delta_{sh} \tag{14}$$

$$K_{st}\Delta_{st} = K_{sh}\Delta_{sh} \tag{15}$$

Solving these equations provides the final displacement:

$$\Delta_{st} = \frac{K_{sh}}{K_{sh} + K_{st}}\Delta_0 \tag{16}$$

The final displacement is determined by the relative magnitudes of K_{st} and K_{sh}. An increase in K_{sh} causes the final displacement to approach the initial displacement Δ_0, while a decrease in K_{sh} causes the final displacement to approach zero.

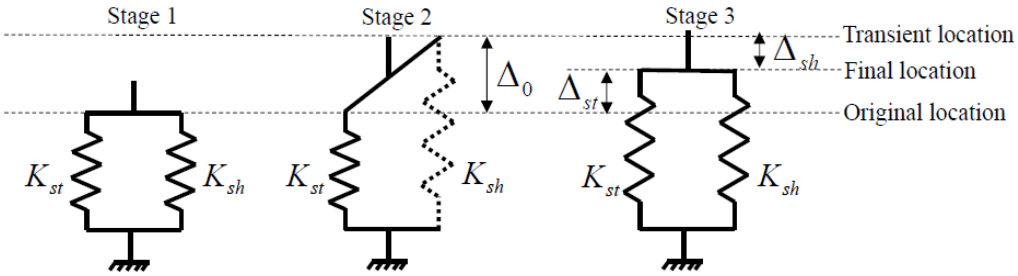

Figure 89 The interaction between structural mesh and shadow mesh in 1D model [45]

2D Linear Analysis of Dual Mesh Method

In the 2D element demonstration, the analysis incorporates the effects of the Poisson ratio, which result in iterative deformations between the x and y directions. When an initial strain is applied in one direction, it induces deformation in the perpendicular direction due to the Poisson effect. The procedure involves iteratively adjusting these deformations until equilibrium is achieved in both directions, ensuring that the model accurately reflects the interaction between the two axes.

Reinforcement

When reinforcement in concrete is considered, the presence of steel increases the stiffness in the direction of the reinforcement. This modified stiffness is expressed as:

$$E_{st,x} = V_s E_s + (1 - V_s) E_c \quad (17)$$

$$E_{st,y} = E_c \quad (18)$$

where V_s and V_c are the volume fractions of steel and concrete, respectively. This relationship indicates that a 1% increase in the reinforcement ratio results in a 5% increase in stiffness [45].

Appendix C: Detailed FEM Description of the 2D Cube Model

General Description

- **Software:** Diana FEA software.
- **Type of Model:** 2D finite element model using plane stress elements for concrete and embedded truss elements for reinforcements.
- **Analysis:** Static nonlinear analysis.

Geometry

Table 18 the cross-section properties of each finite element

		type	Shape	Dimensions	Thickness
All Analysis	Concrete sheet	Polygon sheet	Rectangular	100x100 mm	100 mm
	Shadow mesh sheet	Polygon sheet	Rectangular	100x100 mm	100 mm
	Steel rebar	Line	Line	100 mm	ϕ10 mm

Material Properties

Table 19 Material properties of concrete, Shadow mesh, and the steel rebar

Material	Parameter	Input
Concrete	Young's modulus (E_c)	33950 MPa
	Poisson's ratio (v)	0
	Compressive strength (f_{cm})	45 MPa
	Tensile strength (f_{tm})	4.11 MPa
Shadow mesh	Young's modulus (E_{DM})	2% E_C MPa
	Poisson's ratio (v)	0
Steel rebar	Young's modulus (E)	200000 MPa
	Yielding strength (f_{ym})	450 MPa
	Ultimate strength (f_{um})	540 MPa
	Ultimate strain (ε_{su})	0.05

Material Models

Table 20 constitutive models

	Specifications	Input data
Concrete	Class	Concrete and masonry
	Material Model	Total strain-based crack model
	Crack Bandwidth	10 mm
	Crack Orientation	Rotating
	Tensile curve	Linear
	Crack bandwidth specification	Rots
	Poisson’s ratio reduction	No reduction
	Compressive Behaviour	Elastic

Shadow Mesh	Class	Composites and rubber
	Material Model	Linear elastic isotropic
Reinforcement	Class	Steel
	Material Model	Von Mises plasticity
	Hardening Hypothesis	Strain hardening
	Hardening Type	Isotropic hardening

Iteration Procedure

Table 21 the characteristics of the incremental-iterative solution method

Analysis No.	*Iterative Scheme*	*Convergence norm*	*simultaneously satisfy*	*Tolerance*	*No convergence*	*Step size*	*Max iteration*
All)	Full Newton-Raphson	Energy AND Out-of-balance force	Both	0.0001 (energy) 0.01 (Out-of-balance force)	Continue	Both 0.01(100)	300

Appendix E: Detailed FEM Description of the Beam

General Description

- **Software:** Diana FEA software.
- **Type of Model:** 2D finite element model using plane stress elements for concrete and embedded truss elements for reinforcements.
- **Symmetry:** Only half of the beam is modelled due to symmetry to reduce computational cost.
- **Analysis:** Static nonlinear analysis.

Geometry

Includes beam geometry with longitudinal (3x M10, 2x M25, and 2x M30 bars) and transverse reinforcements, loading plate, and support plates, in addition to Dual Mesh.

Table 22 the cross-section properties of each finite element

		type	Shape	Dimensions	Thickness
All Analysis	Beam sheet	Polygon sheet	Rectangular	552 mm x 3420 mm	152 mm
	Dual Mesh sheet	Polygon sheet	Rectangular	552 mm x 3420 mm	152 mm
	Support plate	Polygon sheet	Rectangular	35 mm x 150 mm	152 mm
	Load plate	Polygon sheet	Rectangular	35 mm x 150 mm	152 mm
	3x M10	Line	Line	-	300.862 mm^2[3]
	2x M25	Line	Line	-	1404.31 mm^2[4]
	2x M30	Line	Line	-	997.518 mm^2[5]
	2x D4	Line	Line	-	51.4 mm^2[6]

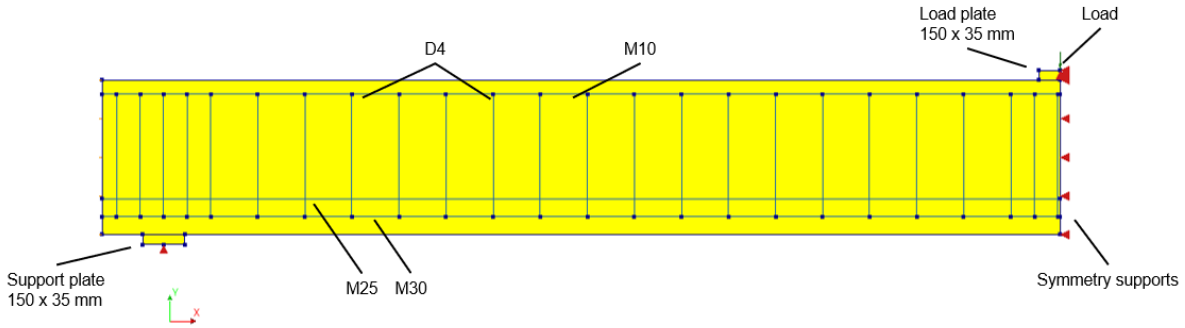

Figure 90 Model of the Toronto beam test VS-C3

[3] Equivalent Cross-Section for 3x ø11.3 mm
[4] Equivalent Cross-Section for 2x ø25.2 mm
[5] Equivalent Cross-Section for 2x ø29.9 mm
[6] Equivalent Cross-Section for 2x ø5.70 mm

Properties

Table 23 Properties for Beam Test VS-C3 (Vecchio and Shim 2004)

Material	Parameter	Input
Concrete	Young's modulus (E_c)	34300 MPa
	Poisson's ratio (v)	0.2
	Compressive strength (f_{cm})	43.5 MPa
	Tensile strength (f_{tm})	3.13 MPa
	Fracture energy in tension (G_f)	0.1439 N/mm
	Fracture energy in compression (G_c)	35.975 N/mm
	Mass density (ρ)	2.4E-9 T/mm^3
Dual Mesh (DM)	Young's modulus (E_{DM})	2% E_C MPa
	Poisson's ratio (v)	0
	Mass density (ρ)	0 T/mm^3

Table 24 Properties for Beam Test VS-C3 (Vecchio and Shim 2004)

Material	Parameter	Input
Reinforcement Steel M10	Young's modulus (E)	200000 MPa
	Yielding strength (f_{ym})	315 MPa
	Ultimate strength (f_{um})	460 MPa
	Ultimate strain (ε_{su})	0.025
Reinforcement Steel M25	Young's modulus (E)	200000 MPa
	Yielding strength (f_{ym})	445 MPa
	Ultimate strength (f_{um})	680 MPa
	Ultimate strain (ε_{su})	0.05
Reinforcement Steel M30	Young's modulus (E)	200000 MPa
	Yielding strength (f_{ym})	436 MPa
	Ultimate strength (f_{um})	700 MPa
	Ultimate strain (ε_{su})	0.05
Reinforcement Steel D4	Young's modulus (E)	200000 MPa
	Yielding strength (f_{ym})	600 MPa
	Ultimate strength (f_{um})	651 MPa
	Ultimate strain (ε_{su})	0.05
Steel for Plates	Young's modulus (E)	210000 MPa
	Poisson's ratio (v)	0.3

Material Models

	Specifications	Input data
Concrete	Class	Concrete and masonry
	Material Model	Total strain-based crack model
	Crack Bandwidth	37.5 mm
	Crack Orientation	Rotating
	Tensile curve	Linear, Exponential, Multi-linear[7]
	Crack bandwidth specification	Rots
	Poisson's ratio reduction	No reduction
	Compressive Behaviour	Parabolic
	Reduction model	Vecchio and Colline 1993
	Lower bound reduction curve	0.6
Dual Mesh	Class	Composites and rubber
	Material Model	Linear elastic isotropic
Reinforcement	Class	Steel
	Material Model	Von Mises plasticity
	Hardening Hypothesis	Strain hardening
	Hardening Type	Isotropic hardening
Support & load plates	Class	Steel
	Material Model	Linear elastic isotropic

Interfaces (sensitivity case):

- **Element Class:** Structural Interfaces used between steel plates and the concrete beam.
- **Integration Scheme:** Reduced Lobatto integration (3 integration points).
- **Thickness:** Equal to the beam's width (152 mm).
- **Properties Source:** Based on Belletti et al. (2017).

	Specifications	Input
Interface	Type	2D line interface
	Material Model	Nonlinear elasticity
	Normal Stiffness Modulus	Same as Young's modulus of concrete
	Shear Stiffness Modulus	Young's modulus of concrete / 10^8
	Normal and Shear Stiffness Reduction in Tension	
	Interface Opening for Reduction	0.001
	Reduction Factor	0

Boundary Conditions:

- **Supports:**
  - Fixed translation in Y direction at the midpoint of the support plate.
  - Symmetry condition restricts X-direction translation on the beam's edges.
  - Additional support at the load application point restricting translation in the Y direction.

Mesh Details:

- **Type:** Quadrilateral quadratic elements with an approximate size of 37.5 mm.

[7] Different tensile curves used, depending on the cases.

Loading conditions:

- **Deadweight**: Self-weight of concrete and steel elements is included
- **Design Load:** A point load applied at mid-span, assumed to be equal to 40% of the ultimate load capacity of the beam
- **ASR Load**: Prescribed strain applied to the shadow mesh to simulate ASR-induced expansion
- **Failure Load**: Prescribed deformation is increased incrementally until failure occurs to determine the ultimate load capacity

Table 25 the characteristics of the incremental-iterative solution method

Analysis No.	*Iterative Scheme*	*Convergence norm*	*simultaneously satisfy*	*Tolerance*	*No convergence*	*Step size*	*Max iteration*
(Design phase)	Full Newton-Raphson	Energy AND Out-of-balance force	Both	0.0001 (energy) 0.01 (Out-of-balance force)	Continue	Both 0.01(100)	300
(ASR phase)	Secant (Quasi-Newton)	Energy AND Out-of-balance force	Both	0.0001 (energy) 0.01 (Out-of-balance force)	Continue	Both 0.01(100)	300

Outputs Requested

- **Displacements**
- **Support reactions**
- **Crack strains**
- **Crack openings**
- **Total strains**
- **Cauchy stresses**